

The hydrological effects of explosive volcanic eruptions in the Asian monsoon region

A dissertation

Submitted in Partial Fulfilment of the Requirements
for the Degree of Doctor rerum naturalium (Dr. rer. nat.)
to the Department of Earth Sciences
of the Freie Universität Berlin

by

Zhihong Zhuo

Berlin, September 2019



Supervisor: Prof. Dr. Ulrich Cubasch
Freie Universität Berlin

Second examiner: Prof. Dr. Stephan Pfahl
Freie Universität Berlin

Date of the viva voce/defense: Nov. 27, 2019

Declaration

I hereby declare that except where specific reference is made to the work of others, the contents of this dissertation are original and have not been submitted in whole or in part for consideration for any other degree or qualification in this, or any other University. This dissertation is the result of my own work and includes nothing which is the outcome of work done in collaboration, except where specifically indicated in the text. This dissertation contains less than 50,000 words including appendices, bibliography, footnotes, tables and equations and has less than 50 figures.

Zhihong Zhuo
September 2019

Abstract

This thesis investigates the spatio-temporal characteristics and the mechanisms of explosive volcanic eruptions' hydrological effects in subregions of the Asian monsoon region (AMR). Based on two volcanic forcing indices, volcanic eruptions are classified according to their northern hemisphere volcanic aerosol injection (NHVAI). Comparisons on the hydrological effect of NHVAI in subregions of AMR are made between tree ring-based hydrological reconstruction data MADA, and the model data from CMIP5 and Last Millennium Ensemble project. MADA and the multi-model ensemble means agree on the drying effect of volcanic eruptions in the monsoon-dominated subregion, while discrepancies can be found in the westerlies-dominated subregion. A better agreement between proxy reconstruction and models is visible one year after the eruption rather than in the eruption year. Less proxy-model discrepancies are apparent in subregions with more available tree-ring chronologies. Results also indicate that the MMEM of CMIP5 is able to reproduce volcanic eruptions' hydrological effects in southern Asian monsoon region.

Based on the multi-model ensemble mean of CMIP5, the mechanism of the hydrological effects of NHVAI is investigated. The analyses focus on the drying effect in the relatively wettest area (RWA) and the wetting effect in the relatively driest area (RDA). The radiative effect of NHVAI causes a reduction of land-ocean thermal contrast. This changes the transport of water vapor and the formation of atmospheric clouds in the region. The regional temperature and precipitation responses result from the radiative effect of atmospheric clouds. The reduced land-ocean thermal contrast causes a weakened Asian summer monsoon circulation. The transport of water vapor from the ocean to the land is reduced. This results in the drying effect in the RWA due to the reduced formation of atmospheric clouds and precipitation. On the other hand, more water vapor is transported to the RDA due to the change of atmospheric circulation. The vertical motion is also enhanced. This increases the formation of atmospheric clouds and precipitation, and results in the wetting effect in the RDA. Another volcanic classification with only southern hemisphere volcanic aerosol injection (SHVAI) is constructed in order to study the climate effect of SHVAI. Results show inversed climate responses to SHVAI compared to NHVAI. Especially in the RWA, the results suggest significant drying effect after NHVAI, but slight wetting effect after SHVAI.

In order to investigate the climate effects of volcanic eruptions at different latitudes, volcanic forcing generated from the Easy Volcanic Aerosol (EVA) is implemented into the full-coupled land-ocean general circulation model MPI-ESM-LR. The aim is to simulate a Pinatubo-like eruption at 30°N (NH), equator (EQ) and 30°S (SH). The results confirm the opposite effects on monsoon precipitation after the NH and SH volcanic eruptions. Especially in India, one finds warming and drying effects after the NH eruption, but cooling and wetting effects after the SH eruption. The climate responses to the EQ eruption are similar to that after the SH eruption.

A tendency towards an El Niño event is visible one to three years after the NH eruption. After the SH eruption, a tendency towards the negative phase of the ENSO can be found. One year after the EQ eruption, a tendency towards an El Niño event can be found. The ENSO moves to the negative phase three years after the EQ eruption.

In summary, the mechanism of the climate response in India can be described as follows: The radiative effect of stratospheric aerosol from the NH (SH) volcanic eruption causes decreased (increased) interhemispheric thermal contrast and land-ocean thermal contrast. It strengthens (weakens) the South Asian summer monsoon and forces a southward (northward) move of the Intertropical Convergence Zone (ITCZ). This decreases (increases) the water vapor transport from the ocean to the land, and leads to the depletion (formation) of atmospheric cloud and less (more) precipitation in India. The radiative effect of the atmospheric cloud and the physical feedback of the system result further in the warming (cooling) and drying (wetting) effects in India. Results in this study indicate an important role the dynamical response and the resultant change of atmospheric cloud plays on the regional climate responses to volcanic eruptions.

Zusammenfassung

Die vorliegende Arbeit beschäftigt sich mit den räumlich-zeitlichen Eigenschaften und den Mechanismen der hydrologischen Effekte explosiver Vulkanausbrüche in den Subregionen der asiatischen Monsunregion (Asian Monsoon Region, AMR). Basierend auf zwei vulkanischen Forcierungsindizes werden Vulkanausbrüche nach ihrer vulkanischen Aerosolinjektion der Nordhalbkugel (auf der nördlichen Hemisphäre) (NHVAI) klassifiziert. Vergleiche über die hydrologische Wirkung von NHVAI in den Teilregionen der AMR werden zwischen den baumringbasierten hydrologischen Rekonstruktionsdaten MADA und den Modelldaten aus dem CMIP5 und dem Last Millennium Ensemble Projekt durchgeführt. MADA und das Multi-Model-Ensemble stimmen über die trockene Wirkung von Vulkanausbrüchen in der vom Monsun dominierten Subregion überein, während Diskrepanzen in der vom Westen dominierten Subregion zu finden sind. Eine bessere Übereinstimmung zwischen Proxy-Rekonstruktion und Modellen ist ein Jahr nach dem Ausbruch und nicht im Jahr des Ausbruchs sichtbar. In den Subregionen mit mehr verfügbaren Baumring-Chronologien sind weniger Proxy-Modell-Diskrepanzen zu erkennen. Die Ergebnisse deuten auch darauf hin, dass das MEM von CMIP5 zuverlässig die hydrologischen Effekte von Vulkanausbrüchen in der südasiatischen Monsunregion reproduzieren kann.

Basierend auf dem Multi-Modell-Ensemble-Mittelwert von CMIP5 wurde der Mechanismus der hydrologischen Effekte von NHVAI untersucht. Die Analysen konzentrieren sich auf den Trocknungseffekt im relativ nassesten Bereich (relatively wettest area, RWA) und den Benetzungseffekt im relativ trockensten Bereich (relatively driest area, RDA). Die Strahlungswirkung von NHVAI führt zu einer Verringerung des thermischen Kontrasts zwischen Land und Meer. Dies verändert den Transport von Wasserdampf und die Bildung von Wolken in der Region. Die regionalen Temperatur- und Niederschlagsreaktionen resultieren aus der Strahlungswirkung von atmosphärischen Wolken. Der reduzierte Wärmekontrast zwischen Land und Meer führt zu einer geschwächten Zirkulation des asiatischen Sommermonsuns. Der Transport von Wasserdampf aus dem Meer an Land wird reduziert. Dies führt zu dem Trocknungseffekt im RWA durch die reduzierte Bildung von atmosphärischen Wolken und Niederschlägen. Andererseits wird durch die Änderung der atmosphärischen Zirkulation mehr Wasserdampf zum RDA transportiert. Die vertikale Bewegung wird eben-

falls verstärkt. Dies erhöht die Bildung von atmosphärischen Wolken und Niederschlägen und führt zu einem Benetzungseffekt in der RDA. Eine andere vulkanische Klassifikation mit der vulkanischen Aerosolinjektion der südlichen Hemisphäre (SHVAI) wird erstellt, um die Klimawirkung von SHVAI zu untersuchen. SHVAI-Ergebnisse zeigen im Vergleich zu NHVAI umgekehrte Klimareaktionen. Insbesondere bei RWA deuteten die Ergebnisse auf einen signifikanten Trocknungseffekt nach NHVAI hin, aber einen leichten Benetzungseffekt nach SHVAI.

Um die Klimaauswirkungen von Vulkanausbrüchen in verschiedenen Breitengraden zu untersuchen, wird der aus dem Easy Volcanic Aerosol (EVA) erzeugte Vulkansturm in das vollgekoppelte Land-Ozean-Gesamtzirkulationsmodell MPI-ESM-LR implementiert. Das Ziel ist es, einen Pinatubo ähnlichen Ausbruch bei 30° N (NH), Äquator (EQ) und 30° S (SH) zu simulieren. Die Ergebnisse bestätigen die gegenteiligen Auswirkungen auf den Monsun nach den NH- und SH-Vulkanausbrüchen. Vor allem in Indien findet man nach dem NH-Ausbruch einen wärmenden und trocknenden Effekt, aber nach dem SH-Ausbruch einen kühlenden und benetzenden Effekt. Die Klimareaktion auf den EQ-Ausbruch ist ähnlich wie nach dem SH-Ausbruch.

Ein bis drei Jahre nach dem NH-Ausbruch ist eine Tendenz zu einem El Niño-Ereignis erkennbar. Nach dem SH-Ausbruch ist eine Tendenz zur negativen Phase des ENSO zu erkennen. Ein Jahr nach dem EQ-Ausbruch ist eine Tendenz zu einem El Niño-Ereignis zu erkennen. Das ENSO geht drei Jahre nach dem EQ-Ausbruch in die negative Phase über.

Zusammenfassend lässt sich der Mechanismus der Klimareaktion in Indien wie folgt beschreiben: Die strahlende Wirkung von stratosphärischem Aerosol aus dem NH (SH)-Vulkanausbruch bewirkt eine Abnahme (Zunahme) des interhemisphärischen Wärmekontrasts und des Land-See-Thermokontrasts. Es stärkt (schwächt) den südasiatischen Sommermonsun und zwingt eine südliche (nördliche) Bewegung der intertropischen Konvergenzzone (Intertropical Convergence Zone, ITCZ). Dies verringert (erhöht) den Wasserdampftransport vom Ozean zum Festland und führt zur Abnahme (Bildung) der atmosphärischen Wolke und zu weniger (mehr) Niederschlag in Indien.

Die Strahlungswirkung der atmosphärischen Wolke und die physikalische Rückkopplung des Systems führen in Indien weiter zum Erwärmungs- (kühlungs-) und Trocknungs- (Benetzungs-) Effekt. Die Ergebnisse dieser Studie zeigen eine wichtige Rolle, die die dynamische Reaktion und die daraus resultierende Veränderung der atmosphärischen Wolke für die regionale Klimareaktion auf Vulkanausbrüchen spielt.

Table of contents

List of figures	xiii
List of tables	xvii
1 Introduction	1
1.1 Motivation	1
1.2 Hydrological conditions in the Asian monsoon region	3
1.3 Volcanic eruption and climate	5
1.3.1 Radiative effect of volcanic eruptions	5
1.3.2 Volcanic effects on precipitation	8
1.3.3 Asymmetric volcanic aerosol distribution and precipitation	9
1.3.4 Tropical and extratropical eruption and climate	9
1.4 Volcanic eruption and El Niño/Southern Oscillation	10
1.5 Objectives and outline	12
2 Data and Methods	13
2.1 Volcanic forcing data	13
2.2 Tree-ring based hydrological reconstruction data	15
2.3 Model data	16
2.3.1 PMIP3/CMIP5 “last millennium” experiment	16
2.3.2 Last Millennium Ensemble	17
2.4 Methods	18
2.4.1 Hydrological indices	18
2.4.2 Volcanic classifications	18
2.4.3 Superposed Epoch Analysis with Monte Carlo significance test	19
2.4.4 Correlation analysis	19
2.4.5 Monsoon and ENSO indices	21
2.5 Model simulation using EVA and MPI-ESM	21

2.5.1	Easy Volcanic Aerosol forcing generator	21
2.5.2	Max-Planck-Institute Earth System Model	22
2.5.3	Experiment setup	24
3	Comparison of proxy and model on volcanic aerosols' hydrological effects in Asian westerlies and monsoon-dominated subregions	27
3.1	Explosive volcanic classifications	27
3.2	Subregions of the Asian monsoon region	31
3.3	Temporal comparison between proxy and model on hydrological effects of volcanic eruptions	31
3.3.1	Temporal response in the Asian monsoon region	31
3.3.2	Temporal response in westerlies and monsoon-dominated subregions	35
3.4	Spatial comparison between proxy and model on hydrological effects of volcanic eruptions	36
3.5	Discussion on uncertainty source of proxy and model	45
4	The Mechanism of volcanic aerosol's hydrological effect in the Asian monsoon region	51
4.1	Volcanic classifications with different hemispheric aerosol loadings	51
4.2	Climate response to GNH and GSH classifications	52
4.3	Correlation analysis	57
4.4	Mechanism of the hydrological response in GNH classification	59
4.4.1	The role of atmospheric clouds and water vapor	59
4.4.2	Moisture change due to dynamical responses	60
4.4.3	Summary of the mechanism	63
4.5	Different climate response to asymmetric volcanic aerosol loadings	67
5	Simulation on climate effects of volcanic eruptions at different latitudes	69
5.1	Volcanic forcing from EVA	69
5.2	Climate response to volcanic eruptions at different latitudes	72
5.2.1	Global radiative effects	72
5.2.2	Climate effects in the Asian monsoon region	76
5.2.3	ENSO responses to volcanic eruptions at different latitudes	81
5.3	Mechanisms of climate responses to different latitudinal volcanic eruptions in India	83
5.3.1	The direct radiative effect and dynamical response	83
5.3.2	The role of atmospheric clouds and water vapor	86

5.3.3	Scheme of the response mechanism	94
6	Conclusions and outlook	99
6.1	Proxy-model comparisons	99
6.2	Mechanism of the hydrological effects	101
6.3	Climate effects of volcanic eruptions at different latitudes	102
6.4	Outlook	104
	References	107
	Appendix A List of abbreviations	119

List of figures

1.1	Hydrological distribution and climate systems in the Asian monsoon region	4
1.2	Schematic diagram of volcanic inputs to the atmosphere and their effects . . .	6
2.1	Schematic view of MPI-ESM-LR	23
2.2	Schematic view of the experiment setup	25
3.1	Volcanic years and northern hemisphere volcanic aerosol injection in the GNH and CNH classifications	29
3.2	The proxy reconstruction data MADA and the divided subregions	32
3.3	Temporal SEA results of MADA PDSI (blue lines), JJA mean CMIP5 PDSI (red lines) and CMIP5 SPI12 (pink lines) corresponding to GNH (a) and CNH (b) volcanic classifications in 1300-1850 CE in the Asian monsoon region	34
3.4	Temporal SEA results of modeled JJA mean PDSI corresponding to GNH volcanic classification in the Asian monsoon region. Analyses are performed on LME PDSI over the core period (1300-1849), and both LME PDSI and CMIP5 PDSI over the whole period (850-1849)	35
3.5	Temporal SEA results of MADA PDSI (blue lines), JJA mean CMIP5 PDSI (red lines) and CMIP5 SPI12 (pink lines) corresponding to GNH (solid lines) and CNH (dashed lines) volcanic classifications in 1300-1850 CE in Asian westerlies-dominated subregion (a) and monsoon-dominated subregion (b) .	37
3.6	Temporal SEA results of modeled JJA mean PDSI corresponding to GNH volcanic classification in Asian westerlies-dominated subregion (a) and monsoon-dominated subregion (b). Analyses are performed on LME PDSI over the core period (1300-1849), and both LME PDSI and CMIP5 PDSI over the whole period (850-1849)	38
3.7	Spatial response of MADA PDSI (a), JJA mean CMIP5 PDSI (b) and CMIP5 SPI12 (c) to GNH volcanic classification in 1300-1850 CE in the Asian monsoon region	41

3.8	Spatial response of MADA PDSI (a), JJA mean CMIP5 PDSI (b) and CMIP5 SPI12 (c) to CNH volcanic classification in 1300-1850 CE in the Asian monsoon region	43
3.9	Spatial response of modeled JJA mean PDSI to GNH classification in the Asian monsoon region. Analyses were performed on LME PDSI over the core period (1300-1849), and both LME PDSI and CMIP5 PDSI over the whole period (850-1849)	44
3.10	Temporal analysis results of MADA PDSI corresponding to different volcanic classifications	47
4.1	Volcanic years and hemispheric volcanic aerosol injection magnitudes in GNH (red lines and texts) and GSH (blue lines and texts) classifications. Model ensemble members used in this chapter are shown in the green box .	53
4.2	Temporal SEA results of summer JJA mean PDSI corresponding to GNH (yellow line) and GSH (green line) volcanic classifications in 1300-1850 CE in the Asian monsoon region	54
4.3	Temporal SEA results of summer JJA mean temperature ($^{\circ}\text{C}$) of land (a) and difference between land and ocean (b) in the Asian monsoon region.	56
4.4	Spatial distribution of the Palmer Drought Severity Index (PDSI, top) and the temperature (T , $^{\circ}\text{C}$, bottom) anomalies	57
4.5	Spatial distribution of top of the atmosphere outgoing shortwave radiation (TOA OSR, W/m^2) anomalies in clear sky	59
4.6	Spatial distribution of top of the atmosphere outgoing shortwave radiation (TOA OSR, W/m^2 , top) in full sky and cloud area fraction (C , $\%$, bottom) anomalies	61
4.7	Spatial distribution of evaporation (E , mm/day , top) and relative humidity (RH , $\%$, bottom) anomalies	62
4.8	Temporal SEA results of the East Asian summer monsoon index (EASMI, m/s , top) and South Asian summer monsoon index (SASMI, m/s , bottom) anomalies	64
4.9	Vertical integrated moisture flux (VIMF, $\text{kg}/\text{m}\cdot\text{s}$, vector) and its divergence (VIMFD, $10^{-5} \text{ kg}/\text{m}^2\cdot\text{s}$, shades) in five years before the eruption (a, REF) and the anomalies in the eruption year of the GNH (b) and GSH (c) classification	65
5.1	Global mean aerosol optical depth anomaly at 550 nm (top) and its zonal mean distributions for the NH (a), EQ (b) and SH (c) volcanic eruption cases (bottom) generated by Easy Volcanic Aerosol (EVA) forcing generator . . .	71

5.2	Global mean net solar radiation (W/m^2) anomaly at top of the atmosphere in clear sky (top) and its zonal mean distributions for the NH (a), EQ (b) and SH (c) volcanic eruption cases (bottom)	74
5.3	Global mean surface temperature ($^{\circ}\text{C}$) anomaly (top) and its zonal mean distributions for the NH (a), EQ (b) and SH (c) volcanic eruption cases (bottom)	75
5.4	JJA mean temperature ($^{\circ}\text{C}$, a) and precipitation (mm/day, b) anomaly over the land of the Asian monsoon region	78
5.5	Spatial distribution of JJA mean temperature ($^{\circ}\text{C}$) anomaly in 1992 in the Asian monsoon region for the NH (a), EQ (b) and SH (c) volcanic eruption cases	79
5.6	Spatial distribution of JJA mean precipitation (mm/day) anomaly in 1992 in the Asian monsoon region for the NH (a), EQ (b) and SH (c) volcanic eruption cases	80
5.7	Time series of Oceanic Niño Index ($^{\circ}\text{C}$) anomaly for the EQ (a), NH (b) and SH (c) volcanic eruption cases	82
5.8	Difference of JJA mean temperature ($^{\circ}\text{C}$) anomaly between northern and southern hemisphere (a) and ITCZ in 1992 (b) indicated by the JJA mean zonal mean precipitation (mm/day) anomaly between 20°N and 20°S	84
5.9	South Asian summer monsoon index (m/s) anomaly	85
5.10	JJA mean vertically integrated moisture flux (vector, $\text{kg}/\text{m}\cdot\text{s}$) and its divergence (shaded, $10^{-5} \text{ kg}/\text{m}^2\cdot\text{s}$) for the control runs without any volcanic eruption (a), and their anomalies after the NH (b), EQ (c) and SH (d) volcanic eruptions in 1992	87
5.11	Spatial distribution of JJA mean net surface solar radiation (W/m^2) anomaly in the clear sky after the NH (a), EQ (b) and SH (c) volcanic eruptions in 1992	89
5.12	Spatial distribution of JJA mean net surface solar radiation (W/m^2) anomaly in the full sky after the NH (a), EQ (b) and SH (c) volcanic eruptions in 1992	90
5.13	Spatial distribution of JJA mean total cloud cover (%) anomaly after the NH (a), EQ (b) and SH (c) volcanic eruptions in 1992	91
5.14	Spatial distribution of JJA mean vertical integrated water vapor (kg/m^2) anomaly after the NH (a), EQ (b) and SH (c) volcanic eruptions in 1992	92
5.15	Spatial distribution of JJA mean relative humidity (%) anomaly after the NH (a), EQ (b) and SH (c) volcanic eruptions in 1992	93
5.16	Schematic view of the mechanism chain on the climate response to volcanic eruptions at different latitudes	95

List of tables

2.1	PMIP3/CMIP5 Model ensembles used in the study	17
2.2	volcanic classifications, identified eruption years and stratospheric aerosol magnitudes	20
2.3	Summary of the simulations used for analysis.	25
3.1	The volcanic classifications tested on the proxy reconstruction data and the included event years	30
3.2	Percentage of grid cells that have same sign between MADA PDSI and CMIP5 PDSI/SPI12 in each subregion	39
4.1	Average Pearson cross correlation (r) values between precipitation (P), sea surface temperature (SST) and radiation, heat and moisture related variables of the Asian monsoon region. Numbers in italics are significant at the 95% confidence level. Numbers in bold are significant at the 99% confidence level.	58

Chapter 1

Introduction

1.1 Motivation

The uneven spatial distribution of precipitation and the resultant flood and drought extremes in the Asian monsoon region (AMR, 8.75°S–56.25°N, 61.25°E–143.75°E, Cook et al. (2010)) affect the lives of more than 60% of the global population. Asian summer monsoon precipitation was observed to be significantly decreased after volcanic eruptions in both observation and model simulations (Iles and Hegerl, 2014; Trenberth and Dai, 2007; Zambri and Robock, 2016). However, these studies were more about impact on the global scale; summer monsoon reduction was only briefly studied. For the eruptions in the period without observation, studies focusing on Asian summer monsoon with spatial analysis can be performed through model simulation, like Peng et al. (2010), Man et al. (2014) and Man and Zhou (2014). However, these studies were more about East Asian summer monsoon, and bias results, only based on the model simulation, might come from the performance of the employed single model. Only in recent decades, with the development of hydrological proxy reconstructions (Cook et al., 2010; Shen et al., 2007; Shi et al., 2017), spatio-temporal analysis with proxy reconstructions were performed in the Asian monsoon region (Anchukaitis et al., 2010; Gao and Gao, 2018; Shen et al., 2007; Zhuo et al., 2014). However, different results were reported, which were based on the different proxy reconstructions, especially on the spatial distribution of the hydrological effects after volcanic eruptions. This indicates the potential uncertainties, which the proxy reconstructions have. Among these proxy reconstructions, the Monsoon Asia Drought Atlas (MADA, Cook et al. (2010)) is widely used as a criterion to evaluate the model performance on the volcanic effects in the Asian monsoon region (Anchukaitis et al., 2010; Stevenson et al., 2017, 2016; Wegmann et al., 2014; Zhang et al., 2012). Nevertheless, results based on a single model simulation show large discrepancies, even inversed spatial patterns, to MADA in these studies. The proxy-model discrepancies can be caused by uncertainties

from both sides. The proxy data suffers from the incomplete temporal and spatial coverage of the tree-rings (Cook et al., 2010), or the limitation of the availability of the maximum latewood density chronology. The uncertainty of the model simulation can result from the problematic volcanic forcing reconstruction (Sigl et al., 2015; Stoffel et al., 2015), and the shortcomings in reproducing the dynamic responses in the atmosphere and the ocean (Ding et al., 2014).

Recent studies report that a multi-model ensemble (MME) approach leads to a better estimation of climate change as it averages out unrelated model errors (Flato et al., 2013) and El Niño-Southern Oscillation (ENSO) effects (Iles et al., 2013). It even enhances the climate prediction skill (Kadow et al., 2015), which is also significantly affected by volcanic aerosol (Timmreck et al., 2016). MME mean (MMEM) of the fifth phase of Coupled Model Intercomparison Project (CMIP5) shows large improvements in reflecting global temperature and precipitation variation (Flato et al., 2013; Knutti and Sedláček, 2012) as well as monsoon and precipitation variation in East Asia (Kusunoki and Arakawa, 2015; Song and Zhou, 2014). Using MME approach, the response of a reduced temperature and summer monsoon rainfall to volcanic eruptions are also clearly detected in historical simulations (Zambri and Robock, 2016), and even in the “last millennium (LM)” experiment of CMIP5 (Zambri et al., 2017). However, the climate effect of volcanic eruptions reported in Zambri et al. (2017) is more about the global scale. Studies aimed at the Asian monsoon region on a regional scale is important for a better water management and coping strategy after volcanic perturbation in the near future.

The mechanism of the hydrological response to volcanic eruptions were only roughly investigated (Man and Zhou, 2014; Man et al., 2012, 2014; Oman et al., 2006). Conclusions in these studies are based either on temporal analysis or on a global perspective, without consideration of the regional difference (Oman et al., 2006). Furthermore, most studies aimed at the East Asian summer monsoon region (Man and Zhou, 2014; Man et al., 2012, 2014), but did not consider the teleconnection between the South and East Asian summer monsoon (Preethi et al., 2016). Therefore, large uncertainties remain on the explaining of the mechanism of the hydrological response. Especially, no studies have considered the monsoon and westerlies-dominated subregions of the Asian monsoon region. There are only limited studies focusing on the hydrological effect of different hemispheric volcanic aerosol injection (VAI) in the Asian monsoon region (Liu et al., 2016; Zhuo et al., 2014). These studies all constructed the hemispheric volcanic classifications, based on the volcanic forcing reconstruction, which implicitly represented different magnitude of volcanic aerosols in different hemispheres. This therefore casts shadows on how accurate the conclusion is on

the hydrological effects of different hemispheric VAI, as well as the different effects from tropical and extratropical eruptions.

This study aims to comprehensively study the hydrological response to explosive volcanic eruptions in subregions of the Asian monsoon region. It investigates 1) the capability of CMIP5 MMEMs on reproducing the temporal variation and spatial distribution of the hydrological effect, which is based on proxy-model comparisons 2) the mechanisms of the spatio-temporal hydrological effects, which are based on CMIP5 MMEM, 3) the climate effects of different latitudinal volcanic eruptions and the related mechanisms, which are based on model simulation. The comparison between the hydrological proxy data and the model output contributes to evaluate their uncertainty and reliability. Additionally, previous studies mostly investigated the temporal response of the Asian monsoon to volcanic eruptions, and no attention was paid to the different dominated subregions, this study will fill in the gaps by discussing the spatial distribution of the hydrological effects in subregions of the Asian monsoon region. The present work extends the study on the spatio-temporal characteristics and mechanisms of the climate response to different hemispheric volcanic eruptions. Results in this study will contribute to a better understanding of the regional difference of volcanic eruptions' hydrological effects and the potential mechanism, and to provide a potential theoretical reference to augment drought and flood management strategies in different areas of Asia in the face of future explosive volcanic eruptions.

1.2 Hydrological conditions in the Asian monsoon region

The Asian monsoon region (AMR, 8.75°S–56.25°N, 61.25°E–143.75°E, Cook et al. (2010)) covers the most populated countries like China and India. Any perturbation to the climate, especially the hydrological condition in the summer, brings the greatest effect on the largest population all over the world. As part of the largest continental landmass on Earth, the AMR has more climatic types than any other continent. The northwest part of the region has a specific continental climate. In the southeast part, it involves the complex Asian monsoon system due to the contrast between the landmass and the Indian and Pacific Ocean. It is also largely affected by other factors like the Tibetan Plateau (TP) and Eurasian snow cover (Ha et al., 2012), and various large-scale climate phenomenon like the Intertropical Convergence Zone (ITCZ, Yancheva et al. (2007)) and ENSO (Ha et al., 2012). Thus, understanding the hydrological variation to any perturbation is both socioeconomically and biophysically important (Dando, 2005).

Figure 1.1 shows the dominant climate system and the climatological precipitation distribution in the boreal summer (June-July-August, JJA) in 1981-2010. The purple line in the

figure indicates the modern Asian summer monsoon limit, to the northwest are the westerlies dominated arid areas, to the southeast are the monsoon-dominated humid areas (Chen et al., 2008; Dando, 2005; Herzsuh, 2006). It includes two monsoon subsystems – the East Asian summer monsoon (EASM) and the South Asian summer monsoon (SASM), which are usually separated by 100°E longitude (Chiang et al., 2017; Herzsuh, 2006). The EASM has specific climate characteristics, which cannot be simply regarded as an eastward extension of the SASM. The SASM should be a tropical monsoon because the wind changes from the winter easterlies to summer westerlies. The EASM should be regarded as a sub-tropical monsoon while the low-level winds reverse from winter northerlies to summer southerlies (Ding and Chan, 2005; Wang and Lin, 2002), and is dominated by the western Pacific subtropical high (WPSH) (Loo et al., 2015; Zhou et al., 2009).

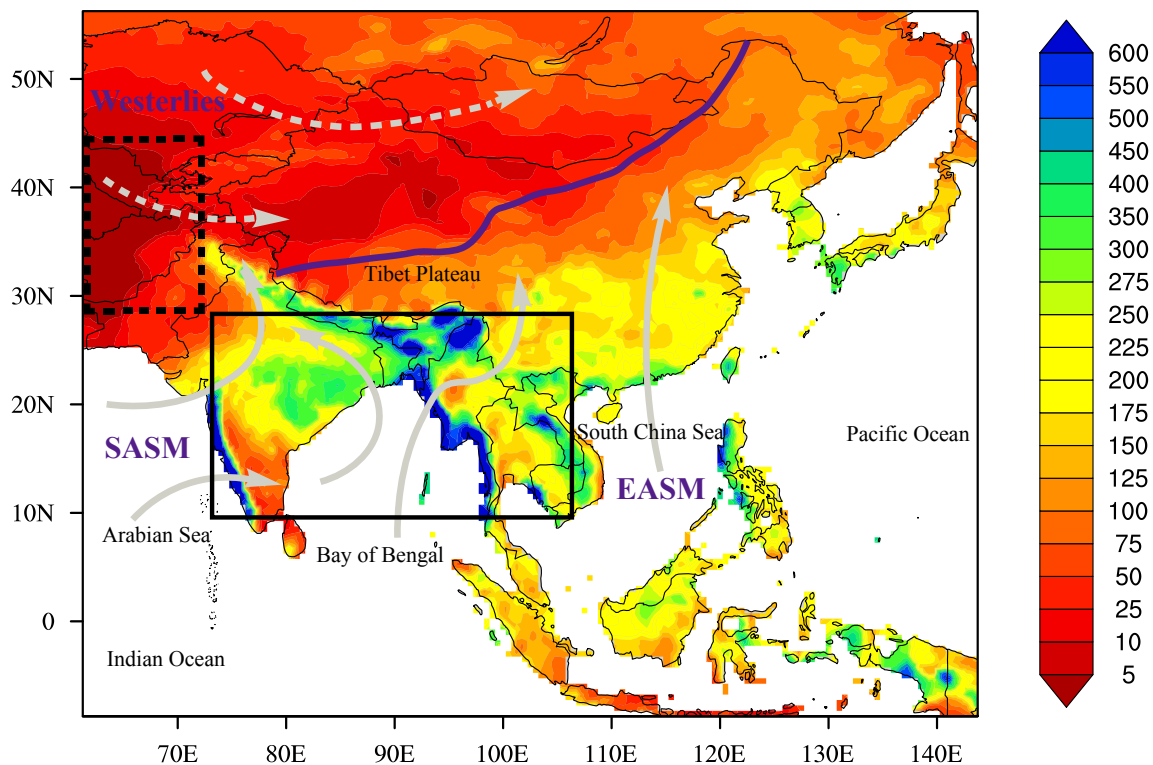


Fig. 1.1 Hydrological distribution and climate systems in the Asian monsoon region. The colors indicate the climatological June-July-August mean precipitation (mm/month) in 1981-2010, which are based on the monthly global land-surface precipitation of Global Precipitation Climatology Centre Full Data Reanalysis version 7. The solid and dashed black box indicates the relatively wettest area (RWA) and the relatively driest area (RDA), respectively.

From the precipitation distribution (figure 1.1), we can see an uneven precipitation distribution with a diminishing scale from southeast to northwest in the Asian monsoon

region. Comparing to the monsoon-dominated subregion, there are much less precipitation in the westerlies-dominated subregion. The southwestern part (areas enclosed by the black boundary; hereafter marked as the relatively driest area (RDA) in this study) tend to be the driest area. Here, because westerly wind brings limited moisture to this region, the transport of air mass from its adjacent areas may play a key role in controlling the moisture conditions. Intense heating due to the strong summer insolation on the Tibetan Plateau and adjacent Asian highlands causes a strong uplift motion in these areas. This strengthens the subsidence of dry air mass, which contributes to the intensification of the dry climate (Chen et al., 2008). In the monsoon-dominated subregion, the temporal and spatial distribution of summer precipitation is largely affected by the evolution of the South and East Asian summer monsoon (Wang et al., 2005). From the figure, one can see that areas affected by the South Asian summer monsoon have the largest precipitation, especially the area between the Tibet Plateau and the Bay of Bengal (as indicated by the black rectangle; hereafter marked as the relatively wettest area (RWA) in this study). The areas affected by the East Asian summer monsoon experience an uneven precipitation distribution with a diminishing scale from south to north (Wang et al., 2012), which often results in severe and persistent drought in north China while heavy precipitation and even floods in south China (Ding et al., 2009, 2008).

1.3 Volcanic eruption and climate

1.3.1 Radiative effect of volcanic eruptions

Franklin (1784) first reported that the extreme cold summer in 1783 in Europe might be due to the climate effect of the Laki eruption. The large eruption of Tambora in 1815 which caused an extreme cooling in the summer of 1816 as “the year without summer” (Wood, 2015). In the 20th century, the explosive eruption of El Chichón in April 1982, and the Mount Pinatubo in June 1991 drew the attention of scientists to comprehensively investigate the climatic effect of volcanic eruptions. Along with the development of technology, more accurate and comprehensive observations can be used to study the climate effects of volcanic eruptions. As the best recorded large event, the explosive eruption of Mount Pinatubo in 1991 was investigated by a large amount of studies. Analyses, which were based on both observation data (Robock, 2002; Robock and Mao, 1995) and model simulations (Hansen et al., 1992; Kirchner et al., 1999; Pitari and Mancini, 2002), indicate a significant summer temperature decrease of global mean and northern hemisphere (NH) bands after the 1991 Mount Pinatubo eruption.

Simulations on more volcanic events with different models suggested consistent cooling that can last up to 4 years after the eruptions (Robock and Y., 1994; Schneider et al., 2009). These studies revealed the radiative effect of the volcanic eruptions. As summarized by Robock (2000, 2015) (figure 1.2), volcanic eruption injects gases and ashes into the atmosphere, those injected into troposphere by small eruptions can last only one to three weeks, because they are quickly washed out by precipitation, thus bringing a limited climate effect. However, with an explosive volcanic eruption, large amount of gases injected into the stratosphere can last one to three years because of limited convection and associated turbulence in the stratosphere. These gases include a large amount of sulfur, which are converted into sulfate aerosols in the stratosphere. These aerosols reflect and scatter more incoming solar flux back into the space, thus leading to a net cooling effect in the surface. Meanwhile, these sulfate aerosols absorbed longwave radiation from the surface, bringing a net warming effect in the stratosphere.

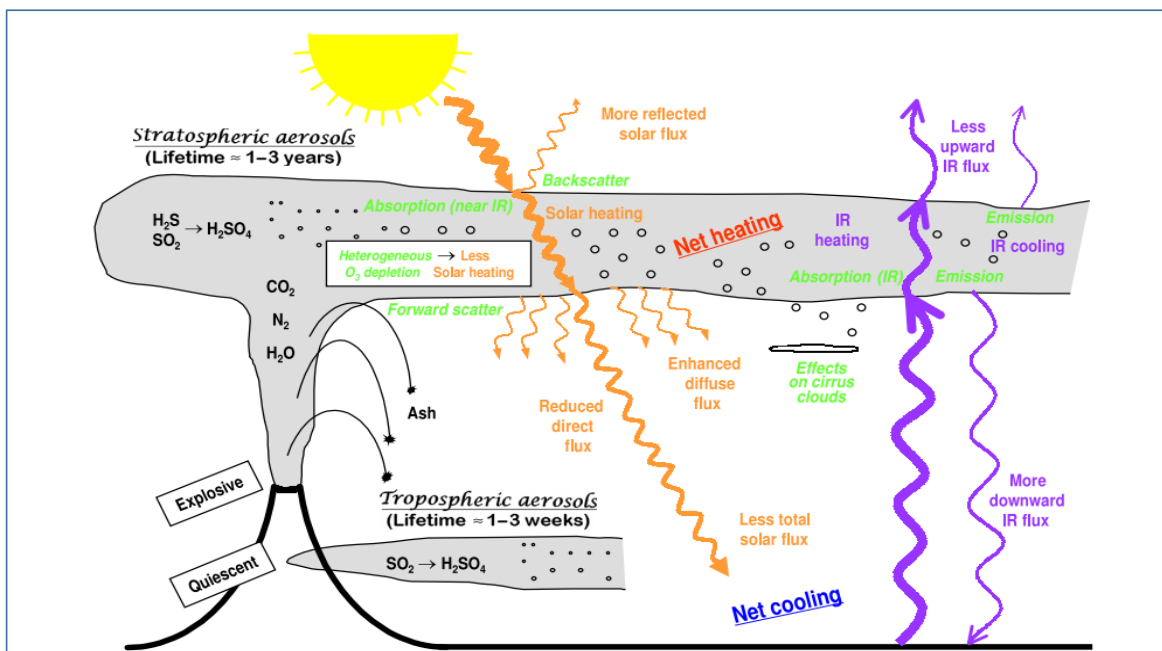


Fig. 1.2 Schematic diagram of volcanic inputs to the atmosphere and their effects, from Robock (2015)

Studies on volcanic eruptions in recent centuries indicated their significant surface cooling effects. These assessments helped to attribute the global warming in the past century to anthropogenic greenhouse gases, as the anthropogenic influences on climate must be evaluated against a background of continued natural forcing of the climate system (Robock, 2000). As an important nature forcing, we need to look into historical volcanic eruptions that trace further back in time to evaluate its variability and uncertainty. This is a big

challenge due to the short observational records on both the eruption history and the climate conditions. In this context, there are two ways to conduct researches, one depends on the proxy reconstructions, and the other one relies on model simulation. However, model simulation on paleoclimate depends on the proxy reconstruction of volcanic forcing.

Reconstructed volcanic forcing indices used in the model simulation are the fundamental basis for climate research. Pioneering indices of volcanism includes the Dust Veil Index by Lamb and Sawyer (1970) and the Volcanic Explosivity Index (VEI) by Newhall and Self (1982). A more thorough review of these and other volcanic indices can be found in Robock and Free (1995) and Robock (2000). Later, ice cores were found to be valuable to reconstruct the longer history of volcanism as a direct measure of volcanic sulfate that relates to the climate effect. In the past several decades, works on volcanic forcing reconstructions were developed from using single or a few ice cores (Ammann et al., 2007; Ammann and Naveau, 2003; Robock and Free, 1995) to combining multiple ice cores from both the Arctic and Antarctica (Crowley et al., 2008; Gao et al., 2008). Most recently updated volcanic forcing reconstructions have been published by Sigl et al. (2015) and Toohey and Sigl (2017). In these two reconstructions, ice cores and tree rings are combined. This contributes to a better dating of the volcanic events in the last millenniums and more precise estimation of volcanic aerosols (Sigl et al., 2015). From the reconstructions available, only Gao et al. (2008) and Crowley et al. (2008) volcanic forcing indices have been adopted by the third phase of paleoclimate model intercomparison project (PMIP3, Braconnot et al. (2012)). PMIP3 launched the “LM” experiment (Schmidt et al., 2011) as a contribution to the fifth phase of the climate model intercomparison project (CMIP5, Taylor et al. (2012)). These two indices have been widely used by the research community.

These reconstructions help to identify the year and aerosol magnitude of the historical eruptions in the past millennium. To reflect their climate impacts, climate records are needed. In the years without any continuous observational records, proxy reconstructions are widely used as an indicator of temperature and hydrological conditions. These are not only based on tree rings (Briffa et al., 2001; Cook et al., 2010; Schneider et al., 2015; Stoffel et al., 2015; Wilson et al., 2016), but also on multi-proxies including lake sediment, ice cores, historical records etc. (Mann et al., 1999; Steiger et al., 2018). Analysis of these proxy data also shows the cooling effect of volcanic eruptions in the past 600 years. (Briffa et al., 2001; Hegerl et al., 2003; Mann et al., 2012; Stoffel et al., 2015). With these volcanic forcing reconstructions used in climate models, researchers are also able to simulate the volcanic eruption and study their climate effects go back to recent millennium (Mann et al., 2012; Stoffel et al., 2015; Timmreck, 2012). Simulation with a fully coupled general circulation model (GCM) and a

simple energy-balance climate model (EBM) indicates that the cooling effect of explosive volcanic eruptions can reach up to 2°C (Mann et al., 2012).

1.3.2 Volcanic effects on precipitation

The radiative effect of volcanic eruptions further affects the hydrological process. Trenberth and Dai (2007) showed that the observed precipitation, runoff and the Palmer Drought Severity Index (PDSI) decreased significantly in 1992 after the Mount Pinatubo eruption. Both observation and model simulation indicates detectable reduction of global precipitation after volcanic eruptions (Gillett et al., 2004; Iles and Hegerl, 2014; Iles et al., 2013; Paik and Min, 2016; Robock and Y., 1994), which is mainly caused by the reduced vertical motion following the decrease of incoming shortwave radiation and the cooling effect after volcanic eruptions (Paik and Min, 2016). Precipitation was found to be decreased largely in tropical areas (Colose et al., 2016a; Iles and Hegerl, 2014). The reduction of tropical precipitation is mainly caused by the reduced evaporation due to the blockage of shortwave radiation after volcanic eruptions (Robock, 2015). The reduction of precipitation was found to be even notable in the summer monsoon regions (Colose et al., 2016b; Iles and Hegerl, 2014; Liu et al., 2016; Man et al., 2014; Oman et al., 2006; Schneider et al., 2009; Zambri and Robock, 2016). This is due to the inhomogeneous cooling between the land and sea, which results in a decreased land-sea thermal contrast and thus the weakening of the summer monsoon (Man and Zhou, 2014; Man et al., 2012, 2014; Oman et al., 2006; Robock, 2015).

The Asian monsoon region is one of the most affected areas. However, the temporal and spatial characteristics of the volcanic eruptions' hydrological effects and the related mechanisms have only briefly been investigated (Anchukaitis et al., 2010; Man and Zhou, 2014; Man et al., 2012, 2014; Zhuo et al., 2014). Most of them only focus on one part of the area (Gao and Gao, 2018; Man and Zhou, 2014; Man et al., 2012, 2014; Zhuo et al., 2014). These studies also show different spatial patterns of the hydrological effect based on different proxy reconstruction data and/or model data. Studies aiming at a better understanding the hydrological effect in subregions of the monsoon Asia need to be performed, especially, the westerlies and monsoon-dominated subsystems should be taken into consideration when performing the studies. The mechanism of the hydrological effect, especially in different subregions of the AMR is rarely investigated. The conclusion on the weakened summer monsoon due to the volcanic eruption was generally based on qualitative analysis of the altered land-sea thermal contrast (Man and Zhou, 2014; Man et al., 2012, 2014). The mechanisms related to the intensity of the weakened Asian summer monsoon, and other connected factors on explaining the hydrological effect of volcanic eruptions, are controversial questions that remain to be investigated. These will be carried out in chapter 3 and 4.

1.3.3 Asymmetric volcanic aerosol distribution and precipitation

Climatic impacts of volcanic eruptions depend on the distribution of volcanic aerosols and the associated radiative forcing structures (Toohey et al., 2019; Yang et al., 2019). Haywood et al. (2013) first reported the potential inverted climate effects of the asymmetric volcanic aerosol distributions (more aerosols concentrated over a single hemisphere) may have on Sahelian precipitation. Three of the four driest Sahelian summers were found to be preceded by substantial NH volcanic eruptions. They further used model simulation to test the climate effects of stratospheric aerosol injections in different hemispheres, and found that more stratospheric aerosol loadings concentrated over NH made Sahelian drier, but the wetting effects are shown when aerosols are concentrated over southern hemisphere (SH). Iles and Hegerl (2014) showed similar results after studying several volcanic eruption cases in recent centuries. Later, Colose et al. (2016a) and Zuo et al. (2018) found an inverted response of tropical hydroclimate to different superposed hemispheric volcanic eruptions in the last 1000 years. These studies, based on either observation or model simulation, all suggest different climate impacts of interhemispherically asymmetric volcanic aerosols, which are probably caused by the movement of the ITCZ towards the warmer hemisphere with less volcanic aerosol loading (Colose et al., 2016a; Haywood et al., 2013; Iles and Hegerl, 2014; Zuo et al., 2018).

Since the ITCZ is connected to the Asian summer monsoon (Yancheva et al., 2007), volcanic eruptions in different hemispheres may lead to inverted hydrological effects in the Asian monsoon region. Using proxy reconstruction data MADA and a historical drought disaster records-based index, Zhuo et al. (2014) found that volcanic aerosols injected into the NH led to significant drying effects in China, but a slight wetting effect after being injected into the SH. Liu et al. (2016) found a similar inverted climate effect of asymmetric VAI on Asian summer monsoon as well as on global monsoon precipitation. These studies used volcanic classifications based on the volcanic forcing index, which has much smaller aerosol concentration in SH compared to that in NH. This brings uncertainty with the conclusion. So far, only temporal analysis was done in Liu et al. (2016) for volcanic classifications with asymmetric aerosol loadings in two hemispheres. The hydrological effect of the volcanic eruption in different hemispheres has not yet been intensively investigated, especially on the spatial distribution of the climate impacts. This will be carried out in chapter 4 and 5.

1.3.4 Tropical and extratropical eruption and climate

Tropical eruptions were commonly thought to have larger climate effects than extratropical or high-latitude eruptions (Myhre et al., 2013; Schneider et al., 2009). The volcanic aerosols

injected into the stratosphere from the tropic was believed to be able to transport to both hemispheres and finally reach both poles. This generates larger areas of aerosol clouds and lasts longer in the stratosphere, thus bringing larger and longer climate effect (Schneider et al., 2009). Based on this hypothesis, previous reconstruction of volcanic forcing assumed a shorter lifetime of aerosols injected by extratropical volcanic eruptions (Ammann et al., 2007; Gao et al., 2008). Thus, comparing to tropical eruptions, model results suggested shorter cooling and less severe reduction of tropical precipitation after high-latitude eruptions (Schneider et al., 2009). Using both ice-core and tree ring-based proxy reconstruction and model simulation, Toohey et al. (2019) found larger climate effects after extratropical eruptions than tropical eruptions. They pointed out that the volcanic forcing from tropical eruptions was overestimated in volcanic forcing indices, this can result in an underestimation of climate effects from extratropical eruptions. This leads to the following question: what different climate effects do tropical and extratropical volcanic eruptions have temporally and spatially? This question will be investigated in chapter 5.

1.4 Volcanic eruption and El Niño/Southern Oscillation

In studying the climate effect of volcanic eruptions, the climate system has interannual variability that might mask or mimic volcanic signal (Kirchner and Graf, 1995). Particularly, the variation of the El Niño/Southern Oscillation (ENSO), which must be considered as they have similar amplitudes and timescales (Robock, 2015). This concern applies especially to the Asian monsoon region, where ENSO affects regional temperature and precipitation variation through various mechanisms over the year (Ding and Chan, 2005).

The question, whether there is a connection between volcanic eruption and ENSO events, has long been explored but remains unclear. Some studies suggest that there is little connection (Ding et al., 2014; Robock and Y., 1994), but other studies found various correlation between volcanic eruptions and ENSO event (Adams et al., 2003; Mann et al., 2005; McGregor and Timmermann, 2011). Using independent proxy reconstruction data on volcanism and climate, Adams et al. (2003) found a significant El Niño-like response for several years to explosive tropical volcanic eruptions in the past several centuries. Using the Zebiak-Cane model of the tropical Pacific coupled ocean-atmosphere system, Mann et al. (2005) simulated a significant tendency towards El Niño after explosive tropical eruptions over the past 1000 years. However, using the National Center for Atmospheric Research (NCAR) Community Climate System Model (CCSM), version 3, McGregor and Timmermann (2011) found an increasing likelihood of a La Niña event in the year after an eruption. Studies also showed that volcanic eruptions can affect the evolution of ENSO,

but also with many contradictory findings (Li et al., 2013; Maher et al., 2015; Wang et al., 2017). Employing a seven-century-long ENSO reconstruction, which was based on 2,222 tree ring chronologies, Li et al. (2013) found anomalous El Niño-like response in the year of large tropical eruptions, followed by anomalous La Niña tendency one year after the eruptions. Using large ensemble members from historical experiment of CMIP5, Maher et al. (2015) found an increased tendency toward El Niño after an eruption but toward La Niña three years later. Using Bergen Climate Model, Wang et al. (2017) found that ENSO has a negative-positive-negative response to strong tropical volcanic eruptions.

In addition, recent studies suggest that the effect of a volcanic eruption on ENSO depends on some factors like the latitude and the season of the volcanic eruption as well as the initial state of the ENSO (Liu et al., 2018; Pausata et al., 2015; Predybaylo et al., 2017; Stevenson et al., 2016). Pausata et al. (2015) simulated a high latitude eruption in NH, and found an El Niño-like anomaly after the eruption, which results from the southward movement of ITCZ, followed by the weakening of the trade wind in the western and central part of equatorial Pacific Ocean. Stevenson et al. (2016) found a hemispherical dependent relationship between volcano and ENSO. Specifically, they found a tendency toward El Niño after the superposed NH and tropical volcanic events but toward La Niña after superposed SH volcanic events in the last millennium. Liu et al. (2018) found similar results with both model simulation and analysis on proxy reconstructions of volcanism and ENSO indices. Employing the Geophysical Fluid Dynamics Laboratory Climate Model Version 2.1 (GFDL-CM2.1), Predybaylo et al. (2017) tested the effect of Pinatubo-size eruption on ENSO and suggested a dependence of an increased probability of El Niño on the initial condition of ENSO and the season of volcanic eruption. Specifically, they found statistically significant El Niño response one year after the eruption for cases of central or eastern Pacific El Niño and neutral phases, whereas no response for La Niña case. They also found a more pronounced El Niño responses to eruptions in summer than that in winter and spring. The main feedbacks to explain the effects include the ocean dynamical thermostat and wind changes due to the land-ocean temperature gradients. These contradictory findings show that the relationship between volcanic eruption and ENSO remain to be a large controversial problem. This will be investigated in chapter 5.

1.5 Objectives and outline

The following main questions will be investigated in this study:

Question 1: What are the similarities and discrepancies between proxy and model on reflecting volcanic eruptions' spatio-temporal hydrological effects in the subregions of the Asian monsoon region?

Question 2: Is the multi-model ensemble mean (MMEM) of CMIP5 able to reproduce volcanic eruptions' hydrological effects in the Asian monsoon region?

Question 3: What is the mechanism behind the hydrological effects of the explosive volcanic eruptions in subregions of the Asian monsoon region?

Question 4: Are there different hydrological responses to different hemispheric volcanic aerosol injections?

Question 5: What hydrological effects do different latitudinal volcanic eruptions have in the Asian monsoon region?

Question 6: What connection have different latitudinal volcanic eruptions with ENSO variation?

Question 7: What is the mechanism of the climate response to different latitudinal volcanic eruptions?

This thesis is arranged into 6 chapters. Chapter 2 describes the data and methods used in this study, followed by chapter 3, which deals with the question 1 to 2. It transfers model temperature and precipitation data to drought indices, and compares with the hydrological proxy reconstruction data on reproducing the spatio-temporal hydrological effects of explosive volcanic eruptions in subregions of the Asian monsoon region. Chapter 4 focuses on questions 3 and 4, which used varies variables of CMIP5 model output, to explore the mechanism of different hydrological effects in westerlies and monsoon-dominated subregion of Asia. Questions 5 to 7 will be discussed in chapter 5, which addresses with large ensemble members of model simulations. Firstly, it presents the climate effects of different latitudinal volcanic eruptions in the Asian monsoon region, and then shows the variation of ENSO after these different eruption cases. Finally, it tries to explain the potential mechanism of these climate variations to different latitudinal volcanic eruptions. The conclusions and implications of the results, including the outlook of future researches, are shown in chapter 6.

Chapter 2

Data and Methods

In this chapter, the volcanic forcing reconstruction indices are introduced firstly, followed with the introduction of the hydrological reconstruction data and the model data. Then the methods used in this study are described. The introduction of EVA, MPI-ESM-LR and the experiment setup of the model simulations are given in the final part of this chapter.

2.1 Volcanic forcing data

As one of the main natural forcing sources, volcanic forcing is important for studying the climate variation. The reconstruction of historical volcanic forcing is the basis in model simulations on studying the climate variation of longer periods. Researchers have reconstructed the volcanic forcing of the past few centuries (Ammann et al., 2007; Ammann and Naveau, 2003; Robock and Free, 1995) to be used in model simulations. In the last decade, with more ice cores available from both Arctic and Antarctica, endeavors were made by Gao et al. (2008) and Crowley et al. (2008) to extend the volcanic forcing reconstruction to a millennium scale. These two volcanic forcing indices, referred as GRA (Gao et al., 2008) and CEA (Crowley et al., 2008) volcanic forcing, which were suggested by PMIP3/CMIP5 as the only two adopted volcanic forcing dataset in the “last millennium (LM)” experiment (Schmidt et al., 2011), have been widely used in the research community. Sigl et al. (2015) produced the current longest volcanic forcing reconstruction back to the last 2500 years, which was not only based on multi-parameter measurement of ice cores, but also tree-rings in order to improve the dating of the volcanic events. More recently, Toohey et al. (2016) compiled a program, called the Easy Volcanic Aerosol (EVA), to generate volcanic forcing files. Adopting the identified volcanic events and related sulfate injection magnitude in Sigl et al. (2015), Toohey and Sigl (2017), by using the EVA module, produced the volcanic forcing dataset “eVolk2k” for paleoclimate simulation of the last 2000 years. These two recently

developed volcanic forcing datasets are adopted as the only two volcanic forcing datasets to be used in the “LM” experiment of the PMIP4/CMIP6 project.

In order to study the climate response of historical volcanic eruptions, we used output that is available from the state-of-the-art models from the “LM” experiment of PMIP3/CMIP5. Since the GRA (Gao et al., 2008) and CEA (Crowley et al., 2008) volcanic forcing datasets were used in the model simulations, they were adopted in this study to construct the volcanic classifications. GRA volcanic forcing reconstruction (also referred to as IVI2 in Gao et al. (2008)) was an extension of the ice-core volcano index (IVI, Robock and Free (1995)). It extends the IVI in 1850 - 2000 CE to the period of 500 CE to 2000 CE, based on 53 ice cores from both the Arctic and Antarctica. To reconstruct the three-dimensional volcanic forcing index as a function of month, latitude and altitude, they identified the volcanic signals with the peaks that exceed a magnitude of twice the local 31-year running median of the sulfate measurements after removing the background variation, and adjusted the dating of volcanic events based on these potential signals in ice cores. Ice cores have peaks in different years that might indicate the volcanic event. For the less well-documented events tracing back further in history, it has large uncertainty on determining the eruption date. They tried to narrow down the dating uncertainty through cross-core comparison and adopting historical records. After having identified the volcanic events, they calculated their Arctic or Antarctic mean volcanic sulfate deposition, and then calculated the amount of stratospheric sulfate injection globally as well as in each hemisphere. This is a variable that closely relates to the climate impact of volcanic eruption. After this, they produced the monthly and spatially dependent volcanic forcing index with stratospheric transport parameterization and function, assuming a linear relationship between total stratospheric sulfate aerosol load and global aerosol optical depth (AOD). April is assumed to be the month for eruptions of those identified unknown volcanic events. The volcanic aerosols evolved during the first four months after an eruption with a linear buildup of the total aerosol mass and then on exponential decrease with a global mean e-folding time of 12 months. They also interpolated the vertical distribution of volcanic aerosols, assuming that all the volcanic events have the same vertical distribution as the 1991 Pinatubo eruption. There are uncertainties coming from the assumptions made in the reconstruction process, but generally, the uncertainty is decreased compared to earlier studies (Gao et al., 2008).

CEA (Crowley et al., 2008) is the other adopted volcanic forcing reconstruction by the “LM” experiment of the PMIP3/CMIP5. This is a four-equal-area latitude band of AOD and effective radius reconstruction that covers the period of 800 CE to 2000 CE. The technical details of the reconstruction process were given in Crowley and Unterman (2013). It is primarily based on sulphate records of 25 ice cores from both Antarctic and Greenland. It

uses similar methods to Gao et al. (2008), with some different assumptions in determining the eruption date and the composite depositions in Greenland and the Antarctica, and then measures the stratospheric sulfate flux of historical volcanic eruptions in each hemisphere. For most of the unknown eruptions, it was assumed that January 1 was the eruption date, if an ice core indicates largest sulphate values in two years after the eruption, then the start date was set to July 1. They paid attention to the uncertainties, which come from the Icelandic eruptions and tropical eruptions that have only unipolar ice core records from either Antarctic or Greenland. Different growth curves of the aerosols were used for high and low-latitude eruptions, and satellite measures were adopted to validate the forcing reconstruction. The time evolution of the aerosol perturbation was assumed to be a linear increase in AOD for 5 months, lasting for another 3 months and then decreased with an e-folding lifetime of 1 year for tropical eruptions. This assumption was based on the satellite measurement of 1991 Pinatubo eruption. For explosive volcanic eruptions larger than the 1991 Pinatubo eruption, it was considered that larger collisions between aerosol in larger particle size will reduce the shortwave radiation forcing, a $2/3$ power scaling was applied when calculating the AOD. Thus, the CEA has smaller forcing for the explosive eruptions compared to the GRA volcanic forcing reconstruction. The dating accuracy was considered to be within 1 year after 1104 CE and 2 years before 1104 CE (Crowley and Unterman, 2013).

Sigl et al. (2015) produced the most recent reconstruction of historical volcanism in the past 2500 years based on three Greenland and two Antarctica ice cores as well as a series of tree ring chronologies. Based on precise age markers from recently available ^{14}C measure data of tree rings, Sigl et al. (2015) found a seven years of dating offset in previous ice core chronologies before 1000 CE. They revised the ice core chronologies based on these time markers and other evidence from tree rings, radionuclides, tephra analyses, and historical accounts. Together with new multi-parameter measure of ice cores, they improved the dating accuracy of past volcanic events and extended the reconstruction of volcanic aerosol deposition for both polar ice sheets to 2500 years.

2.2 Tree-ring based hydrological reconstruction data

In order to reflect the hydrological condition of the past years in the Asian monsoon region (AMR, 8.75°S – 56.25°N and 61.25°E – 143.75°E), the Monsoon Asian Drought Atlas (MADA, Cook et al. (2010)) is adopted in this study. This is the first hydrological reconstruction dataset in the AMR that has annual recordings from 1300 CE to 2005 CE and $2.5^{\circ} \times 2.5^{\circ}$ spatial resolution. It is a seasonalized hydrological reconstruction dataset for the boreal summer (June-July-August) monsoon season. MADA was reconstructed from

327 hydroclimatically sensitive tree ring chronologies over 300 sites of the forested areas of Monsoon Asia, combined with the widely used Palmer Drought Severity Index (PDSI, Dai et al. (2004)). Hereafter, I refer to MADA as MADA PDSI in this thesis. The same as PDSI, positive MADA PDSI values represent wet conditions while negative values stand for dry conditions. It indicates drought when MADA PDSI falls below -0.5 while reflects flood when it is over 0.5. Since its release, it has been widely used as a reference data set to study the hydrological response to historical volcanic eruptions (Anchukaitis et al., 2010; Stevenson et al., 2017, 2016; Zhuo et al., 2014).

2.3 Model data

2.3.1 PMIP3/CMIP5 “last millennium” experiment

The Coupled Model Intercomparison Project (CMIP) organized under the World Climate Research Programme’s (WCRP) Working Group on Coupled Modelling (WGCM) started in 1995, which is to better understand past, present and future climate changes arising from natural, unforced variability or in response to changes in radiative forcing in a multi-model context. It becomes a central element of national and international assessments of climate change after five phases of development (Eyring et al., 2016). In this study, we use the most newly available output from the fifth phase of the project (CMIP5, Taylor et al. (2012)). To study the hydrological effects of the volcanic eruption in the past hundred years, we adopted all the available model output from the “LM” experiment of CMIP5, which was organized by PMIP3. The participating model groups had to follow the protocol of PMIP3, which constrained the boundary conditions of the model simulation with the prescribed forcing dataset. As suggested in Schmidt et al. (2011), one of the two volcanic forcing data sets - GRA (Gao et al., 2008) and CEA (Crowley and Unterman, 2013) – could freely be chosen by nine modelling groups, which conducted the “LM” experiment. We separated models into two groups, and calculated the multi-model ensemble means (MMEMs) based on the adopted volcanic forcing data sets. To keep the same number of models involved in the two groups of MMEMs, and because of some error in the dataset of FGOALS-S2 model, we neglected it and only used the other eight models. Except for GISS-E2-R model which has nine ensemble members (three members used GRA, but with doubled forcing, three members used CEA forcing and three members without volcanic forcing), the other seven models only have one member. As shown in table 2.1, we adopted six members of four models in each group. Only GISS-E2-R model has three members, which might dominate the ensemble

Table 2.1 PMIP3/CMIP5 Model ensembles used in the study

Model	Ensemble member	Resolution (lat°x lon°)	Vertical level	Volcanic forcing	Reference
CCSM4	r1i1p1	0.94x1.25	26	GRA	Gent et al. (2011)
BCC-CSM1-1	r1i1p1	2.8x2.8	26	GRA	Wu et al. (2013)
IPSL-CM5A-LR	r1i1p1	1.9x3.75	39	GRA	Dufresne et al. (2013)
GISS-E2-R	r1i1p122	2x2.5	40	GRA	Schmidt et al. (2014)
GISS-E2-R	r1i1p125	2x2.5	40	GRA	Schmidt et al. (2014)
GISS-E2-R	r1i1p128	2x2.5	40	GRA	Schmidt et al. (2014)
MPI-ESM-P	r1i1p1	1.865x1.875	47	CEA	Giorgetta et al. (2013)
FGOALS-gl	r1i1p1	5x4	26	CEA	Zhou et al. (2008)
MIROC-ESM	r1i1p1	2.8x2.8125	80	CEA	Watanabe et al. (2011)
GISS-E2-R	r1i1p121	2x2.5	40	GRA	Schmidt et al. (2014)
GISS-E2-R	r1i1p124	2x2.5	40	GRA	Schmidt et al. (2014)
GISS-E2-R	r1i1p127	2x2.5	40	GRA	Schmidt et al. (2014)

Note: The ensembles in bold constitute two set of multi-model ensemble means where only one ensemble from GISS-E2-R model is included.

mean. Considering this, two sets of MMEMs with four members, including only one member from GISS-E2-R, are tested. The four members are shown in bold in table 2.1.

2.3.2 Last Millennium Ensemble

The Last Millennium Ensemble (LME, Otto-Bliesner et al. (2016)) is a series of Last Millennium community experiments conducted by the Community Earth System Model (CESM) paleoclimate-working group at NCAR. It used the same climate forcing reconstructions (Schmidt et al., 2011) as CMIP5 for a large ensemble of LM simulations with 10 ensemble members of “full forcing” simulations and 5 ensemble members of each simulation with individual forcing separately. The simulations were performed using the 1.1 version of CESM with the Community Atmosphere Model version 5 (CESM1(CAM5), Hurrell et al. (2013)). This is a fully coupled global climate model that has approximately 2° resolution in the atmosphere and land components and 1° resolution in the ocean and sea ice components. In this study, the multi-member mean calculated from the five ensemble members of the “volcanic only” experiment is also employed. The GRA volcanic forcing reconstruction (Gao et al., 2008) was adopted as the volcanic forcing dataset. Other forcing including solar variability, land use, GHGs and orbital changes were fixed to the same value as in 850 CE.

2.4 Methods

2.4.1 Hydrological indices

The proxy reconstruction data MADA PDSI is used to reflect the hydrological condition in the summer. As the most prominent index of meteorological drought, PDSI has been used worldwide. It measures the departure of any given year's moisture balance from the background state, which is obtained from a water balance model to produce a moving mean value (Dai et al., 2004). To better compare between proxy reconstruction and model, CMIP5 "LM" experiment outputs were regridded to the same spatial resolution as MADA PDSI. Then, using the MATLAB program produced by Jacobi et al. (2013), model precipitation and temperature data, together with latitude and water-holding capacity, are transferred into PDSI. Finally, the multi-model ensemble mean of PDSI is calculated. Hereafter, I refer to it as CMIP5 PDSI in this thesis. It represents normal conditions when CMIP5 PDSI is between -0.5 and 0.5, and indicates incipient drought when CMIP5 PDSI falls below -0.5 and wet spell when CMIP5 PDSI goes above 0.5.

PDSI is based on temperature, precipitation, latitude and soil moisture content in the calculation. This makes it hard to differentiate the contribution of temperature and precipitation. Therefore, we adopted another widely used drought index: 12-months of Standardized Precipitation Index (SPI12, McKee et al. (1993)). It is transferred only from model precipitation data and shows the difference of precipitation from the mean for 12 months divided by the standard deviation. We choose SPI12 as it represents long-term hydrological drought, which occurs after many months of meteorological drought. It indicates evident low water supply, especially in streams, reservoirs, and groundwater levels. This indicates the societal impact of continuous meteorological drought. Different from PDSI, negative and positive values indicate specific drought and wet conditions. It indicates mild drought once SPI12 falls below zero. The same as CMIP5 PDSI, the multi-model ensemble mean of SPI12 from CMIP5 "LM" experiment is calculated and referred to as CMIP5 SPI12 in this thesis. MADA PDSI only reflects the hydrological condition of the summer JJA season. To keep model data the same as MADA PDSI, summer JJA mean of CMIP5 PDSI and CMIP5 SPI12 were analyzed in this study.

2.4.2 Volcanic classifications

MADA PDSI has recordings in 1300-2005 CE, while PMIP3/CMIP5 "LM" experiment covers the period of 850-1849 CE. The overlapped years in 1300-1849 CE were chosen as our core study period. To compare the hydrological effect of explosive volcanic eruptions

between proxy and model simulations, the explosive volcanic eruptions in 1300-1850 CE that injected more sulfate into stratosphere of NH than that of 1991 Pinatubo eruption were picked out. Every volcanic event has over 15 Tg of NH sulfate aerosol injection based on the GRA volcanic forcing index; to explore the mechanism of hydrological response to interhemispherically asymmetric volcanic aerosol injection (VAI), the volcanic events that has stratospheric aerosol injection only into SH were also picked out. Just by coincidence, based on these two criterions, each of the 12 events was picked out and classified as GNH and GSH classifications. Similarly, based on CEA volcanic forcing index, the CNH classification was constructed with volcanic events that released sulfate aerosol flux into the NH over 11 kg/km^2 , which includes 18 volcanic events. The eruption year and the stratosphere aerosol magnitude of the three volcanic classifications are shown in Table 2.2. The difference between the GNH and GSH volcanic classifications reflects their uncertainties originate from the volcanic forcing reconstructions.

2.4.3 Superposed Epoch Analysis with Monte Carlo significance test

To isolate volcanic effects from other random fluctuations, a superposed epoch analysis (SEA, Haurwitz and Brier (1981)) was conducted. SEA is the average of the columns that line up the response index values in fixed time relation to the key event years, which is commonly used in studies for investigating volcanic impacts on climate (Adams et al., 2003; Liu et al., 2016; Zambri et al., 2017; Zhuo et al., 2014). After the pretreatment of the hydrological data and classifications, we conducted SEA on MADA PDSI, CMIP5 PDSI and CMIP5 SPI12 for the 11 years (-5 to 5) surrounding the eruption year (year 0). To study the significance of the hydrological effects, we conducted Monte Carlo model tests (Adams et al., 2003) with 10000 and 1000 resampling of MADA PDSI / CMIP5 PDSI / CMIP5 SPI12 to regional average in temporal analyses and each grid in spatial analyses, based on the null hypothesis that there is no relationship between volcanoes and hydrological conditions. Each volcanic event is randomly reassigned a new eruption year in the study period, and then the average values of the hydrological indices are calculated for the 11 years. This builds a random distribution, against which our SEA results are considered to be statistically significant at the 95% (99%) confidence level when they exceed the 95% (99%) range of the Monte Carlo results.

2.4.4 Correlation analysis

To study the potential mechanism of the hydrological effects, we investigated the correlation relationship between temperature, precipitation and the radiation, heat and evaporation related

Table 2.2 volcanic classifications, identified eruption years and stratospheric aerosol magnitudes

Eruption year (CE)	GRA ^a (sulfate aerosol mass, Tg)		CEA ^b (sulfate aerosol flux, kg/km ²)
	GNH	GSH	CNH
1307		1.18	
1316		1.83	
1328	19.7		
1344			13.6
1358		1.09	
1381		5.27	
1441			11.8
1452	44.6		
1459	21.9		22.1
1474		3.32	
1534		3.86	
1553			13.6
1561			12.2
1585	24.2		22.0
1593		9.54	
1600	46.1		35.0
1619		5.23	
1620			12.4
1641	33.8		17.6
1668			23.3
1673			13.3
1693		27.1	
1694			15.1
1711		3.86	
1719	31.5		
1738		3.34	
1740			17.5
1783	93.0		17.9
1794		1.88	
1809	27.6		22.2
1815	58.6		32.2
1831	17.0		17.5
1835	26.4		14.3

Note: ^aAerosol mass is based on GRA volcanic forcing from Gao et al. (2008). ^bAerosol flux is based on CEA volcanic forcing from Crowley et al. (2008). Years in bold are the volcanic events included in both GNH and CNH classifications.

variables, using the widely used Pearson cross correlation (r) as the indicator. We calculated r in each grid between variables over 11 years before and after the aerosol injection, and then calculated the average r -value of the Asian monsoon region. This helps to identify the key factors related to the hydrological processes. To explore the mechanism of the hydrological responses, the spatial distributions of these key factors were investigated.

2.4.5 Monsoon and ENSO indices

We adopted two indices to better quantify the East and South Asian summer monsoon variation. Following the recommendation in Wang et al. (2008), to assess the strength of EASM, the East Asian summer monsoon index (EASMI, defined as the difference of the zonal wind at 850 hPa between over the region 5°N-15°N, 90°E-130°E and 22.5°N-32.5°N, 110°E-140°E) in Wang and Fan (1999) was used, as it outperforms other 24 indices in reflecting the summer precipitation distribution. For the South Asian summer monsoon index (SASMI), we used the definition of Webster and Yang (1992), which is defined as the difference between the zonal wind at 850 hPa over the region 0°-20°N, 40°E-110°E and the zonal wind at 200 hPa over the region 0°-20°N, 40°E-110°E. This index is widely used to assess the large-scale intensity of the southern ASM.

To define the El Niño and La Niña events, the Niño 3.4 index and the Oceanic Niño Index (ONI) are the most commonly used indices. ONI is the operational definition used by the National Oceanic and Atmospheric Administration (NOAA). We used it in this study to quantify the ENSO variation. The ONI calculates a 3-month running mean of the sea surface temperature (SST) anomaly of 5°N-5°S, 120°W-170°W region, which is the same region used in the Niño 3.4 index. To be classified as an El Niño or La Niña event, the anomalies must exceed +0.5°C or -0.5°C for at least five consecutive months.

2.5 Model simulation using EVA and MPI-ESM

2.5.1 Easy Volcanic Aerosol forcing generator

To include the impact of volcanic eruptions in the climate model simulation, Toohey et al. (2016) compiled the easy volcanic aerosol (EVA) module in order to generate volcanic aerosol forcing as a function of time, latitude, height and wavelength after parameterizing the attributes of volcanic eruption. Based on a parameterized three-box model of stratospheric aerosol transport and simple scaling relationships, EVA transfer stratospheric sulfate mass to mid-visible (550nm) AOD and effective radius as volcanic forcing input for climate model simulations. The structure and parameterization of the EVA module is fixed mainly based on

the satellite-based reconstruction of stratospheric aerosol properties following 1991 Pinatubo eruption, but also reference to other volcanic forcing reconstructions in millennial-timescale including the 1815 Tambora eruption. The simplification of EVA module neglects the impact of polar vortex and the vertical variations in the stratosphere. It also does not consider the height of stratospheric sulfur injection; thus, it cannot reproduce all the features of actual volcanic forcing (Toohey et al., 2016). However, using the EVA module, one can easily modify different aspects of aerosol properties through a specification of the eruption year, month, sulfate injection magnitude and hemispheric ratio. This flexibility on generating volcanic forcing files makes it well suited for idealized studies to fulfill various study purposes through conducting experiments in model simulations (Toohey et al., 2016).

2.5.2 Max-Planck-Institute Earth System Model

The Max-Planck-Institute Earth System Model (MPI-ESM) is a fully coupled general circulation model (Giorgetta et al., 2013). As shown in figure 2.1, MPI-ESM is currently based on the components of ECHAM6 (Stevens et al., 2013) for the atmosphere and MPIOM Jungclaus et al. (2013) for the ocean as well as JSBACH (Reick et al., 2013; Schneek et al., 2013) for terrestrial biosphere and HAMOCC5 (Ilyina et al., 2013) for the ocean's biogeochemistry. The components are coupled through the exchange of energy, momentum, water and carbon dioxide between the atmosphere and the land as well as between ocean and biogeochemistry with a separate coupling program OASIS3 (Valcke, 2013). The time steps in the atmosphere and the ocean are 600 and 4320 s, respectively. In this study, we used the low-resolution (LR) version of MPI-ESM, which has been used for a wide range of CMIP5 simulations. The LR configuration has T63/1.9 horizontal resolution for the atmosphere and 47 hybrid sigma pressure levels to 0.01 hPa, which includes the stratosphere in the CMIP simulations. For the ocean component, MPI-ESM-LR has a bipolar grid with 1.5 resolution (near the equator) and 40 z-levels.

This version is based on the predecessor of MPI-ESM-LR. The largest improvement lies in the upgrade of the atmospheric general circulation model from ECHAM5 (Roeckner et al., 2006) to ECHAM6 (Stevens et al., 2013). More details are described in Giorgetta et al. (2013). Because of its high simulation efficiency (Roeckner et al., 2006), MPI-ESM-LR with ECHAM5 as its atmospheric component has been extensively used in studying the variation of the Asian summer monsoon (Guo et al., 2016; Man et al., 2012) and the response to volcanic eruptions (Man et al., 2014; Zhang et al., 2012). Studies on volcanic effects have also been performed with the newly updated version (Toohey et al., 2016) and even their impact on decadal prediction (Illing et al., 2018; Timmreck et al., 2016).

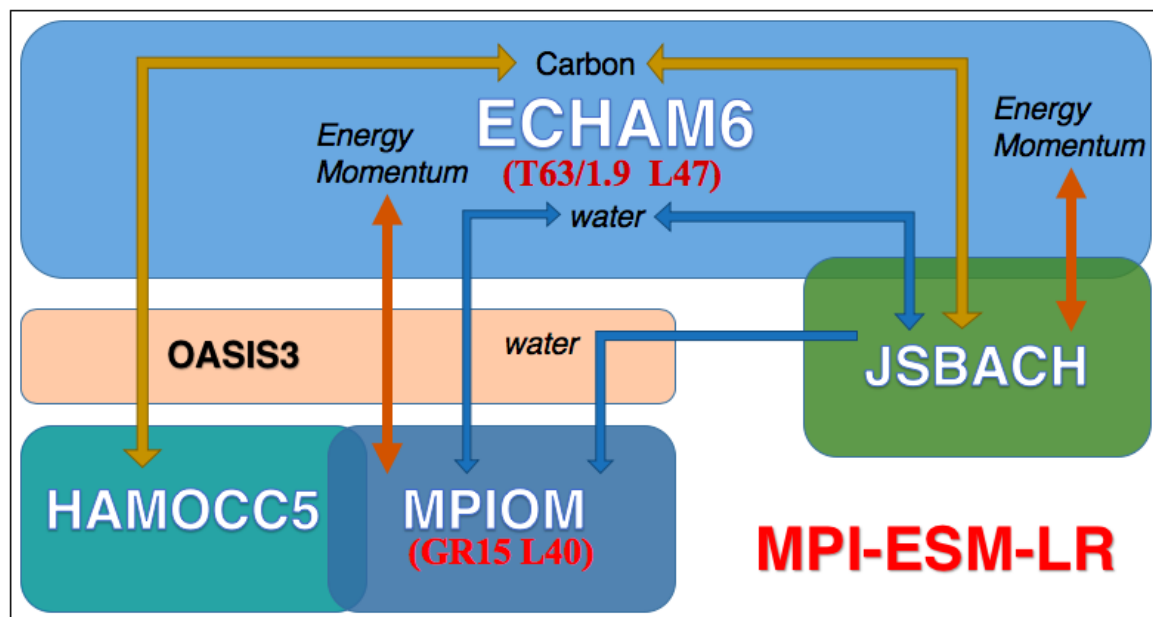


Fig. 2.1 Schematic view of MPI-ESM-LR. The colored boxes show the model components. ECHAM6, as the atmospheric general circulation model, is directly coupled to the JSBACH land model that describes physical and biogeochemical aspects of soil and vegetation. MPIOM, as the ocean general circulation model, includes the HAMOCC5 model for the marine biogeochemistry. OASIS3 is the coupler program used for aggregating, interpolating, and exchanging fluxes and state variables between ECHAM6 and JSBACH as well as MPIOM and HAMOCC. The coupler exchanges fluxes for water, energy, momentum, and carbon dioxide.

2.5.3 Experiment setup

To test the hydrological effect of volcanic eruptions in different hemispheres as well as tropical vs extratropical volcanic eruptions. We used MPI-ESM-LR model to do some sensitivity tests. Volcanic forcing data are produced from the EVA module, in which we set the eruption year and month to June 1991, the same as the 1991 Pinatubo eruption. Because the construction of EVA relies extensively on observational constraints, especially the observational records of 1991 Pinatubo eruption, it produces the volcanic forcing of 1991 Pinatubo eruption that matches the best among all the historical volcanic eruptions. The same as being used in Toohey et al. (2016), 9 Tg of total S injection was set. For different cases, different latitudes were set in the experiments. Specifically, we set 0° for the equatorial eruption (EQ case), and 30° N and 30° S for the Northern and Southern hemispheric eruption (NH and SH cases), respectively. For the NH and SH cases, an updated version of EVA was adopted. This new version fixed a minor bug which affected the spatiotemporal distribution of AOD for extratropical eruptions (through personal communication). Figure 2.2 shows the experiment setup of our simulation. The MPI-ESM-LR model we used here is the same as that used for the historical simulation of CMIP5. The spin up run was performed in the period of 1966-2012 CE, and then we performed 23 control runs (CTR) for the period of 1986-1995 CE without any volcanic eruption. For these 23 members, we calculated the ONI to study the ENSO variation. It represents neutral or weak ENSO condition when the value falls between -1 and 1. To rule out the concurrent effect of ENSO, we picked out 10 members with neutral or weak ENSO in the period of 1990-1992 CE, and performed three 10-member ensemble integrations of experiments for the EQ, NH and SH cases in the period of 1991-1996 CE. Because of the free-running spin-up simulations and the quantification of ENSO, the simulated years do not correspond to the real years.

We calculated multi-member mean of these experiments to study the hydrological effect of the volcanic eruptions at different latitudes. Table 2.3 shows the used simulations for analysis. Anomalies are calculated by subtracting the MEM of the control runs. The standard deviation (SD) of the control runs was calculated to indicate the significance of the temporal results. Two-tailed student-t tests at the 95% and 99% confidence levels were made for the significance of the spatial results.

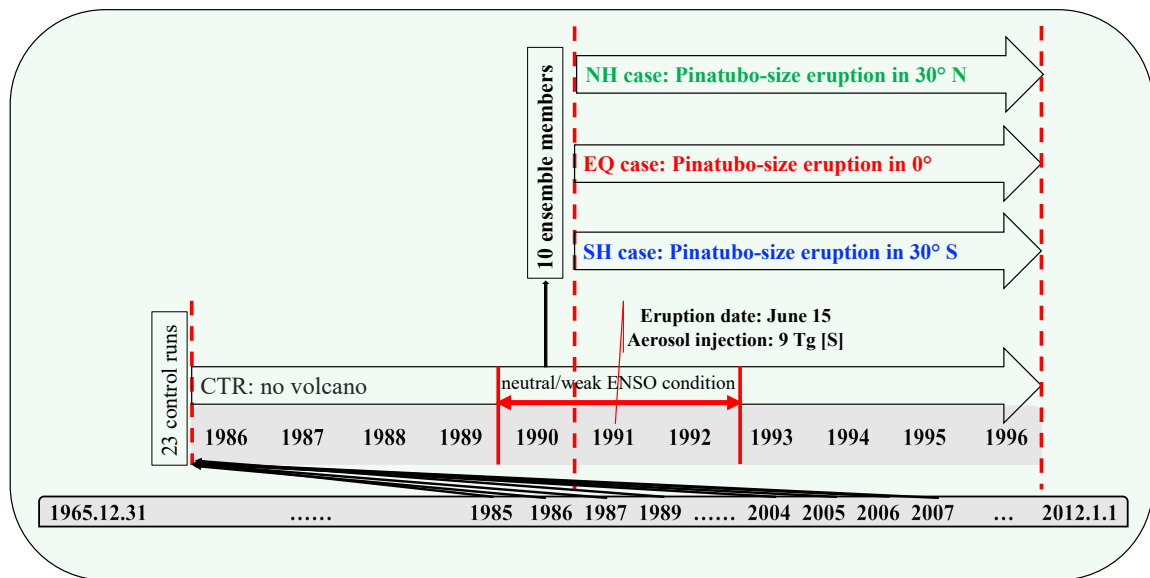


Fig. 2.2 Schematic view of the experiment setup. Simulations are performed using MPI-ESM-LR model, volcanic forcing are produced from EVA module.

Table 2.3 Summary of the simulations used for analysis.

Name	Ensemble members	Eruption (latitude)	Eruption date	Injected sulfate
CTR	10	/	/	/
NH	10	30° N	June 15, 1991	9 Tg
EQ	10	0°	June 15, 1991	9 Tg
SH	10	30° S	June 15, 1991	9 Tg

Chapter 3

Comparison of proxy and model on volcanic aerosols' hydrological effects in Asian westerlies and monsoon-dominated subregions

In this chapter, comparisons of volcanic aerosols' spatio-temporal hydrological effects were conducted between tree-ring based reconstruction and model simulations. The similarity and discrepancy of temporal variation and spatial distribution of the hydrological effects and the uncertainty of both data source are discussed.

3.1 Explosive volcanic classifications

The two adopted volcanic forcing reconstructions GRA (Gao et al., 2008) and CEA (Crowley et al., 2008) identified different volcanic eruption years and estimated different aerosol magnitudes. Since both have uncertainties, we adopted both indices and constructed two classifications to compare the hydrological effect of volcanic eruptions between proxy and model simulations. Figure 3.1 shows the classified volcanic events in 1300-1850 CE and their magnitudes as well as the related model ensemble members used in the MMEs. There are 12 volcanic events classified in the GNH classification based on the criterion that the aerosol magnitude is larger than the 1991 Pinatubo eruption (injected 15 Tg sulfate aerosol mass based on GRA index), the identified strongest eruption was in 1783 CE, which injected 93 Tg sulfate aerosol into the stratosphere of NH, while the weakest eruption was in 1831 which only injected 17 Tg sulfate aerosol. However, 18 events were included in the CNH

classification that are larger than 11 kg/km^2 of released sulfate flux by 1991 Pinatubo eruption in CEA index. The strongest and weakest eruptions were identified in AD 1600 and AD 1441, which released 35 and 11.8 kg/km^2 sulfate flux. Because of the different units used in the forcing reconstruction, we cannot directly compare their magnitudes. As shown here, the strongest and weakest eruptions of the analyzed period were identified in different years. Even for the volcanic events that have been identified in both volcanic forcing indices (shown in red in figure 3.1), the ranking of the injected aerosol magnitude were estimated to be different. Both volcanic forcing indices have uncertainties, and proxy reconstruction reflects the response to the real eruption and injected aerosol magnitude, it is difficult to accurately compare the modeled hydrological effects to the proxy reconstructions. Considering this, we could expect the different magnitude of the hydrological response, thus in our proxy-model comparison analysis, we concentrated more on the tendency of the spatio-temporal climate response to the volcanic perturbation than on the amplitude of the climate effect.

The response in the model simulation depends largely on the forcing used. In order to study the hydrological responses to the volcanic eruptions, the available models were separated into two groups based on the two adopted forcing indices and two MMEs were constructed. As shown in the green box of figure 3.1, only the GISS-E2-R model has adopted both volcanic forcing indices and performed three-member simulations with each volcanic forcing index. There are only 4 models in each group, in order to have a larger number of ensemble members, we adopted all the three available members of GISS-E2-R in our MMEMs. This may lead to a domination of the MMEMs by the GISS-E2-R model. In order to test the severity, we also constructed another two sets of MMEs, which only included one member of the GISS-E2-R model (take out the members in grey, only members in black are used for the tested MMEs).

For the models from both PMIP3/CMIP5 adopting GRA volcanic forcing index and LME, the GNH classification in 850-1849 CE that covered the whole period of the simulation was also tested. For the hydrological reconstruction data MADA PDSI, considering the dating uncertainty of volcanic forcing reconstructions, we also tested different volcanic classifications based on both GRA (Gao et al., 2008) and CEA (Crowley et al., 2008) volcanic forcing indices and the most newly reconstructed index Sigl et al. (2015) and three other classifications used by previous studies. The chosen volcanic eruption years of these tested volcanic classifications are shown in table 3.1.

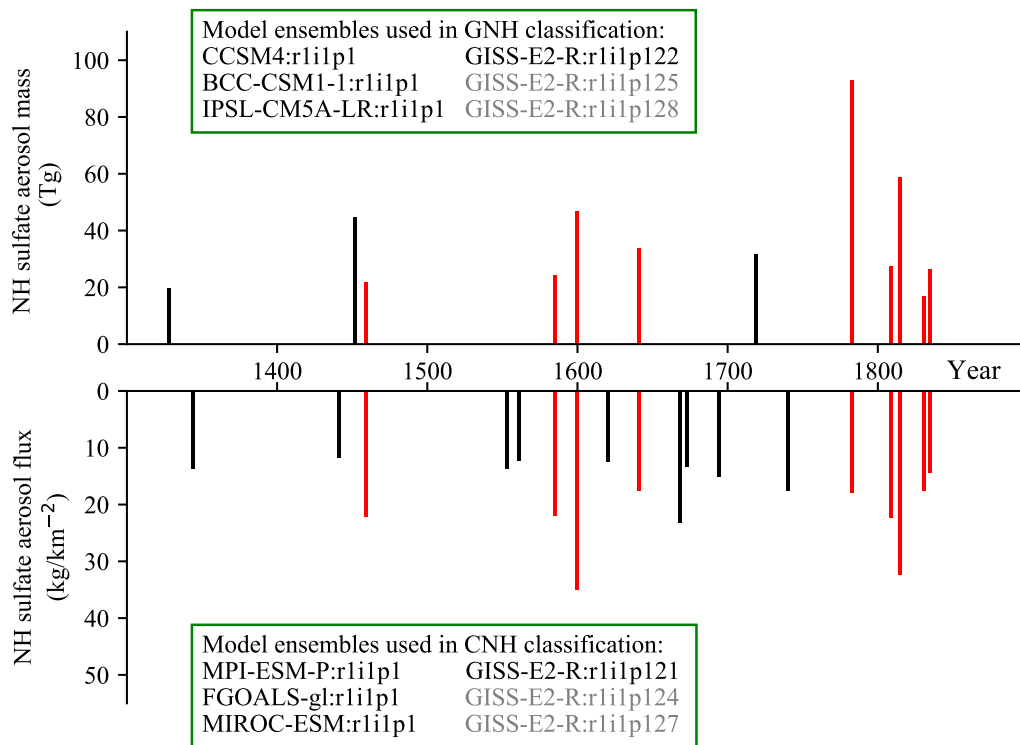


Fig. 3.1 Volcanic years and northern hemisphere volcanic aerosol injection in the GNH and CNH classifications. The red lines indicate that the volcanic events are included in both classifications. Model ensemble members used in the two classifications are shown in the green box, four model ensemble members in black were used in the test of another round of multi-model ensemble means.

Table 3.1 The volcanic classifications tested on the proxy reconstruction data and the included event years

Classification	Reference	Event year (CE)	Num.
GCNH ^a	Gao et al. (2008)	1328, 1344, 1441, 1452, 1459	21
	Crowley et al. (2008)	1553, 1561, 1585, 1600, 1620 1641, 1668, 1673, 1694, 1719 1740, 1783, 1809, 1815, 1831 1835	
SNH ^b	Sigl et al. (2015)	1345, 1458, 1601, 1641, 1695 1783, 1809, 1815, 1836	9
A07	Ammann et al. (2007)	1452, 1600, 1641, 1809, 1815	5
F07	Fischer et al. (2007)	1586, 1596, 1600, 1641, 1673 1809, 1815, 1823, 1831, 1835	10
AN03	Ammann and Naveau (2003)	1443, 1452, 1459, 1463, 1490 1504, 1512, 1522, 1554, 1568 1571, 1586, 1595, 1600, 1605 1619, 1622, 1641, 1660, 1665 1674, 1680, 1693, 1712, 1721 1728, 1737, 1744, 1749, 1752 1760, 1774, 1789, 1794, 1808 1813, 1823, 1831, 1835	39

Note: ^aCombination of both volcanic events in the GNH and CNH classifications. ^b Volcanic events that have larger global forcing and more sulfate in Greenland than that of the Pinatubo eruption in 1991 (-6.49 W/m² global volcanic forcing and 21.4 kg/km² aerosol in Greenland), selection is based on Sigl et al. (2015) reconstruction. The other three classifications follow that in Anchukaitis et al. (2010), but in order to avoid confusing their climate impacts, the events that follow a previous one within 3 years are removed in this study.

3.2 Subregions of the Asian monsoon region

In previous studies, proxy-model comparisons between MADA PDSI and models were conducted over the Asian monsoon region (Anchukaitis et al., 2010; Stevenson et al., 2017, 2016; Wegmann et al., 2014), no selection was made with regard to the regional difference of dominant climate or data reliability. Different hydrological conditions are shown on two sides of the modern Asian summer monsoon limit (figure 1.1), to the northwest are the westerlies-dominated arid areas, whereas to the southeast are the monsoon-dominated humid areas (Chen et al., 2008; Dando, 2005; Herzschuh, 2006). It is controlled by two monsoon subsystems - EASM and SASM, which are usually separated by 100°E longitude (Chiang et al., 2017; Herzschuh, 2006). Considering this, we also performed temporal analysis on two separated westerlies and monsoon-dominated subregions.

For the spatial comparison, in figure 3.2, the locations of the tree-ring chronologies (green dots) distribute irregularly, which might cause different reliability of MADA PDSI in different areas. According to the geographical distribution of Asia (Fan, 2017), the study area covers part of North Asia (NA), Central Asia (CA), and all the countries in East Asia (EA), South Asia (SA) and Southeast Asia (SeA). Considering the two monsoon systems, we separated the whole area into seven subregions (separated by purple boundary lines in figure 3.2) for a more detailed discussion. Western-East Asia (w-EA) is the subregion where has the most available tree-ring chronologies especially the ones dating back to 1300 CE (Cook et al., 2010). In monsoon-dominated subregion, SASM has more tree-ring chronologies, followed by EASM and SeA. In the westerlies-dominated subregion, several tree-ring chronologies are concentrated in the central part of NA, but most of them only date back to 1700 CE (Cook et al., 2010); w-SA and CA have fewer tree-ring chronologies.

3.3 Temporal comparison between proxy and model on hydrological effects of volcanic eruptions

3.3.1 Temporal response in the Asian monsoon region

The average temporal response of MADA PDSI, CMIP5 PDSI and CMIP5 SPI12 in the Asian monsoon region to GNH and CNH classifications are compared. Years before the eruption (year -5 to year -1) served as a reference of the climatological condition. As shown in figure 3.3 (a) MADA PDSI decreased in one year after the eruption (year 1) and significant drying effects are shown in two and three years after the eruption (year 2 and year 3). CMIP5 PDSI decreased promptly and sharply in the eruption year (year 0). The significant drying effects

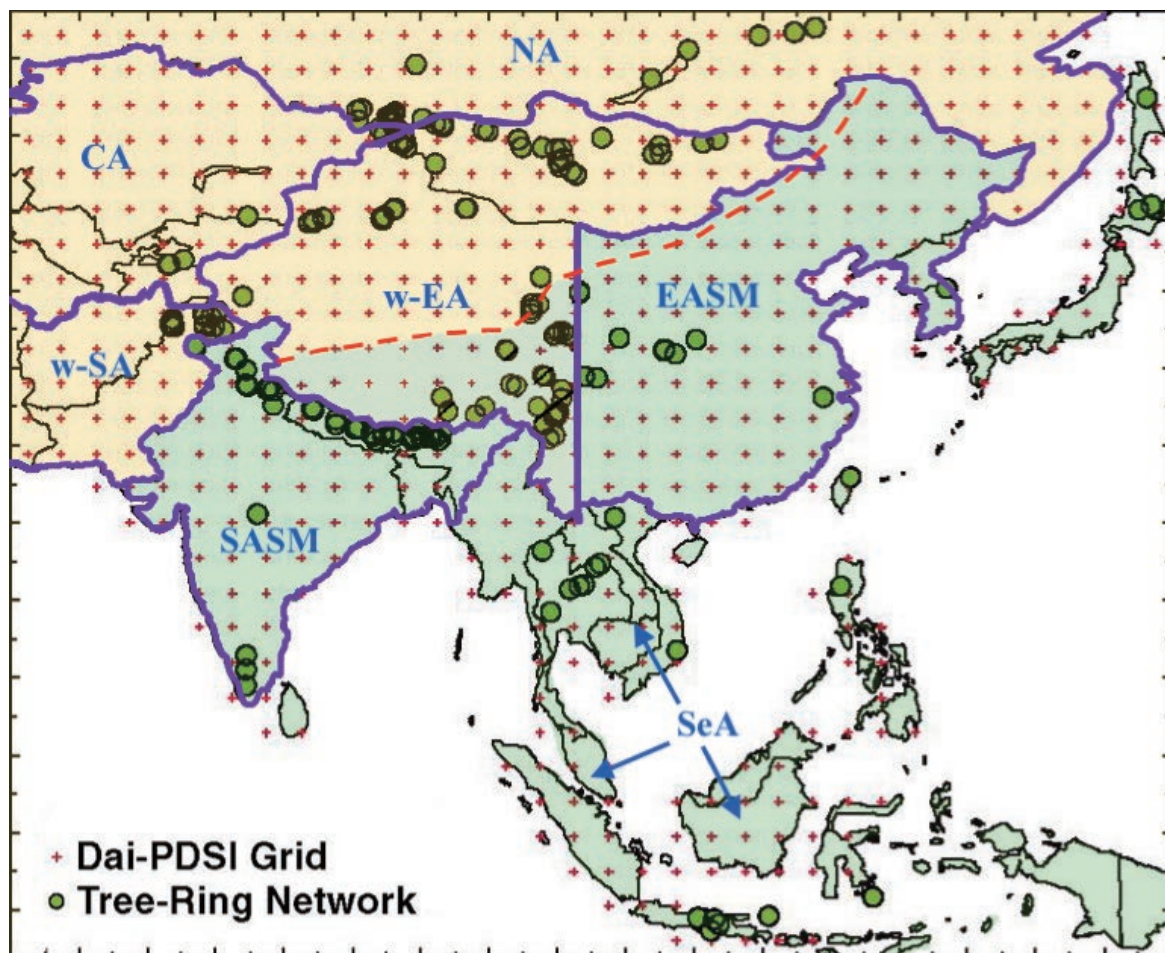


Fig. 3.2 The proxy reconstruction data MADA and the selected subregions. Modified from figure 1 of Cook et al. (2010). Red crosses show the 534 grid points. Green dots indicate the locations of the tree-ring chronologies. Seven subregions are divided by purple curves. Dashed red line indicates the modern Asian summer monsoon limit after Chen et al. (2008). Areas with yellow background indicate westerlies-dominated subregions: North Asia (NA), Central Asia (CA), western-South Asia (w-SA); areas with light green background indicate monsoon-dominated subregions: East Asian summer monsoon (EASM), South Asian summer monsoon (SASM) and Southeast Asia (SeA). Western-East Asia (w-EA) is the monsoon-westerlies transition zone.

lasted for three years, and gradually recovered to normal condition in year 4. Similarly, CMIP5 SPI12 also decreased rapidly in year 0 and year 1, after reaching the strongest drying effects in year 1, it gradually recovered in year 2 and turned to normal condition in year 3. This indicates an agreement between MADA PDSI and CMIP5 PDSI/SPI12 on the drying effects of the volcanic eruptions, although with one year of time lag in MADA PDSI compared to CMIP5 PDSI/SPI12, and the magnitude shown in CMIP5 PDSI/SPI12 are much larger than that in MADA PDSI. This is probably due to exaggerated two times of the GRA forcing used in the GISS-E2-R model. Meanwhile, differing from CMIP5 PDSI/SPI12, MADA PDSI indicates significant wetting tendency in one year before the eruption (year -1) and year 0 (figure 3.3 (a)). These values might be statistical outliers, which are not connected with volcanic eruptions.

Figure 3.3 (b) shows the hydrological response to the CNH classification. The response tendency is similar to that in the GNH classification, MADA PDSI increased before the eruption, and then decreased in year 1 and year 2; CMIP5 PDSI and CMIP5 SPI12 decreased promptly in year 0 and reach the lowest value in year 1, then gradually recovered from year 2. Comparing to the significant results (even at the 99% confidence level) in the GNH classification, the results are less significant in the CNH classification, but the magnitudes in MADA PDSI and CMIP5 PDSI/SPI12 are close to each other. Crowley and Unterman (2013) suggested that volcanic forcing in the GRA index is overestimated. When reconstructing the CEA index, they used scaling with two-thirds in order to calculate the forcing of the explosive eruptions which were larger than 1991 Pinatubo eruption. This scaling affects exactly the volcanic events included in the CNH classification and thus resulted in the minor hydrological response.

The exaggeration of the two times of the GRA forcing used in the GISS-E2-R model might cause the excessive climate response in the GRA-based group of CMIP5 MMEMs. LME (Otto-Bliesner et al., 2016) adopted the GRA forcing in the five ensemble member simulations. Analyses on the multi-member mean of the LME were carried out to test the effect. Since CMIP5 PDSI and CMIP5 SPI12 showed similar tendencies, tests were made only with PDSI, but for both the selected core period (1300-1849) and the whole period (850-1849) of the “LM” experiment. Hereafter, the multi-member mean PDSI from LME “volcanic only” experiment is referred to as LME PDSI in this thesis. As shown in figure 3.4, LME PDSI validates the similar drying effects in the eruption year, with LME PDSI decreased quickly in year 0 and the significant drying effects last to year 1 over both periods. CMIP5 PDSI shows excessive drying effects over the whole period, which is similar to that shown in figure 3.3 (a) for the selected period. This confirms the findings shown in Zhuo et al.

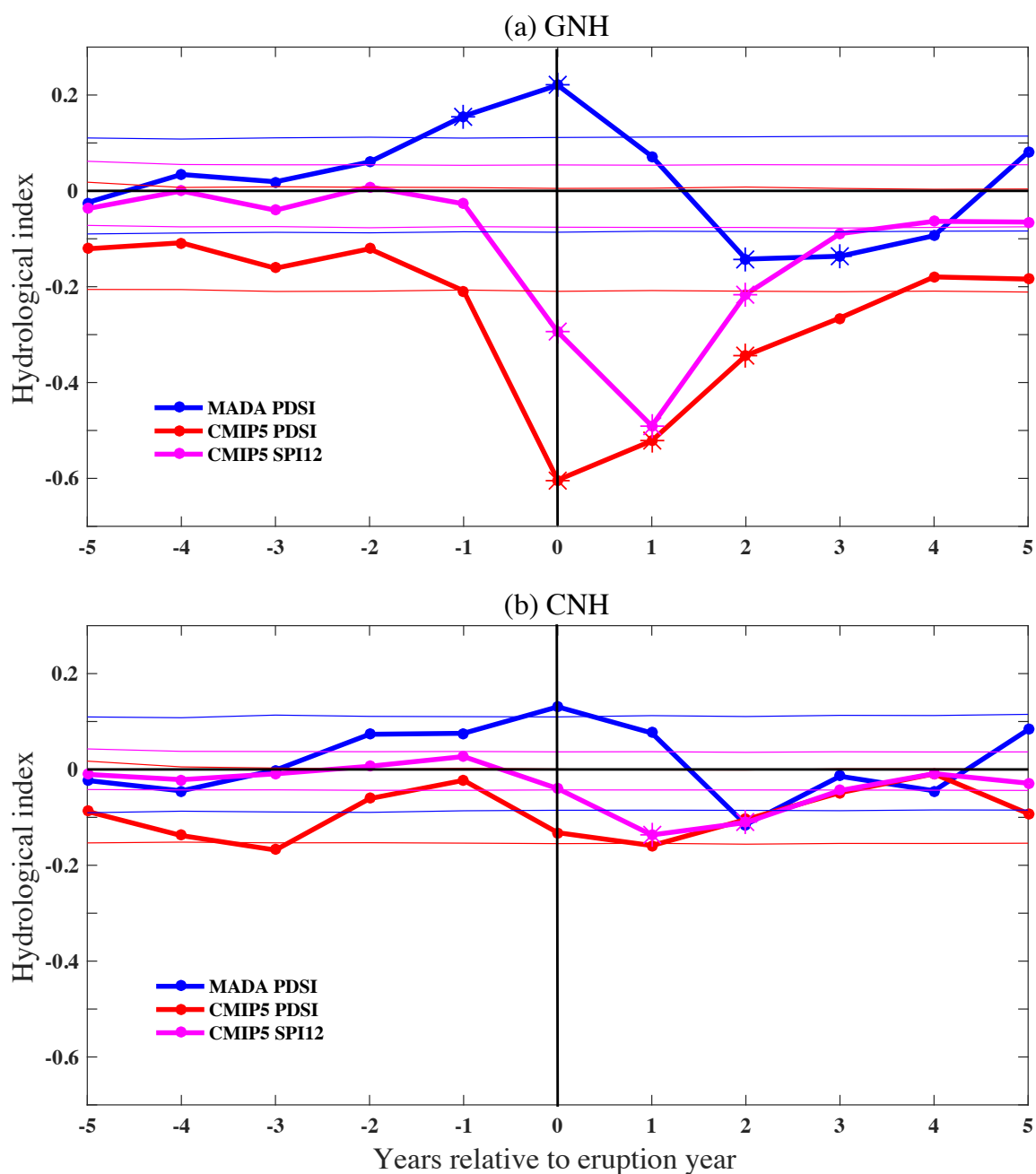


Fig. 3.3 Temporal SEA results of MADA PDSI (blue lines), JJA mean CMIP5 PDSI (red lines) and CMIP5 SPI12 (pink lines) corresponding to GNH (a) and CNH (b) volcanic classifications in 1300-1850 CE in the Asian monsoon region. The thinner lines stand for the relative Monte Carlo model results at the 95% confidence level. The asterisks represent the year that passed the Monte Carlo model tests at the 99% confidence level. Year 0 represents the identified eruption year by volcanic forcing indices, negative and positive years represent relative years before and after the eruption.

(2014) that a larger drying effect in the Asian monsoon region occurs with larger volcanic aerosol magnitude, and it shows similar tendencies among the different cases.

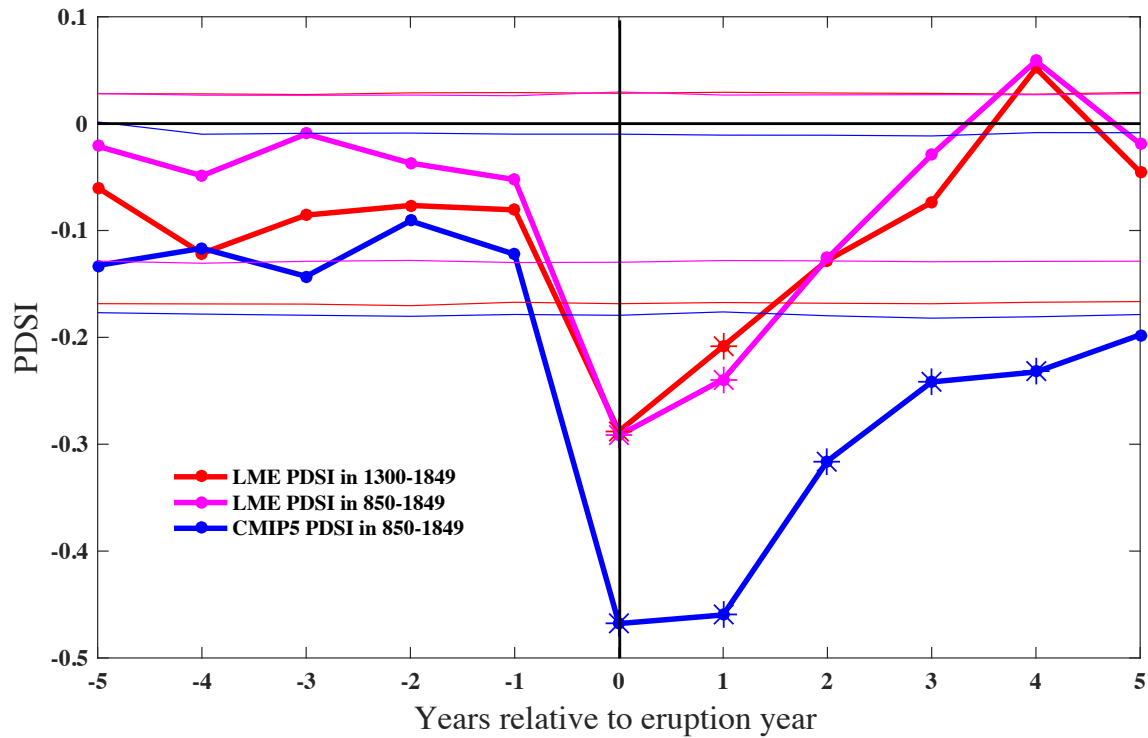


Fig. 3.4 Temporal SEA results of the modeled JJA mean PDSI corresponding to GNH volcanic classification in the Asian monsoon region. Analyses were performed on LME PDSI over the core period (1300-1849), and both LME PDSI and CMIP5 PDSI over the whole period (850-1849). The thinner lines stand for the relative Monte Carlo model results at the 95% confidence level. The asterisks represent the year that passed the Monte Carlo model tests at the 99% confidence level. Year 0 represents the identified eruption year by volcanic forcing indices, negative and positive years represent relative years before and after the eruption.

3.3.2 Temporal response in westerlies and monsoon-dominated subregions

Temporal analysis over the whole region confound the different climate conditions in the westerlies and monsoon-dominated subregions. Additionally, temporal analyses over both the westerlies and monsoon-dominated subregions were performed. Figure 3.5 (a) shows different hydrological responses in the westerlies-dominated subregion, as MADA PDSI in both the GNH (solid blue line) and CNH (dotted blue line) classifications increased from

the negative in year -3 to the positive in year -2. The wet condition extended to in year 0 to year 2, then turned to dry conditions in year 3 to year 5. MADA PDSI in year 1 and year 2 in the CNH classification pass the significance test, but only at the 95% confidence level, and the values are not exceeding the largest value in year -5 and the smallest value in year 5. This indicates that the hydrological response to the volcanic perturbation in the westerlies-dominated subregion is insensitive to volcanic forcing. However, CMIP5 PDSI and CMIP5 SPI12 in the GNH classification show highly significant drying effects in year 0 to year 3 at the 99% confidence level. In the CNH classification, CMIP5 SPI12 shows significant drying effects in year 1 and year 2, but CMIP5 PDSI does not indicate drying effect, instead only significant wetting variation are shown in year -1. This indicates a large difference between MADA PDSI and CMIP5 PDSI/SPI12 in the westerlies-dominated subregion. Considering the exaggerated volcanic forcing in the GNH classification, this also suggests that the wetting or drying effect in this insensitive area depends largely on the magnitude of the injected volcanic aerosols. In the monsoon-dominated subregion (figure 3.5 (b)), MADA PDSI and CMIP5 PDSI/SPI12 in two classifications all agreed on the drying effects in year 0 and year 1 after the volcanic aerosol injection, and the recovering from year 2 onwards. We note that the time-lag effect of proxy data probably exists. As MADA PDSI decreased in year 0, but the significant drying effects are shown in year 1, whereas, CMIP5 PDSI/SPI12 show a sharp decrease in year 0 and the significant drying effects extended to year 1.

Figure 3.6 shows the temporal analyses of LME PDSI over both periods and CMIP5 PDSI over the whole period separately over the westerlies and monsoon-dominated subregions. In the westerlies-dominated subregion, CMIP5 PDSI also indicate a significant drying effect after the aerosol injection over the whole period (850-1849). With the GRA volcanic forcing, LME PDSI increased over both periods in year 1, and then decreased from year 2 to year 5. This is similar to the response tendency of MADA PDSI in GNH classification (figure 3.5 (a)), but both results did not pass the significance tests even at the 95% confidence level. In the monsoon-dominated subregion, model results all suggest consistent drying effects in the eruption year and year 1, and then gradually recovered in year 2.

3.4 Spatial comparison between proxy and model on hydrological effects of volcanic eruptions

Considering the uncertainty of the spatial response arising from the estimated aerosol magnitude in volcanic forcing reconstructions, following discussions are concentrated on horizontal

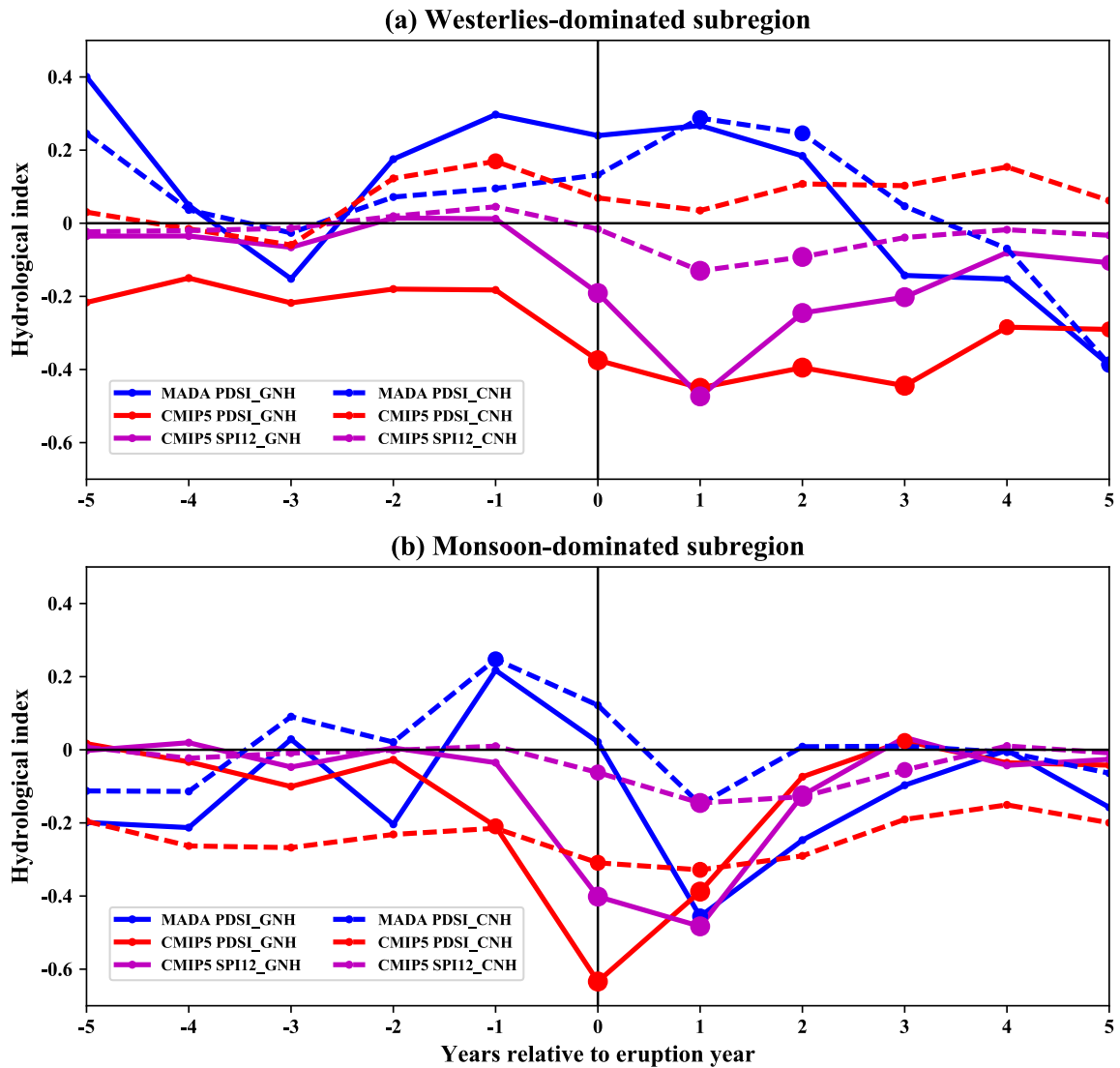


Fig. 3.5 Temporal SEA results of MADA PDSI (blue lines), JJA mean CMIP5 PDSI (red lines) and CMIP5 SPI12 (pink lines) corresponding to GNH (solid lines) and CNH (dashed lines) volcanic classifications in 1300-1850 CE in Asian westerlies-dominated subregion (a) and monsoon-dominated subregion (b). Small and large circle dots indicate the years are significant at the 95% and 99% confidence level.

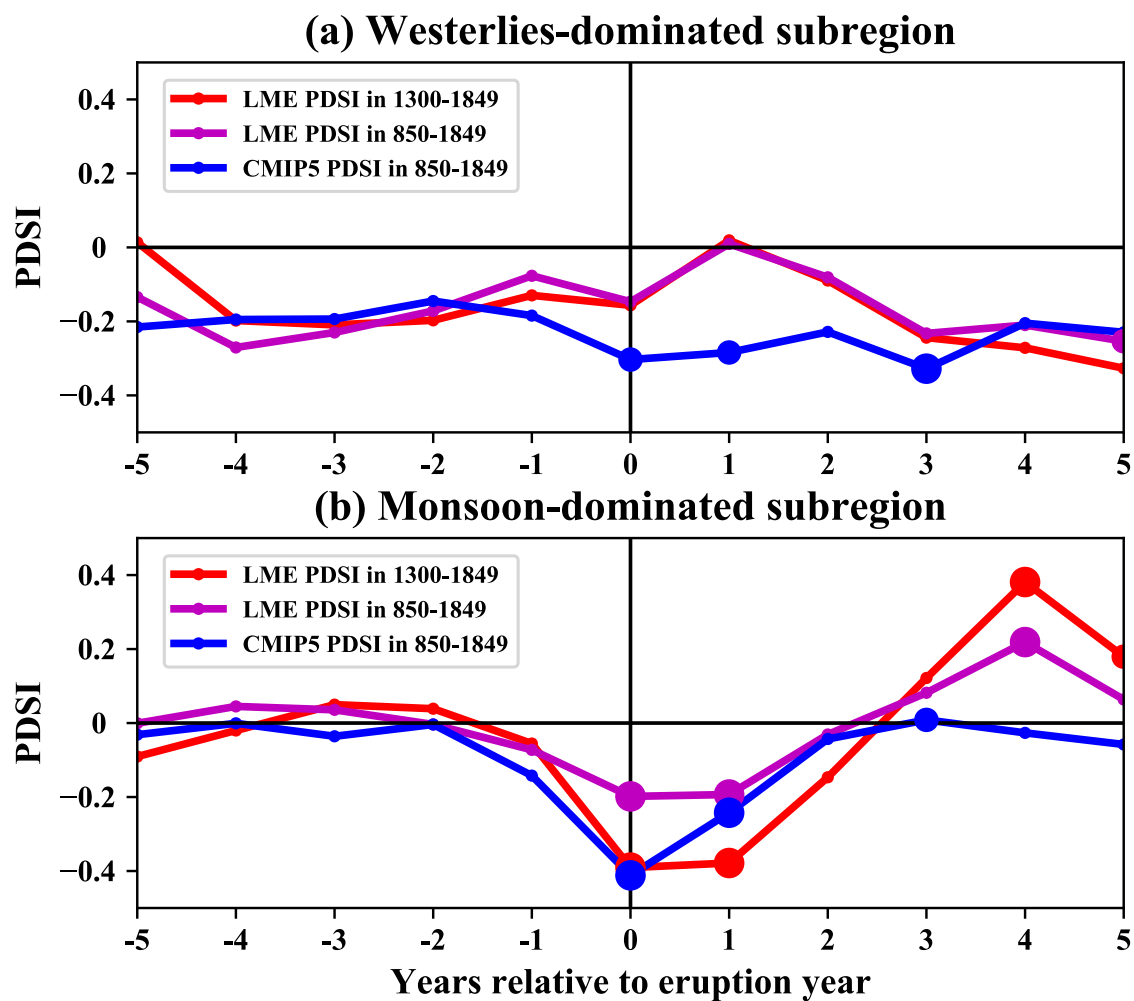


Fig. 3.6 Temporal SEA results of modeled JJA mean PDSI corresponding to GNH volcanic classification in Asian westerlies-dominated subregion (a) and monsoon-dominated subregion (b). Analyses are performed on LME PDSI over the core period (1300-1849), and both LME PDSI and CMIP5 PDSI over the whole period (850-1849). Small and large circle dots indicate the years are significant at the 95% and 99% confidence level.

Table 3.2 Percentage of grid cells that have same sign between MADA PDSI and CMIP5 PDSI/SPI12 in each subregion

Region	Index	GNH				CNH			
		Year 0		Year1		Year 0		Year1	
		PDSI	SPI12	PDSI	SPI12	PDSI	SPI12	PDSI	SPI12
NA	MADA	16%	22%	27%	27%	52%	56%	16%	11%
CA	MADA	31%	38%	17%	9%	57%	50%	41%	17%
w-SA	MADA	32%	28%	40%	44%	48%	48%	52%	60%
w-EA	MADA	56%	58%	59%	65%	56%	62%	57%	62%
SASM	MADA	45%	45%	62%	69%	29%	25%	65%	60%
EASM	MADA	48%	42%	43%	62%	47%	41%	47%	61%
SeA	MADA	17%	14%	43%	46%	40%	24%	31%	29%

Note: Percentage in bold and bold-italics are the first and second largest one in the seven subregions.

distribution of the drying and wetting tendencies. To quantify the similarity of drought and wet areas between proxy and model, the percentage of grid cells that have same sign between MADA PDSI and CMIP5 PDSI/SPI12 in each subregion are shown in table 3.2. Different percentages, from 11% to 69%, indicate that the similarities between MADA PDSI and CMIP5 PDSI/SPI12 differ in different subregions. Eight percentages suggest the largest similarity between MADA PDSI and CMIP5 PDSI/SPI12 in w-EA, followed by SASM and EASM. One finds that the proxy and the model agree better in the subregions with more available tree-ring chronologies, which indicates an important role the original tree ring sources might play on the reliability of proxy reconstruction data. The percentages are generally larger in year 1 than in year 0, except for NA and CA, where one finds the smallest number of tree-ring chronologies. A better similarity between MADA PDSI and CMIP5 PDSI/SPI12 are shown in the monsoon-dominated subregions than in the westerlies-dominated subregions, especially in year 1. This is consistent with the temporal analysis, and spatially quantify that the proxy and the model agree better in monsoon-dominated subregions in year 1.

To investigate the spatial distribution of the drying and the wetting variation, we show the spatial patterns of the superposed hydrological responses to GNH classification in figure 3.7. CMIP5 PDSI shows drier conditions before the eruption than that in MADA PDSI (shown in figure 3.7 (b) as Year -5 to -1 ave), but with a similar southeast-wet-northwest-dry dipolar distribution. MADA PDSI shows wet conditions in NA, northeast EASM and SeA in year 0 and in CA in year 1. However, most of the areas did not pass the significance test. Significant drying effects develop gradually in w-EA in year 0 and extends to SASM and

northern EASM in year 1; the drying effects are reflected by the disappearance of the wet areas in SeA. Consistent with the temporal analysis result, MADA PDSI shows the strongest effect in year 1, with a drying effect in monsoon-dominated subregion and a wetting effect in westerlies-dominated subregion. This gradually reversed in year 2 and turned to wet in the monsoon-dominated subregion while drought in the westerlies-dominated subregion in year 3. Comparing to MADA PDSI, CMIP5 PDSI shows faster and longer effects, with overall significant (99% confidence level) drying effect in year 0 to year 2, except for the wet areas in w-SA and southern EASM. Similarly, drought areas in the monsoon-dominated subregions turned to wet in year 3, while the hydrological effect emerges in the westerlies-dominated subregions (figure 3.7 (b)). These patterns are well verified by CMIP5 SPI12, which displays a weaker response but similar patterns in figure 3.7 (c). From the hydrological variation tendencies, the proxy and the model show similar drying to wetting variation in monsoon-dominated subregions (EASM, SASM and SeA), with faster and longer effects by the model, which were probably caused by the excessive volcanic forcing used in the GISS-E2-R model ensemble members. The ecological time lag-effect of the tree-ring based proxy reconstruction data (Wu et al., 2015) might also contribute to the difference. General agreements are shown in w-EA, where has a dense tree ring coverage. In the westerlies-dominated subregions with rare tree ring availability, MADA PDSI shows a wetting to drying transition, whereas, CMIP5 PDSI and CMIP5 SPI12 show continuous drying effects in CA and NA, but wetting effects in w-SA. This is consistent with the temporal results shown in figure 3.5, that MADA PDSI and CMIP5 PDSI/SPI12 agree on the tendency of the hydrological response to volcanic perturbation in the monsoon-dominated subregion, while discrepancies exist in the westerlies-dominated subregion.

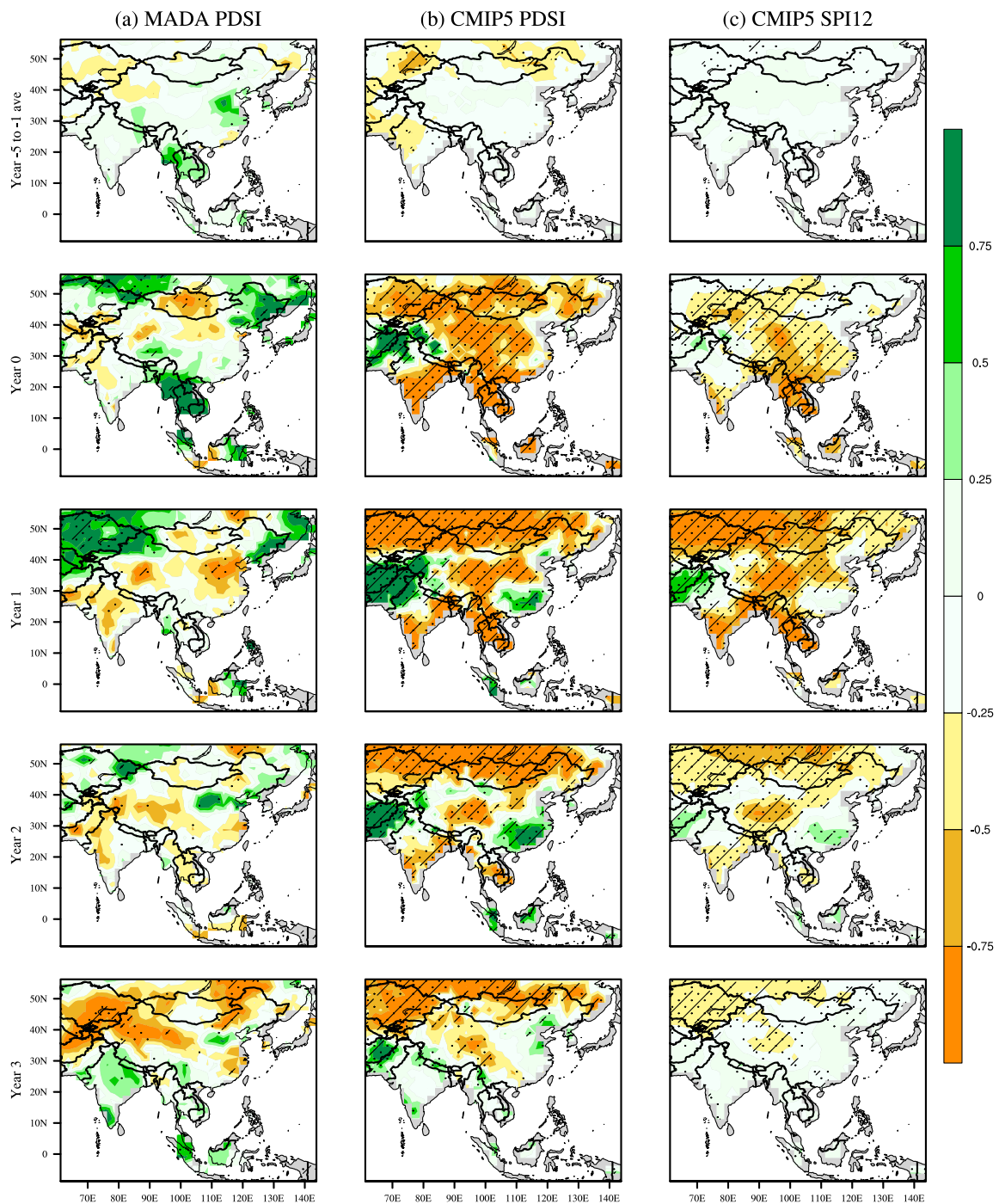


Fig. 3.7 Spatial response of MADA PDSI (a), JJA mean CMIP5 PDSI (b) and CMIP5 SPI12 (c) to GNH volcanic classification in 1300-1850 CE in the Asian monsoon region. The grid cells marked by black dots and slashes denote areas that passed the Monte Carlo model significance tests at the 95% and 99% confidence levels. Year 0 represents the volcanic eruption year by volcanic forcing indices, negative and positive years represent relative years before and after the eruption.

In the CNH classification (figure 3.8), MADA PDSI (figure 3.8 (a)) and CMIP5 PDSI (figure 3.8 (b)) indicates weaker effects of volcanic perturbations, but with similar hydrological patterns as that in GNH classification (figure 3.7 (a) and 3.7 (b)), except that CMIP5 PDSI shows limited response in CA and NA subregions (figure 3.8 (b)). This indicates that the large drying effects shown in GNH classification (figure 3.7 (b)) are caused by the response to the exaggerated volcanic forcing in GISS-E2-R model ensemble members. CMIP5 SPI12 (figure 3.8 (c)) indicates even weaker effects, but the obvious drying areas agree well with other CMIP5 PDSI patterns. Better agreement between MADA PDSI and CMIP5 PDSI/SPI12 occurs in the subregions with more tree ring sources, and highly significant results of CMIP5 PDSI/SPI12 in GNH and CNH classifications indicates the consistency of models on reproducing the drying and wetting response to volcanic perturbations. In westerlies-dominated subregions, discrepancies between MADA PDSI and CMIP5 PDSI/SPI12 do not allow drawing definite conclusions.

To further explore the reliability of model simulations, we add spatial analysis on LME PDSI over both periods (1300-1849 and 850-1849) and CMIP5 PDSI over the whole period (850-1849). Since similar patterns between CMIP5 PDSI and CMIP5 SPI12 were found, only PDSI is used as the indicator of the hydrological conditions. As seen from figure 3.9, CMIP5 PDSI shows similar patterns; even extending the period to the whole 1000 years. Similar patterns are also shown in LME PDSI over both periods. The spatial patterns are not exactly the same among these different groups of ensemble member means, and the calculated pattern correlations are not significant (not shown). However, with different resolution of the models, it is too hard to have complete matches. This indicates that the study periods, the number of the superposed events and the aerosol magnitude do not have large effect on the spatial patterns of the hydrological effect. These similar patterns support the reliability of models on reproducing the hydrological effects of volcanic eruptions in southern Asian monsoon region.

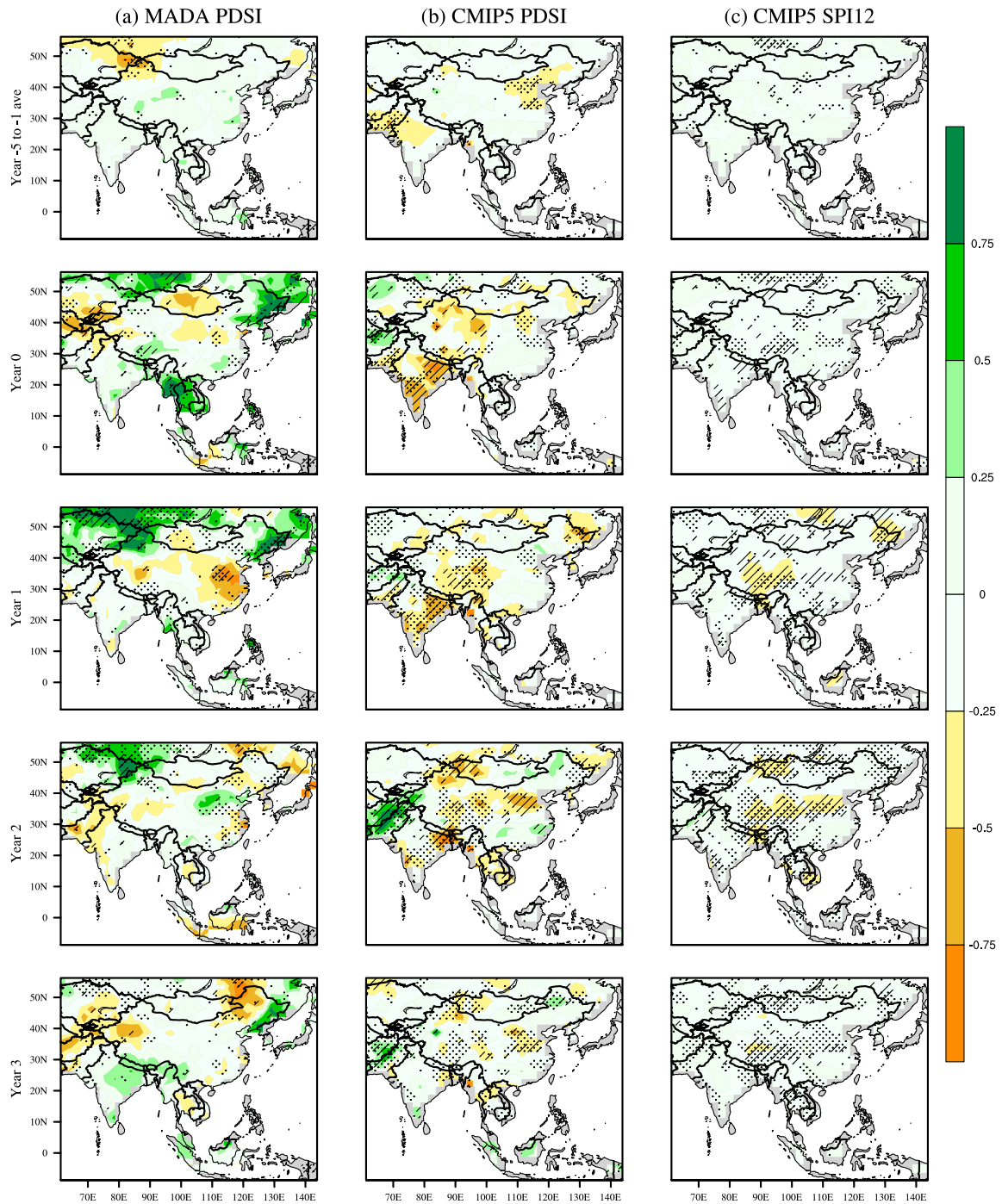


Fig. 3.8 Spatial response of MADA PDSI (a), JJA mean CMIP5 PDSI (b) and CMIP5 SPI12 (c) to CNH volcanic classification in 1300-1850 CE in the Asian monsoon region. The grid cells marked by black dots and slashes denote areas that pass the Monte Carlo model significance tests at the 95% and 99% confidence levels. Year 0 represents the volcanic eruption year by volcanic forcing indices, negative and positive years represent relative years before and after the eruption.

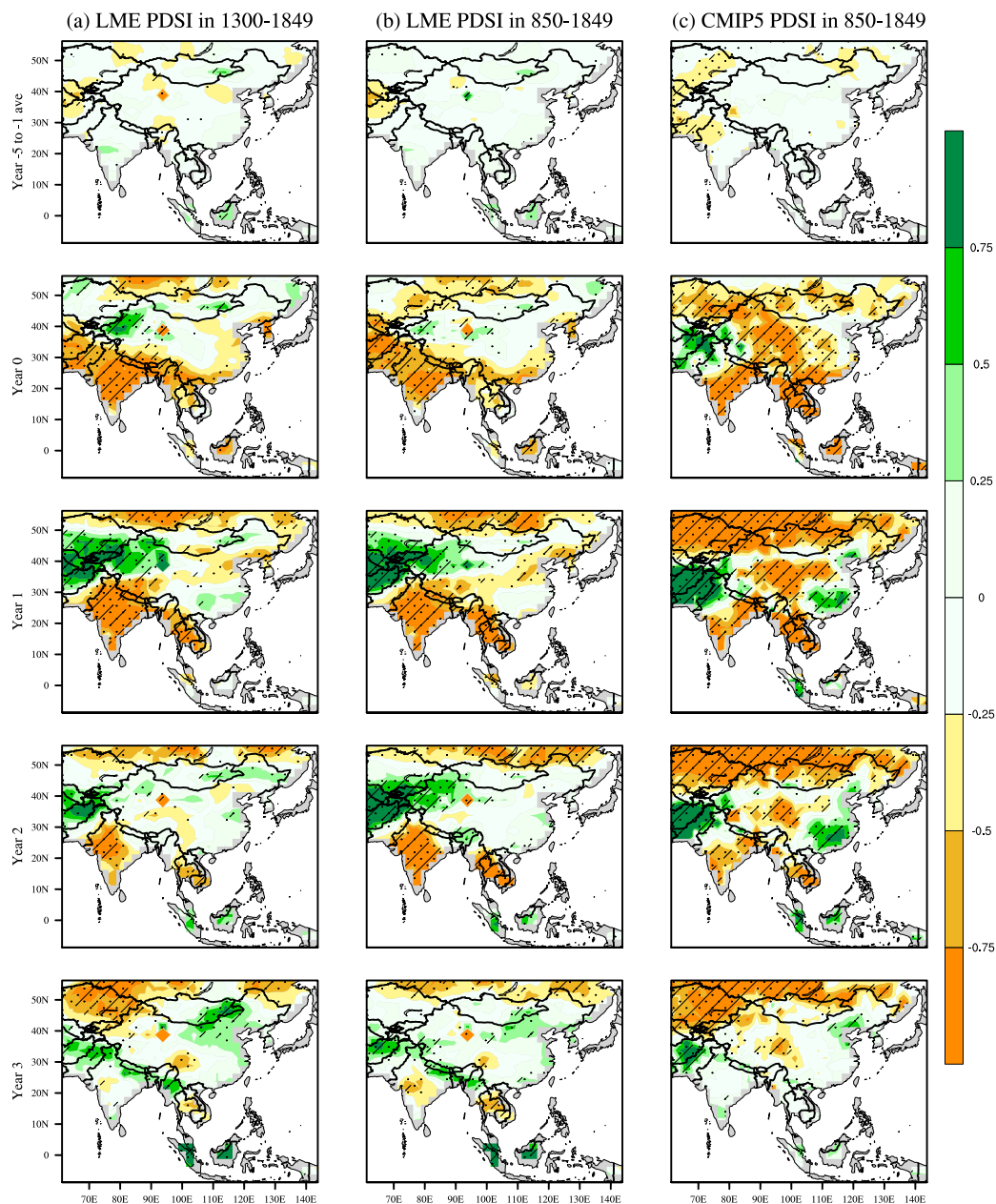


Fig. 3.9 Spatial response of modeled JJA mean PDSI to GNH classification in the Asian monsoon region. Analyses were performed on LME PDSI over the core period (1300-1849), and both LME PDSI and CMIP5 PDSI over the whole period (850-1849). The grid cells marked by black dots and slashes denote areas that passed the Monte Carlo model significance tests at the 95% and 99% confidence levels. Year 0 represents the volcanic eruption year by volcanic forcing indices, negative and positive years represent relative years before and after the eruption.

Summarizing the proxy-model comparison on the spatio-temporal hydrological response patterns to volcanic eruptions, one finds a similar drying effect in the monsoon-dominated subregion while discrepancies exist in the westerlies-dominated subregion. A better agreement on the spatial patterns is found in w-EA, SASM and EASM where there are more available tree rings. This poses an advance on previous studies. Anchukaitis et al. (2010) showed an east-dry-west-wet dipolar pattern by single model CSM1.4. Zhang et al. (2012) showed wetting effects in central Asia by ensemble mean of single model MPI-COSMOS. However, MADA PDSI shows different spatial pattern (Anchukaitis et al., 2010; Stevenson et al., 2017, 2016; Zhang et al., 2012) also showed different patterns between MADA PDSI and ensemble mean of single model CESM. These spatial comparisons were made only in the eruption year. In comparison, our results were based on MMEMs and showed significant improvements. Spatial comparisons of three years were made and suggested a better agreement in one year after the eruption. CMIP5 PDSI and CMIP5 SPI12 verify each other between two classifications with highly significant results. Similar spatial patterns by LEM PDSI indicates the reliability of model simulations. They agree better in the monsoon-dominated subregions with MADA PDSI responding to different volcanic eruption lists. In the southern Asian monsoon region, spatial patterns of MMEMs in year 0 and year 1 agree well with precipitation anomaly pattern after Krakatau and Pinatubo eruptions by CMIP5 model mean in historical simulations (Zambri and Robock, 2016). The identified wet areas in EASM are close to that in Gao and Gao (2018), which showed an increased precipitation over the Yangtze-Huaihe River valley using Feng et al. (2013) precipitation reconstruction. The patterns are also consistent with the observed precipitation and PDSI variations shown in Trenberth and Dai (2007), with a drying effect in SASM, SeA and northern EASM, and wetting effect in w-SA and southern EASM after the Mount Pinatubo eruption. In the northern Asian monsoon region, except for PDSI, which suggest drying effects (Trenberth and Dai, 2007), limited effects are shown in precipitation (Trenberth and Dai, 2007; Zambri and Robock, 2016) and runoff variations (Trenberth and Dai, 2007). The reliability of MMEMs is reflected in the patterns of hydrological response to volcanic perturbation in the Asian monsoon region, except for Central Asia and North Asia; one cannot draw definite conclusions in these two subregions, because CMIP5 PDSI and CMIP5 SPI12 in CNH classification display no impact, and there are only few observations in these subregions.

3.5 Discussion on uncertainty source of proxy and model

Results suggest large discrepancy between MADA PDSI and the models in the westerlies-dominated subregions with fewer available tree rings, and a better agreement is shown in

one year after the eruption instead of in the eruption year. These discrepancies indicate the uncertainty of the results deriving from the data source and analysis process. As suggested by Consortium (2017), we treated the proxy reconstruction and the model data equally, and discussed the uncertainties and limitations of both MADA PDSI and CMIP5 PDSI/SPI12. From the temporal analysis of the Asian monsoon region (figure 3.3), we can see that CMIP5 PDSI/SPI12 agrees with MADA PDSI on the drying effects of explosive volcanic eruptions. CMIP5 PDSI shows stronger effects than MADA PDSI in GNH classification. Stronger effects are also shown in the GNH classification than that in the CNH classification. This is caused by both the exaggerated volcanic forcing used in the GISS-E2-R model ensemble members and the reduced amplitude of the forcing in the CEA reconstruction (Crowley and Unterman, 2013; Crowley et al., 2008). Besides, faster responses are shown in CMIP5 PDSI/SPI12 than that in MADA PDSI in both classifications. This reflects the time lag effect in the tree-ring based ecological response compared to the meteorological response in the model simulation (Wu et al., 2015).

Volcanic event years identified in volcanic forcing indices deviate from the reality. Superposed volcanic classification averages out the effect of a single event, but the dating uncertainty of volcanic events can cause large uncertainty in the hydrological effect reflected by MADA PDSI. Uncertainties in the eruption month of the volcanic events in the indices also bring uncertainty of defining the eruption year. To investigate the dating uncertainty of volcanic events, we tested several different classifications. Table 3.1 shows a different number of events and the dates of the volcanic events in different classifications. We show the response of MADA PDSI to these different classifications in figure 3.10. From it, we can see that in GCNH classification, MADA PDSI suggests a wetting effect in year 0, in other classifications, MADA PDSI started to decrease in year 0, and dropped to the lowest value in year 2 and year 3 in SNH and A07 classifications, respectively. SNH classification is based on the most start-of-the-art volcanic reconstruction, which largely improved the dating accuracy (Sigl et al., 2015), while A07 classification includes only those five explosive eruptions that are the most well-known events during the past centuries. These two classifications have minimum dating uncertainty among the volcanic classifications used in this thesis. Thus, the wetting effect shown in MADA PDSI is probably the result of the dating uncertainty of the volcanic events.

The temporal analysis results of two separated subregions (figure 3.5) suggest an agreement between MADA PDSI and CMIP5 PDSI/SPI12 in the monsoon-dominated subregion while large discrepancies are shown in the westerlies-dominated subregion. Quantification of the grid cells with same sign between MADA PDSI and CMIP5 PDSI/SPI12 indicates a better agreement in subregions with more tree ring sources and in the second summer after

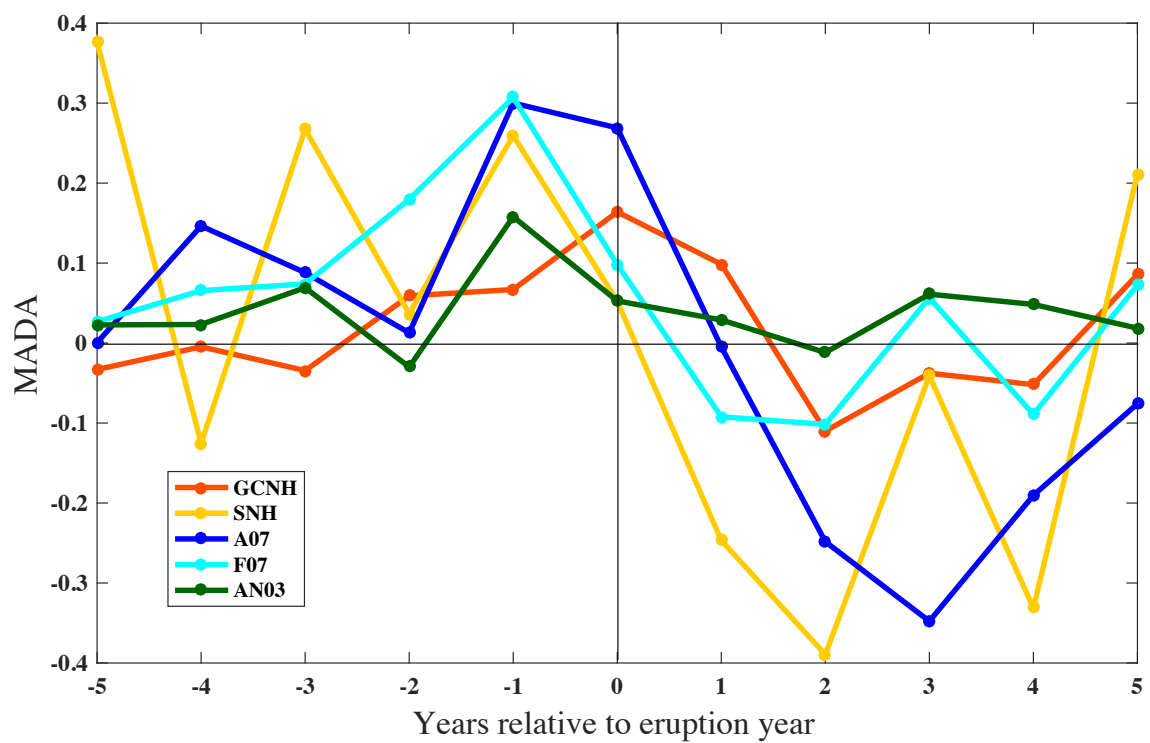


Fig. 3.10 Temporal analysis results of MADA PDSI corresponding to different volcanic classifications.

the volcanic perturbation. This might explain partly the spatial proxy-model discrepancies suggested by previous studies (Anchukaitis et al., 2010; Stevenson et al., 2017, 2016; Zhang et al., 2012), because comparisons were only made in the first summer after the eruption. Comparison on spatial patterns of the hydrological effects show large discrepancies in the westerlies-dominated subregions with limited tree ring sources. This also reveals the limitation of MADA PDSI caused by the spatial coverage of original tree rings. The drying tendencies in the westerlies-dominated subregion reflected by CMIP5 PDSI/SPI12 in GNH classification might be realistic, but it might be misleading patterns coming from the exaggerated volcanic forcing used in the GISS-E2-R model ensemble members. This exaggerated forcing also contributes to the faster and longer drying effects of volcanic perturbation in monsoon-dominated subregions.

Spatial analysis (figure 3.7) indicates significant wetting effects in MADA PDSI in North Asia (NA), which is opposite to the drying effects shown by CMIP5 PDSI and LME PDSI in the GNH classification. This discrepancy was also seen in Liu et al. (2016) between MADA and another precipitation reconstruction. Thus, the wetting effect also indicates the data uncertainty of MADA PDSI, especially in the westerlies-dominated subregion where there is a shortness of tree-ring chronologies, especially those go back to 1300 CE (Cook et al., 2010). However, we would like to point out that the models also suggest a wetting effect in the western areas, and the wetting areas vary a bit in the different groups of ensemble member means, which have different forcing magnitudes. Thus, the discrepancy can also be caused by the uncertain aerosol magnitude and the consequent uncertain effect shown in the models. The difference in resolution of both proxy reconstruction and models also introduces uncertainties.

A limited number of ensemble members might bring uncertainty to MME-based analysis. Especially, three ensemble members of GISS-E2-R model might have a dominant effect on the MEM. However, when testing MEMs with only four members (members in black in figure 3.1), which include only one member of GISS-E2-R, temporal and spatial patterns remain largely unchanged. This illustrates the limited effect of the number of ensemble members on the hydrological response patterns. Deviation of the model-based analysis between two classifications can come from the number of classified events based on volcanic forcing indices. However, when testing the classifications with the same nine events in both indices (marked in red in figure 3.1), temporal and spatial patterns remain largely constant. This indicates the negligible effect the number of events brings on the patterns.

The internal variability of the climate system often brings uncertainty on detecting the hydrological effects of volcanic eruptions, especially the hardly constrained effects of the concurrent ENSO events (Adams et al., 2003; Khodri et al., 2017; Li et al., 2013; Stevenson

et al., 2017, 2016). The effect of eruption seasons on the circulation and ENSO can bring extra uncertainties (Stevenson et al., 2017). All these might contribute to the proxy-model discrepancies, especially in the initial phase and the phase-out period of the hydrological effects. Following the method in Iles et al. (2013), we tested this uncertainty through repeating the SEA analysis after regressing out the effect of ENSO. Consistent with Iles et al. (2013) and Iles and Hegerl (2014), it only resulted in a lower response in amplitude, but the temporal and spatial patterns remain largely unchanged. In addition, previous researches show that volcanic eruptions can affect the hydrological condition through affecting the evolution of ENSO in time, but with large contradictory findings (Adams et al., 2003; Li et al., 2013; Liu et al., 2018; Stevenson et al., 2016; Sun et al., 2018; Wang et al., 2017). This is an additional source contributing to proxy-model discrepancies. Future improvement of volcanic forcing reconstructions, model simulations, proxy reconstructions and observations will lead to a better understanding and reconciling the proxy-model discrepancies.

Chapter 4

The Mechanism of volcanic aerosol's hydrological effect in the Asian monsoon region

Summarizing the previous chapter, CMIP5 multi-model ensemble means (MMEMs) are able to reflect the drying effect of the northern hemisphere volcanic aerosol injection in the monsoon-dominated subregion while wetting effects are shown in western-South Asia. The mechanism of the inversed hydrological response to volcanic eruptions in the different subregions of the Asian monsoon region is not yet been clarified. This chapter is aimed at answering the main questions 4 and 5 raised in the introduction chapter. The CMIP5 MMEM is used to explore the potential mechanism of different hydrological effects of volcanic eruptions in different subregions of monsoon Asia. Endeavors are also made to examine the hydrological effects of different hemispheric volcanic aerosol injections in the Asian monsoon region.

4.1 Volcanic classifications with different hemispheric aerosol loadings

To explore the hydrological effects of volcanic eruptions in different hemispheres, volcanic classifications with aerosol loadings in different hemispheres were constructed. Chapter 3 indicates the capability of MMEM on reproducing the volcanic eruptions' hydrological effects in the southern Asian monsoon region. The two classifications based on GRA (Gao et al., 2008) and CEA (Crowley et al., 2008) volcanic forcing reconstructions show similar patterns, with more significant and pronounced patterns from the group of GRA-based

output. Thus, in this chapter, analyses were performed with the GRA-based MEM of PMIP3/CMIP5 to explore the mechanism of the hydrological effect. For the explosive volcanic aerosol injection in the NH, we used the same GNH classification as that in chapter 3. Volcanic eruptions included in this classification injected larger aerosol magnitude into the NH than that of the 1991 Pinatubo eruption. To explore the hydrological effects of the different hemispheric volcanic aerosol injection, another classification, based on the GRA volcanic forcing index, with volcanic events in 1300-1850 that only injected aerosols into southern hemisphere, was constructed, and named GSH classification. Figure 4.1 shows the volcanic years and aerosol magnitudes in two classifications. Comparing to the GNH classification, the aerosol magnitudes of volcanic eruptions in the GSH classification are much smaller. This might result in a reduced climate effect in the GSH classification, and might not be sufficient to indicate the different hydrological effects of different hemispheric volcanic aerosols. However, since both classifications have 12 volcanic events, the GSH classification is sufficient to serve as a reference classification without northern hemisphere volcanic aerosol injection.

4.2 Climate response to GNH and GSH classifications

To show the climate effects of the classified volcanic eruptions, temporal and spatial SEA analyses are performed on PDSI and temperature. Figure 4.2 shows the hydrological response to two volcanic classifications in the Asian monsoon region. From figure 4.2 (a), we can see that in response to the GNH volcanic classification, PDSI indicates significant drying effect in the eruption year (year 0). This drying effect extends to three years after the eruption (year 3). For the GSH classification, PDSI change shows no clear sign, but positive PDSI was shown in year 2 and passed the 99% confidence level, which might indicate wetting effects. The limited effects might be caused by the limited aerosol magnitudes injected into SH based on the GRA volcanic reconstruction. However, results in the GSH classification evidently indicate a large difference between with and without NHVAI. The variation of precipitation indicates similar response. The largest decrease of precipitation emerged in year 0. The drying effect extended to year 1 and then recovered in year 2.

Figure 4.3 indicates the temperature response in two volcanic classifications. From figure 4.3 (a) shows that similar to PDSI variation, in the GNH classification, the largest decrease of land average temperature (T , reference to average of the whole period) of the Asian monsoon region emerged in year 0 and this significant cooling effect extended to year 2 after the northern hemispheric aerosol injection. For the GSH classification, insignificant decreases are shown in year 0 to year 2. Figure 4.3 (b) shows the temperature difference between the

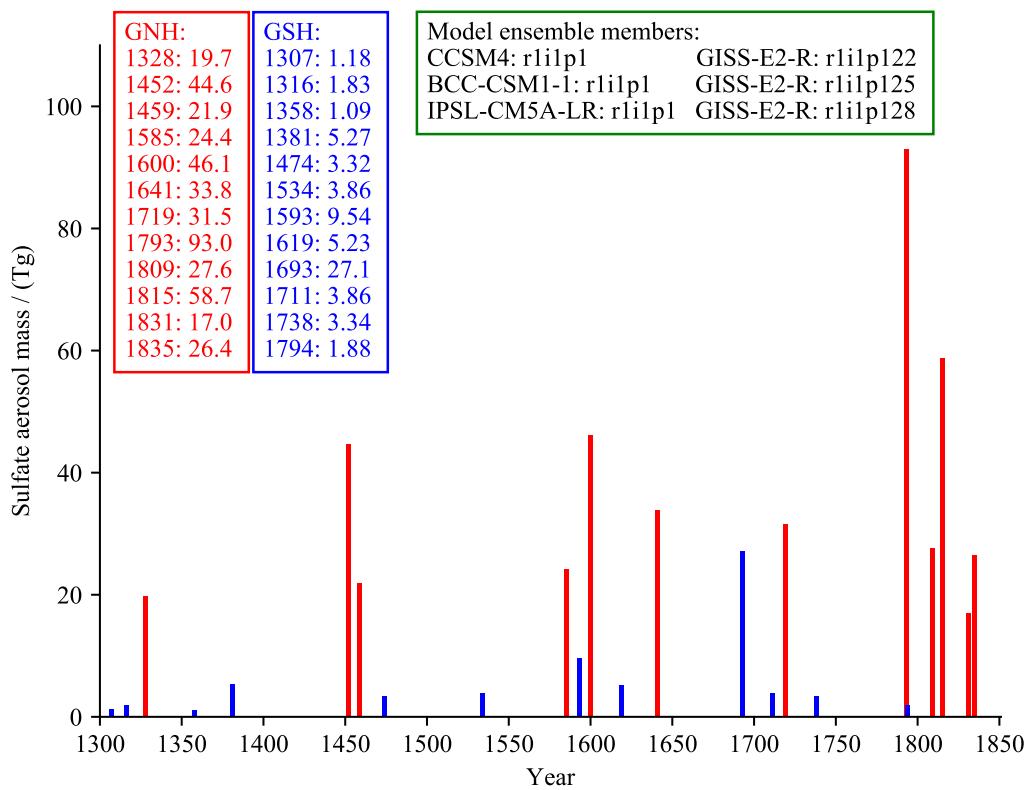


Fig. 4.1 Volcanic years and the hemispheric volcanic aerosol injection magnitudes (Tg) in GNH (red lines and texts) and GSH (blue lines and texts) classifications. Model ensemble members used in this chapter are shown in the green box.

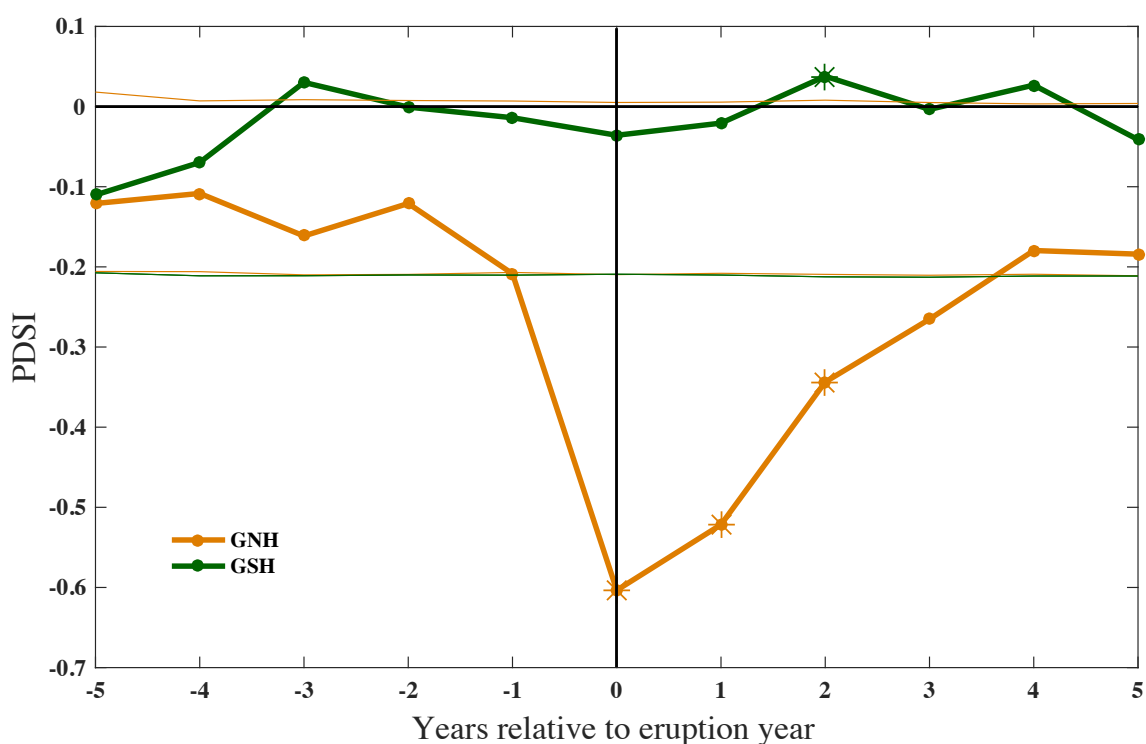


Fig. 4.2 Temporal SEA results of summer JJA mean PDSI corresponding to GNH (yellow line) and GSH (green line) volcanic classifications in 1300-1850 CE in the Asian monsoon region. The thinner lines stand for the relative Monte Carlo model (method see chapter 2.4.3) results at the 95% confidence level. The asterisks represent the years that passed the Monte Carlo model tests at the 99% confidence level. Year 0 represents the identified eruption year by volcanic forcing index, negative and positive years represent relative years before and after the eruption.

land and the sea in the Asian monsoon region. The significant decreasing value in GNH classification confirms a decreased land-ocean thermal contrast caused by the NHVAI; while in the GSH classification, it increased significantly in year 0 and year 1. This indicates an inversed increase of land-ocean thermal contrast after SHVAI. The quantitatively analyzed results in this study confirmed previous findings that volcanic aerosols in the stratosphere reflect more solar radiation back to the space, which leads to an inhomogeneous cooling effect between land and the sea (Robock, 2015). The opposite response to GNH and GSH classifications quantitatively shows the different effect of interhemispherically asymmetric VAI, which was also reported in African monsoon region (Haywood et al., 2013) and global monsoon domain (Liu et al., 2016; Zuo et al., 2018).

The above temporal analyses indicate that the largest drying effect occurs in the eruption year. To look into the spatial distribution of the hydrological effect and the potential mechanism, the spatial patterns of the anomalies in the eruption year are shown, which were calculated with respect to the average of five years before the eruption (Iles et al., 2013; Zuo et al., 2018). Figure 4.4 shows the spatial patterns of PDSI and temperature anomaly. We can see that in GNH classification (figure 4.4 (a)), PDSI indicates significant drying effect in a large part of the Asian monsoon region. The largest drying effects emerge in the southern part of the region (solid black box), while the largest wetting effects are concentrated in the south-western part of the region (dotted black box). This is exactly opposite to the normal hydrological pattern in the Asian monsoon region, which, as shown in figure 1.1, has the maximum precipitation in its southern part (marked as relatively wettest area, RWA) but the minimum precipitation in its south-western part (marked as relatively driest area, RDA). This strong change has the potential to bring large impacts to the local environment and society. Yet no detailed study toward the cause of the hydrological variation has been made. Thus, in this chapter, we fill in the gaps by exploring the mechanism of this inversed hydrological response to the NHVAI in these two areas. Meanwhile, as shown in figure 4.4 (b), different from that in GNH classification, PDSI shows wetting effects in the RWA in the GSH classification, whereas, it shows slight wetting effect in the RDA. This indicates the inversed hydrological effects of different hemispheric volcanic eruptions in the Asian monsoon region. The lower figure 4.4 shows the spatial distribution of the temperature anomaly, which indicates a strong cooling effect in the RDA, but a slight cooling and warming effects in different parts of the RWA in the GNH classification. In the GSH classification, the largest cooling effect appears in the RWA. When comparing to the spatial pattern of PDSI, we can see that in the GNH classification, the area with the largest wetting effect (in the RDA) coincides with the largest cooling effect; whereas the driest area in the RWA is identical to the area with the smallest warming effect. It also shows a similar matching relationship between

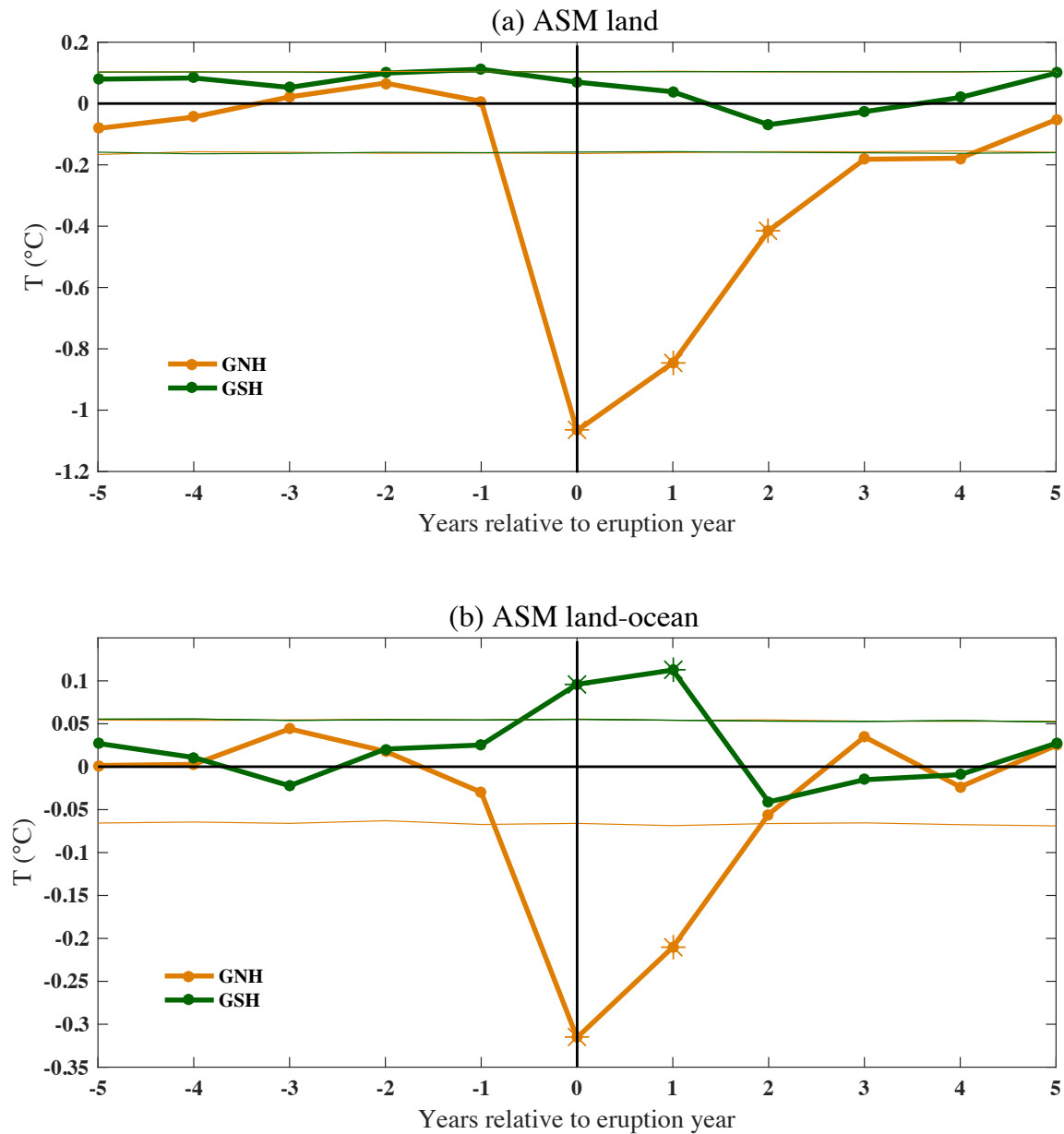


Fig. 4.3 Temporal SEA results of summer JJA mean temperature ($^{\circ}\text{C}$) of land (a) and difference between land and ocean (b) in the Asian monsoon region. The thinner lines stand for the relative Monte Carlo model (method see chapter 2.4.3) results at the 95% confidence level. The asterisks represent the years that passed the Monte Carlo model tests at the 99% confidence level. Year 0 represents the identified eruption year by volcanic forcing index, negative and positive years represent relative years before and after the eruption.

PDSI and temperature in GSH classification, although with wetting effects in the RWA. This indicates that the temperature variation and the hydrological responses to volcanic eruptions are strongly coupled.

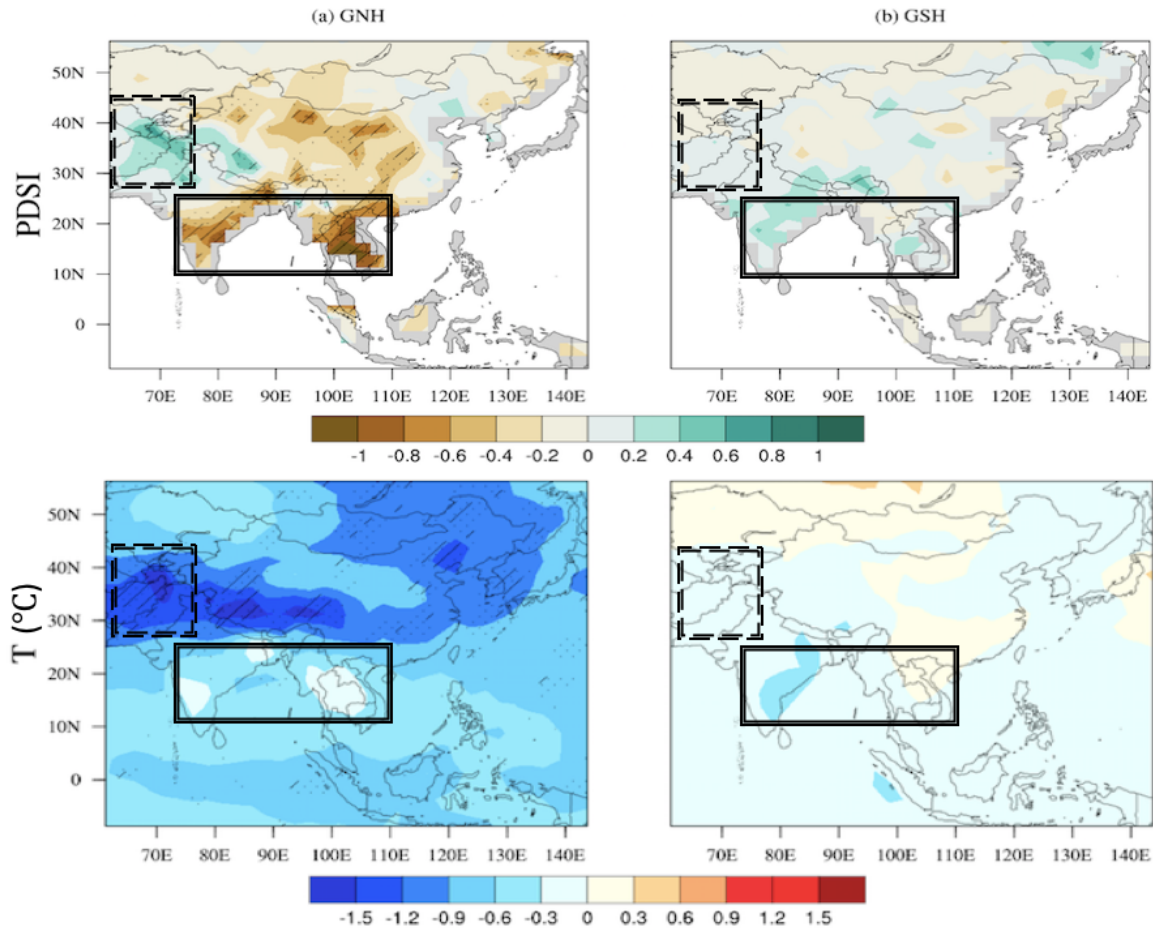


Fig. 4.4 Spatial distribution of the Palmer Drought Severity Index (PDSI, top) and the temperature (T , $^{\circ}\text{C}$, bottom) anomalies in the eruption year with respect to the average of the five years before the eruption. The solid and dashed black box indicates the relatively wettest area (RWA) and relatively driest area (RDA) as shown in figure 1.1, respectively. Regions with black dots and slashes are significantly at the 95% and 99% confidence level.

4.3 Correlation analysis

To identify the key factors that affect the hydrological variation, correlation analyses between radiation, heat, moisture related variables and sea surface temperature (SST) and precipitation (P) were performed, using Pearson cross correlation (r) as the indicator. Since the limited

Table 4.1 Average Pearson cross correlation (r) values between precipitation (P), sea surface temperature (SST) and radiation, heat and moisture related variables of the Asian monsoon region. Numbers in italics are significant at the 95% confidence level. Numbers in bold are significant at the 99% confidence level.

Variables	Abbreviation	P	T
Top of atmosphere incident shortwave radiation	TOA ISR	0.255	<i>0.678</i>
Top of atmosphere outgoing shortwave radiation	TOA OSR	-0.212	-0.788
Top of atmosphere outgoing longwave radiation	TOA OLR	0.121	0.706
Surface upwelling shortwave radiation	USR	-0.142	0.289
Surface downwelling shortwave radiation	DSR	-0.00171	<i>0.667</i>
Surface upwelling longwave radiation	ULR	0.251	0.996
Surface downwelling longwave radiation	DLR	0.459	0.947
Surface upward latent heat flux	LHF	<i>0.613</i>	0.690
Surface upward sensible heat flux	SHF	-0.300	0.321
Evaporation	E	<i>0.613</i>	0.691
Near-surface relative humidity	RH	<i>0.611</i>	0.00499
Near-surface specific humidity	/	<i>0.575</i>	0.881

effects are likely due to smaller aerosol magnitudes in the GSH classification, the correlation analyses were only conducted on the GNH classification.

Table 4.1 shows the average r of the Asian monsoon region between the variables. From the table, we can see that SST is highly correlated with radiation and specific humidity, with r reaching to 0.996/0.947 between SST and upwelling/downwelling longwave radiation (LW), followed by -0.788 and 0.881 between SST and top of the atmosphere (TOA) outgoing shortwave radiation (OSR) and specific humidity. P is more correlated with the evaporation (E)/latent heat flux (LHF, r equal to 0.613) and closely related to relative humidity (RH, r equal to 0.611) and specific humidity (r equal to 0.575). From these correlations, one can conclude that in order to understand the temperature variation, it is important to look into the variation of shortwave and longwave radiation. For the precipitation, the variation of evaporation, latent heat flux and relative humidity are checked. Both, temperature and precipitation, are highly correlated with specific humidity, which indicates that the response of the model follows the Clausius-Clapeyron relation. These correlation analyses can identify the key factors of the hydrological variation but is not sufficient to explain the inversed hydrological responses in the RDA and the RWA (figure 4.4).

4.4 Mechanism of the hydrological response in GNH classification

To explore the potential mechanism of the characteristic response in different areas, the spatial patterns of highly related variables identified by the correlation analyses were investigated. Since limited climate effects are shown in the GSH classification, discussions here are focused on the GNH classification to explore the mechanism chain.

4.4.1 The role of atmospheric clouds and water vapor

The hydrological response is connected with the temperature response. To explore the mechanism of the temperature response, the radiative effects of volcanic aerosols are investigated. As indicated by the clear sky TOA OSR in figure 4.5, the volcanic aerosols reflect large amount of OSR in the GNH classification. The reflected OSR is relatively homogeneous along the same latitude band but decreases from low latitude to high latitude in the northern hemisphere (figure 4.5 (a)). This reflects the direct radiative effect of latitude-dependent volcanic aerosols.

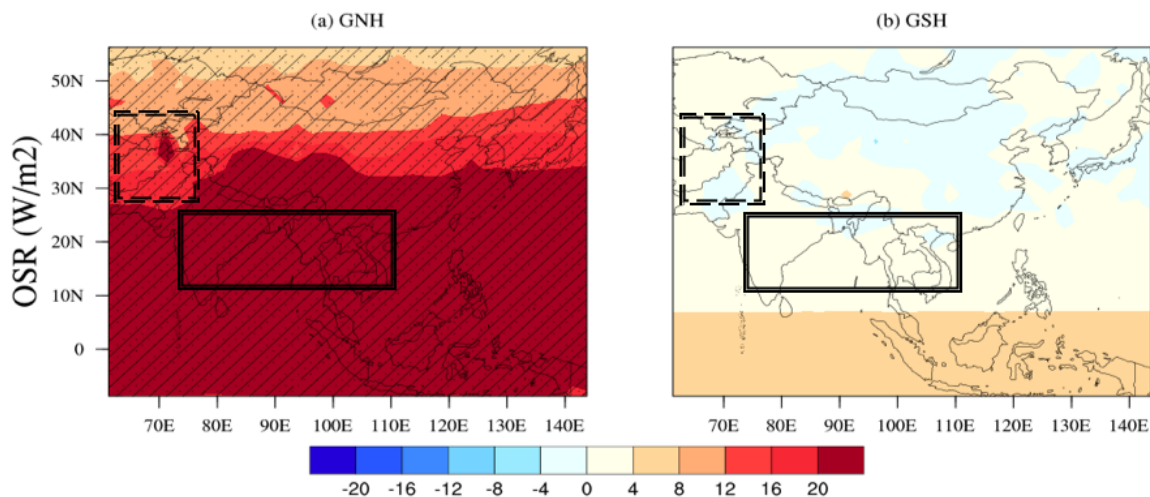


Fig. 4.5 Spatial distribution of top of the atmosphere outgoing shortwave radiation (TOA OSR, W/m^2) anomalies in clear sky in the eruption year with respect to the average of the five years before the eruption. The solid and dashed black box indicate the relatively wettest area (RWA) and the relatively driest area (RDA) as shown in figure 1.1, respectively. Regions with black dots and slashes are significantly at the 95% and 99% confidence level.

The full sky TOA OSR shows inhomogeneous distribution in different regions. As shown in figure 4.6(a), it has a stronger reflection of the solar radiation in the RDA (figure 4.6

(a)), resulting in a larger cooling effect (figure 4.4 (a)). In the RWA, uncertain variations can be found. Slightly increased or decreased reflection of the solar radiation are shown in different parts of the region, which lead to the uncertain variation of T in this area, with slight cooling or warming in different parts of the region (figure 4.4 (a)). Additionally, the cloud area fraction (C, figure 4.6 (a)) indicates a significant increase of clouds in RDA, but decreased significantly in RWA. The difference between clear sky and full sky TOA OSR, and the correlation between full sky TOA OSR and T and C suggests that the regional surface temperature variation is not only due to the direct radiative effect of stratospheric aerosols injected by the explosive volcanic eruptions, but more dominated by the radiative effect of the subsequently formed atmospheric clouds in different regions. The temperature response leads to the variation of the upwelling longwave radiation (ULR) and sensible heat flux (SHF), with a simultaneous reduction of ULR and upward SHF in the RDA. Different variations are shown in different parts of the RWA (not shown).

The temperature variation is related to the hydrological variation. As indicated by the correlation analysis, precipitation is closely related to evaporation (E) and relative humidity (RH). The spatial pattern shows an increase of E in the RDA but a significant decrease of E in the RWA (figure 4.7 (a)). Figure 4.7 (b) indicates a significant increase of RH in the RDA but a significant decrease of RH in the RWA. The model follows the Clausius-Clapeyron relation, which connects these responses with the temperature variation. In the RDA, along with the cooling, the saturation humidity is decreased. The significant increase of the relative humidity result from the increase of the actual water vapor content in the air, which favors the formation of more clouds and precipitation. Whereas, in the RWA, because of the variability of the temperature, the saturation humidity varies. The significant decrease of the relative humidity results from the decrease of the actual water vapor content. This results in the reduction of atmospheric clouds and precipitation. Then, it comes to the following question: what leads to the opposite signal, i.e. increase and decrease of the water vapor content, in the RDA and RWA.

4.4.2 Moisture change due to dynamical responses

To explore the source of the moisture variation, the dynamical responses of the climate are examined. Wang et al. (2005) pointed out that the main source of the summer precipitation in the Asian monsoon-dominated subregion is connected to the evolution of the EASM and SASM. In the westerlies-dominated subregion, the decrease (increase) of summer precipitation results from the regional descending (ascending) motion of air masses (Shi et al., 2016) that transported from adjacent areas (Chen et al., 2008). This indicates that the

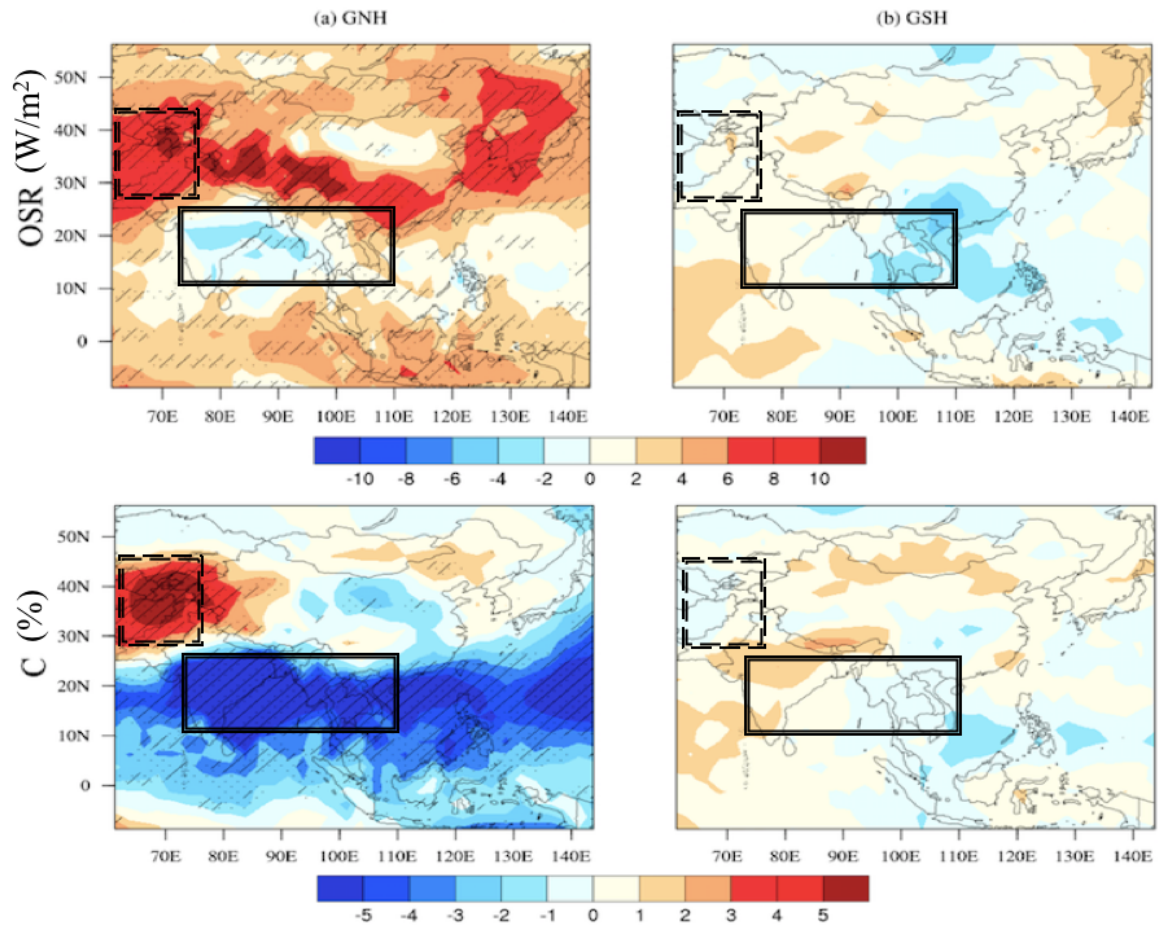


Fig. 4.6 Spatial distribution of top of the atmosphere outgoing shortwave radiation (TOA OSR, W/m^2 , top) in full sky and cloud area fraction (C, %, bottom) anomalies in the eruption year with respect to the average of the five years before the eruption. The solid and dashed black box indicates the relatively wettest area (RWA) and relatively driest area (RDA), respectively. Regions with black dots and slashes are significantly at the 95% and 99% confidence level.

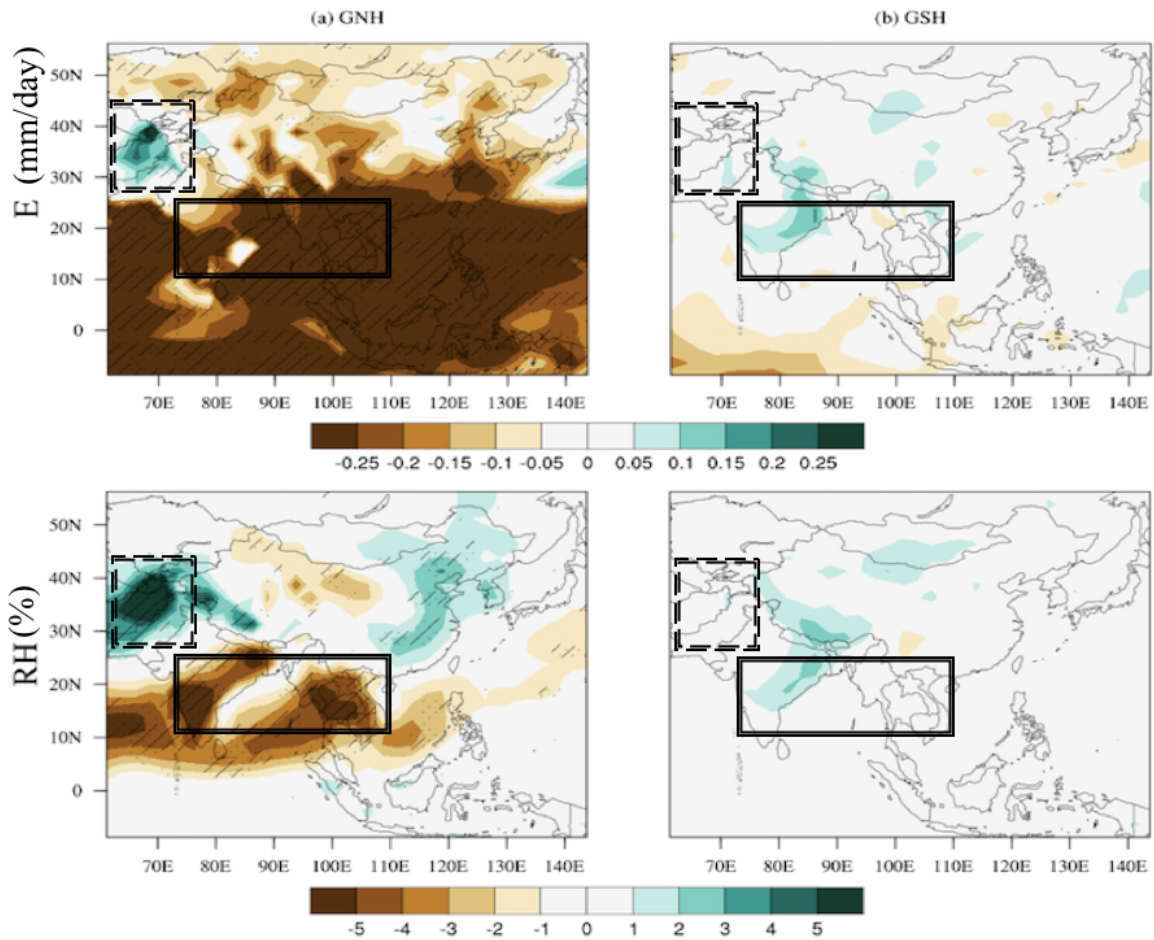


Fig. 4.7 Spatial distribution of evaporation (E, mm/day, top) and relative humidity (RH, %, bottom) anomalies in the eruption year with respect to the average of the five years before the eruption. The solid and dashed black box indicates the relatively wettest area (RWA) and relatively driest area (RDA). Regions with black dots and slashes are significantly at the 95% and 99% confidence level.

transport of water vapor in the monsoon and westerlies-dominated subregion is dominated by horizontal and vertical motion of the atmospheric circulation.

To study the horizontal motion of the atmospheric circulation, we examined the summer monsoon circulation. Temporal analyses indicate a significantly decreased land-ocean thermal contrast in the eruption year (year 0) and one year after the eruption (year 1) in the Asian monsoon region (figure 4.3 (b)), this results in weakened East and South Asian summer monsoon flow. Additionally, EASMI and SASMI were used to determine the weakening effect of Asian summer monsoon quantitatively. As shown in figure 4.8, both EASMI and SASMI decreased significantly in year 0, and the anomalous weakening effects were not recovered until year 3. This largely decreases the water vapor transport from the ocean to the land, thus leading to the decrease of evaporation in the RWA.

To assess the moisture flux and the vertical motion of the atmospheric circulation, the vertical integrated moisture flux (VIMF) and its divergence (VIMFD) were calculated. As shown in figure 4.9 (a), before the volcanic eruption, the RDA is controlled by the divergence of moisture flux and the water vapor is transported by the west and north-west winds. In the RWA, the southwest wind transports large amount of water vapor from the ocean to this area, which one can see a significant convergence area. This results in larger precipitation in the RWA compared to that in the RDA. After the NHVAI (figure 4.9 (b)), water vapor is transported from the ocean and the adjacent eastern highlands to the RDA by the southwest and east wind. The VIMFD indicates a strengthened convergence in this area. This results in an enhanced upward transport of large amounts of water vapor, which leads to more clouds and precipitation, and finally results in the significant wetting effect in this area. In the RWA, the northeast wind indicates a decreased transport of water vapor from the ocean to the land. The VIMFD also indicates a weakened convergence, which leads to less clouds and precipitation. Thus, the reduced horizontal transport of water vapor from the weakened summer monsoon and the weakened vertical motion result in the significant drying effect in the RWA.

4.4.3 Summary of the mechanism

Based on these results, the mechanism of the hydrological effects of NHVAI in these two representative areas of the monsoon and westerlies-dominated subregions can be summarized as follows: the direct radiative effect of stratospheric volcanic aerosols affects the atmospheric circulation. The decreased thermal contrast between the land and ocean resulted in the weakened EASM and SASM. It changes the moisture transport and the formation of clouds in different regions. The variation of precipitation, due to the radiative effect and physical feedback of the regional atmospheric clouds and water vapor, resulted in the drying and

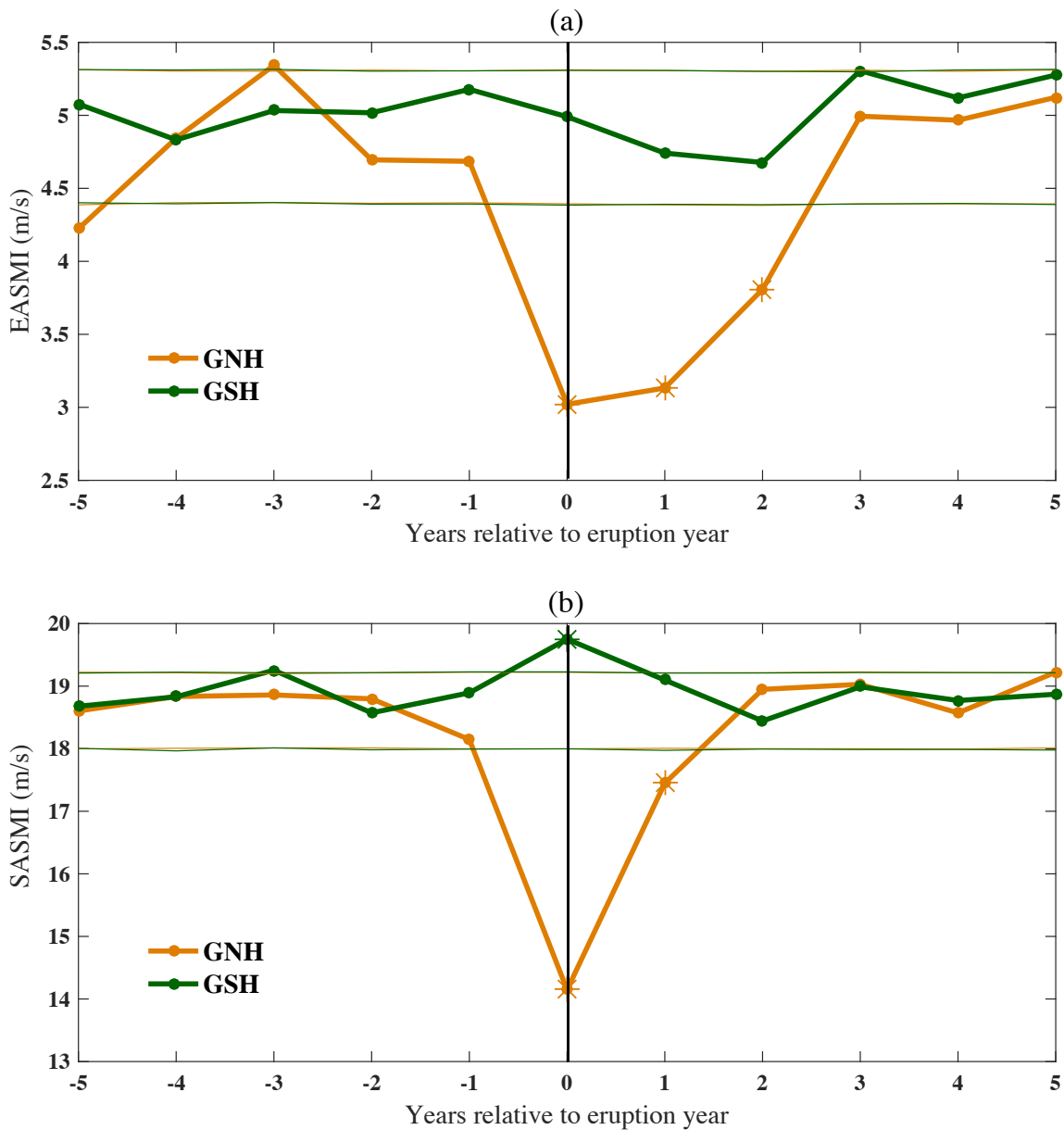


Fig. 4.8 Temporal SEA results of the East Asian summer monsoon index (EASMI, m/s, top) and South Asian summer monsoon index (SASMI, m/s, bottom) anomalies. The thinner lines stand for the Monte Carlo model results (method see chapter 2.4.3) at the 95% confidence level. The asterisks represent the years that passed the Monte Carlo model tests at the 99% confidence level. Year 0 represents the identified eruption year by volcanic forcing index, negative and positive years represent relative years before and after the eruption.

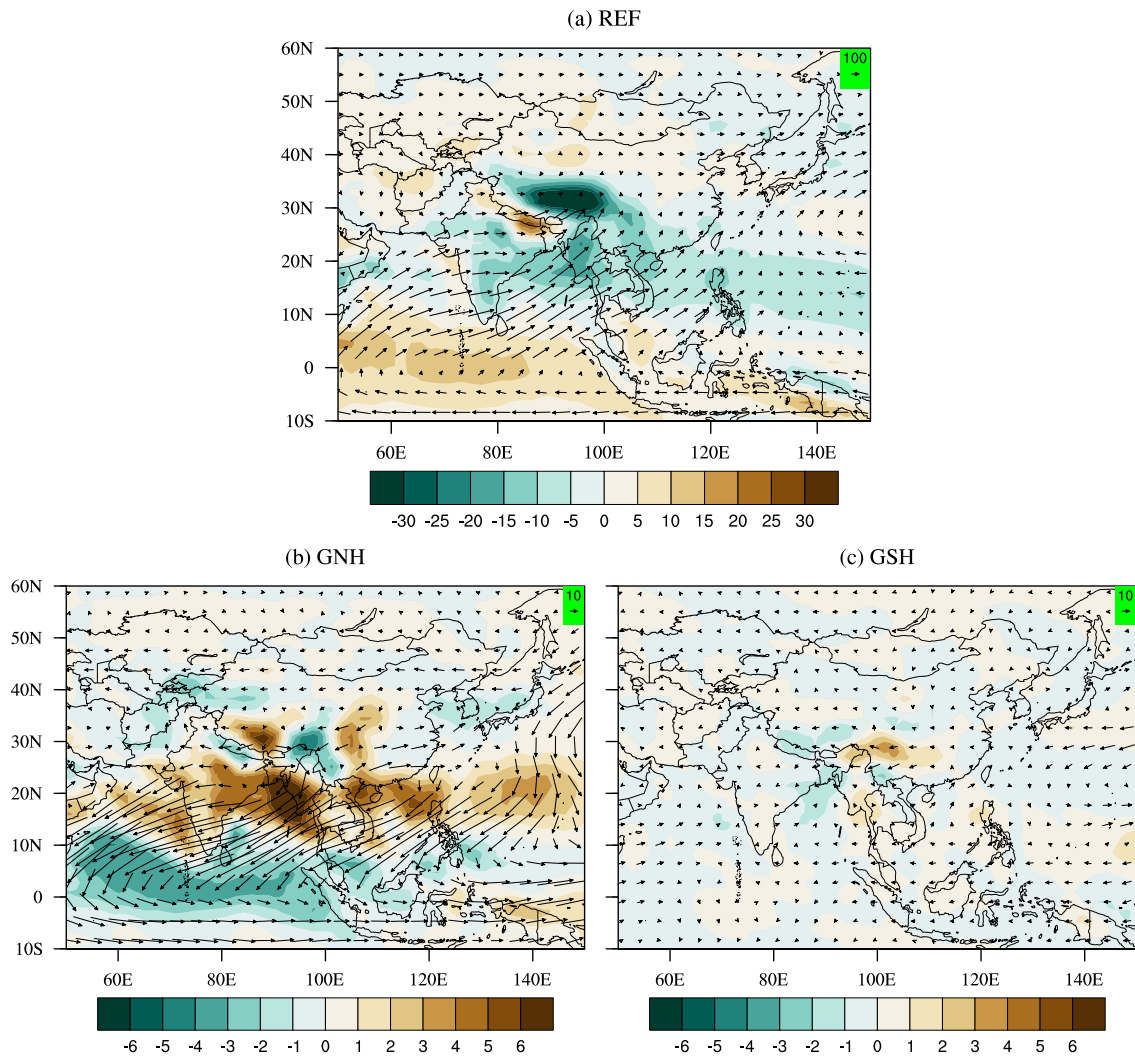


Fig. 4.9 Vertical integrated moisture flux (VIMF, $\text{kg/m}\cdot\text{s}$, vector) and its divergence (VIMFD, $10^{-5} \text{ kg/m}^2\cdot\text{s}$, shades) in five years before the eruption (a, REF) and the anomalies in the eruption year of the GNH (b) and GSH (c) classification.

wetting effects in different regions. Specifically, an increased transport of water vapor from the south and east areas, together with an enhanced upward motion contributed to the formation of clouds and precipitation, which resulted in the wetting effect in the RDA. In the RWA, the drying effect resulted from a decreased transport of the water vapor from the adjacent ocean to the land due to the weakened summer monsoon and weakened upward motion.

Although the mechanism is mainly based on the analysis in the RWA and RDA, where the strongest effects of volcanic eruptions can be found, these responses can be seen in most of the areas, but with a weaker amplitude. They, therefore, reflect the pervasive mechanism of the volcanic eruptions' hydrological effects in the monsoon and westerlies-dominated subregions.

Previous studies (Man et al., 2014; Peng et al., 2010) showed similar attributed mechanisms of the precipitation response to volcanic eruptions in the East Asian summer monsoon region. Specifically, Peng et al. (2010) indicated that the decrease of latent heat flux and the evaporation over tropical oceans led to the reduction of the summer precipitation in eastern China. Man et al. (2014) attributed the reduction of summer precipitation over EASM region to the decreased land-ocean thermal contrast and the subsequent weakening of summer monsoon circulation. Furthermore, Joseph and Zeng (2011) also found less cooling in areas near the equator. This regional warming effect was suggested to be associated with the reduction of clouds, while less evaporation due to the less precipitation further contribute to the regional warming. More recently, Paik and Min (2016) investigated the mechanism of the global precipitation response to volcanic eruptions, and suggested that the reduction of precipitation results from the reduction of the vertical motion from a weakened monsoon, which was attributed to the reduction of shortwave radiation and subsequent surface cooling. Results shown in this chapter agree with these conclusions. However, based only on temporal analyses, Paik and Min (2016) could not explain how the cooling and hydrological response was connected to the dynamic response. Our findings, based on both temporal and spatial analyses, fill in the gaps by explaining the mechanism that the dynamical response changes the transport of water vapor and the formation of regional atmospheric clouds, the radiative effect and physical feedback resulted in different temperature and precipitation responses in different areas. This thesis is the first study to explore the mechanism of different hydrological responses to volcanic eruptions in monsoon and westerlies-dominated subregion of Asia. This enables us to give a comprehensive explanation on the mechanism of different hydrological response to volcanic eruptions in different areas of monsoon Asia.

4.5 Different climate response to asymmetric volcanic aerosol loadings

As indicated by PDSI in the GSH classification, there might be wetting effects in the Asian monsoon region two years after the SHVAI (figure 4.2). As shown in figure 4.3, temperature over the land decreased slightly in the GSH classification (figure 4.3 (a)), but opposite to the GNH classification, in the GSH classification, the significantly increased land-ocean thermal contrast suggests a cooler effect over the ocean than over the land of the AMR (figure 4.3 (b)). This contributes to an inversed dynamical response and subsequent physical response of the atmospheric clouds and precipitation, which can be indicated by differences between the GNH and GSH classifications in the SASM region from most of the spatial patterns (figure 4.4 (b) to figure 4.7 (b) and figure 4.9 (b)). These indicate inversed hydrological effects of the SHVAI, particularly in the SASM region. The mechanism of the hydrological response, although inversed, still follows that as summarized in 4.4.3. This further validates our explanation on the mechanism of the hydrological response to the NHVAI.

The volcanic classifications based on the volcanic forcing reconstruction only identified small magnitudes of aerosol injections in the GSH classification. The large differences of aerosol magnitudes existed in the GNH and GSH classifications might bring large uncertainty to the conclusion, as these small aerosol concentrations have limited climate effects. This makes it difficult to compare with the significant climate effects of the NHVAI. Liu et al. (2016) and Zuo et al. (2018), based on a different criterion of volcanic classifications, have pointed out the inversed hydrological effects the asymmetric aerosol loadings may have on monsoon precipitation. Endeavors are also made to understand the mechanism of the hydrological effects over global monsoon regions (Zuo et al., 2018). However, their studies were based on volcanic classifications that included different magnitudes of volcanic aerosols and a different number of events. The temporal and spatial characteristics of different climate responses to volcanic eruptions in different hemispheres and their potential mechanisms are investigated with specifically designed model simulations in the next chapter.

Chapter 5

Simulation on climate effects of volcanic eruptions at different latitudes

This chapter uses volcanic forcing generated from EVA with the fully coupled climate model MPI-ESM-LR to test the hydrological effects of volcanic eruptions at different latitudes on the Asian monsoon. After identifying the most affected areas, further analyses were made in order to examine the mechanism on the climate effects of the different latitudinal volcanic eruptions.

5.1 Volcanic forcing from EVA

In order to explore the hydrological effects of volcanic eruptions in different hemispheres, and to test the different climate effects of tropical and extratropical volcanic eruptions, three different latitudinal volcanic eruption cases of 10-member simulations were performed with MPI-ESM-LR. The same characteristic parameters as the 1991 Pinatubo eruption, except for the eruption latitude, were prescribed in the three volcanic eruption cases (eruption date on June 15, 1991, total sulfur injection magnitude to be 9 Tg). The eruption latitudes are set at 30° N (NH case), 30° S (SH case) for the extratropical hemispheric eruptions and 0° (EQ case) for the tropical eruption in the EVA module.

The generated volcanic forcing is indicated by the aerosol optical depth at 550 nm (AOD₅₅₀). Figure 5.1 (above) shows the temporal variation of global mean AOD₅₅₀ in 1991-1996. The formation of sulfate aerosol after volcanic eruption increased the global mean AOD₅₅₀ and reached the maximum at 0.12 in December 1991. The patterns of zonal mean AOD₅₅₀ are the same among the three different latitudinal volcanic eruptions. Figure 5.1 (below) shows the spatio-temporal structure of the volcanic forcing. It takes several months

for the formation and the distribution of the aerosols, and the largest AOD₅₅₀ are shown in the boreal autumn of 1991. For the EQ case, the AOD₅₅₀ indicates that volcanic aerosols were distributed more dispersive to both hemispheres, and more aerosols were transported to the NH in the boreal winter of 1991 and the boreal spring of 1992 than to the SH. They are then quickly deposited in the boreal winter of 1992. However, the phenomenon that more aerosols are transported to the NH is dependent on the eruption season, and the connection to the circulation of the stratosphere. When in a test with the eruption month setting to December, more aerosols were transported to the SH than to the NH (not shown). This confirms the research findings made by Stevenson et al. (2016) that the eruption season has to be considered when studying the climate effects of volcanic eruptions. This study focuses on the climate effect of asymmetric volcanic aerosols, and since several model simulations have shown that the volcanic eruptions in boreal summer have larger climate effects than in other seasons Kravitz and Robock (2011); Predybaylo et al. (2017), only the boreal summer eruption is considered in this study. For the NH and SH cases, aerosols are mostly confined in the specific hemispheres. Larger AOD₅₅₀ are shown in the subtropical areas between 30° and 60° latitude. A larger poleward transport than equatorward transport is shown in both cases in the initial period after the eruption.

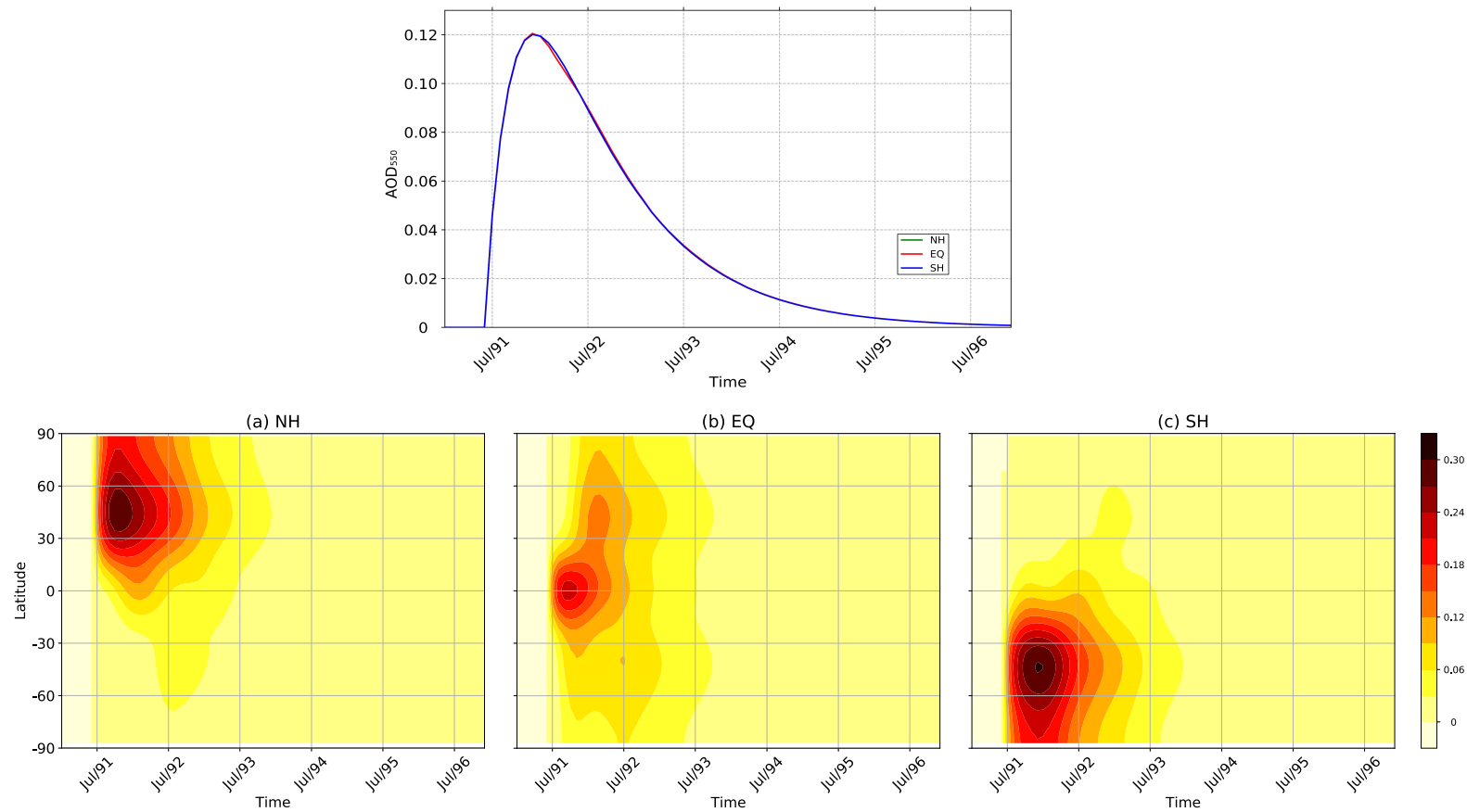


Fig. 5.1 Global mean aerosol optical depth anomaly at 550 nm (top) and its zonal mean distributions for the NH (a), EQ (b) and SH (c) volcanic eruption cases (bottom) generated by Easy Volcanic Aerosol (EVA) forcing generator (see chapter 2.5.1).

5.2 Climate response to volcanic eruptions at different latitudes

With the different volcanic forcing implemented in the MPI-ESM-LR model, the climate response to these different latitudinal volcanic eruptions are simulated. Both temporal and spatial analyses were performed to investigate the climate effects. The ensemble means of the 10 members were used in the analyses. Their anomalies with respect to the control runs without any volcanic eruption are presented.

5.2.1 Global radiative effects

To show the primary radiative effects of the distributed volcanic aerosols, the clear sky net shortwave radiation at the top of the atmosphere (TOA OSR) and surface temperature (T) are presented. Figure 5.2 shows the time series of global mean OSR (above) and its zonal mean distribution (below). The OSR value in the MPI-ESM-LR is negative, thus the negative OSR indicates an increase of the OSR after the volcanic eruptions, and the increase of the OSR lasts for three years until the boreal summer of 1994 for all the three cases. Although all three eruption cases have the same global mean AOD₅₅₀ (figure 5.1 top), a larger increase of OSR after the SH and EQ volcanic eruptions than the NH eruption can be found in the winter of 1991. The zonal mean distribution of the OSR (figure 5.2 bottom) indicates a simultaneous increase of OSR in the areas with a higher AOD in all the three cases in 1991 after the eruption, which confirms that more SR is reflected when there are more volcanic aerosols. In the NH case, more SR was reflected in the boreal summer and autumn seasons of 1992 than in the boreal winter of 1991. In the EQ and SH cases, the shape of the OSR zonal mean distribution is similar to the shape of the AOD₅₅₀ variation.

This decreases the solar radiation reaching the surface and leads to a surface cooling. Figure 5.3 shows the time series of global mean T (top) and its zonal mean distribution (bottom). Significant cooling effects are shown after the volcanic eruptions, and the largest cooling effects are shown in the boreal summer of 1992 for all three cases. However, different response patterns emerge among the three eruption cases. Specifically, for the NH and EQ cases, T decreased largely in the boreal summer of 1991 and 1992, but increased in the boreal winter of 1991. These winter warming effects are in agreement with previous studies Kirchner et al. (1999); Zambri and Robock (2016), which result from the dynamical response to the enhanced stratospheric latitudinal temperature gradient after a volcanic eruption (Kirchner et al., 1999). For the SH case, T decreased continuously until the boreal summer of 1992. From the zonal mean distribution of temperature (figure 5.3 bottom), it shows larger cooling

effects in 1992 and in the corresponding areas with more reflected SR by volcanic in all three cases. For the NH case, it causes a cooling immediately after the eruption in 1991, and then the cooling effect is slightly delayed compared to the OSR variation in 1992. For the EQ and SH cases, the surface cooling effects are shown several months later compared to the OSR variation. These different responses originate from the delayed response in the ocean compared to the land, because the ocean has larger heat content compared to the land and the NH has larger landmass compared to the SH. These responses are similar to those summarized in previous studies (Robock, 2000, 2015).

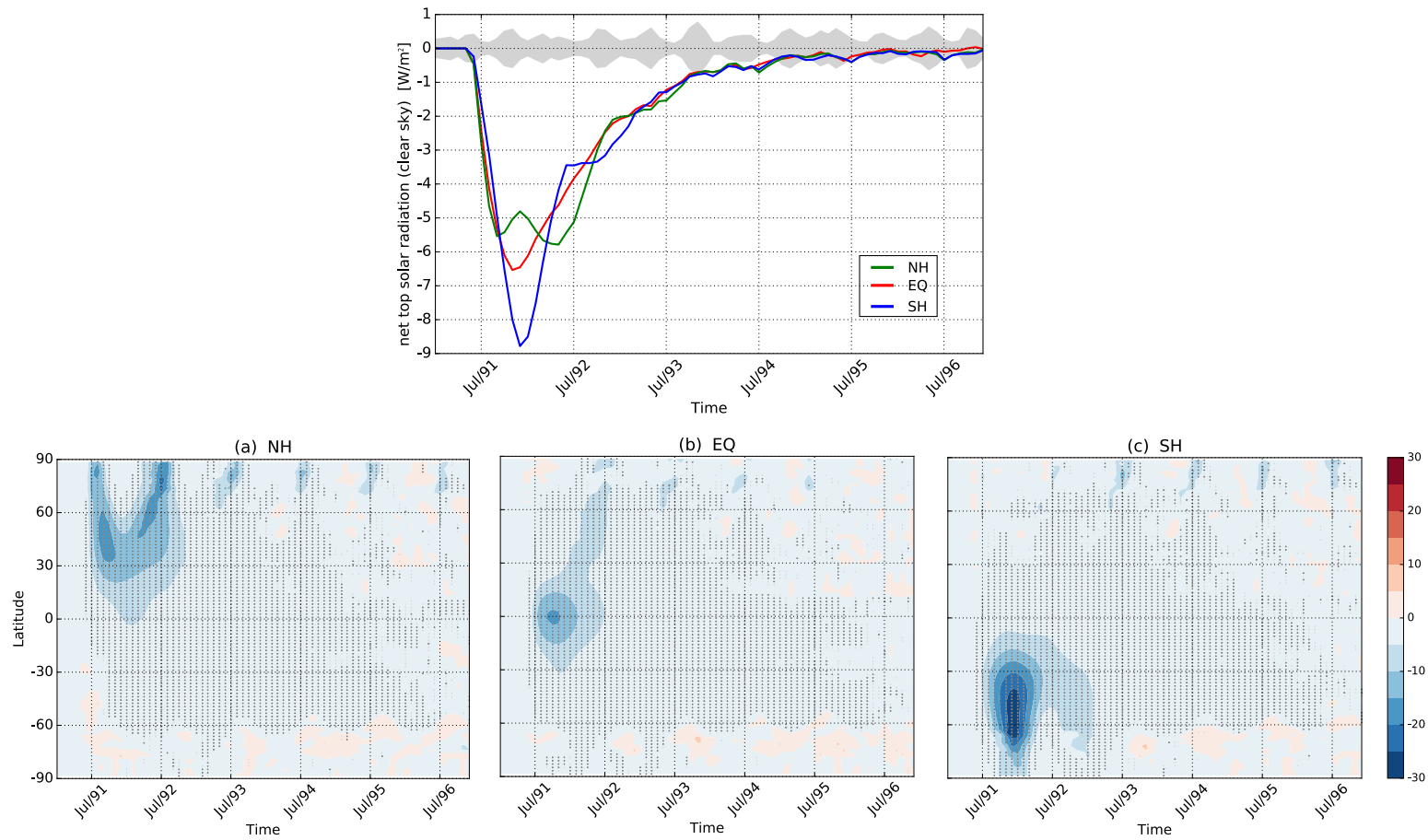


Fig. 5.2 Global mean net solar radiation (W/m^2) anomaly at top of the atmosphere in clear sky (top) and its zonal mean distributions for the NH (a), EQ (b) and SH (c) volcanic eruption cases (bottom). The grey shade indicates two standard deviation of the control runs without any volcanic eruption. The vertical bars and plus signs indicate the grids that passed the significance test at the 95% and 99% confidence level based on two-tailed student's t-tests.

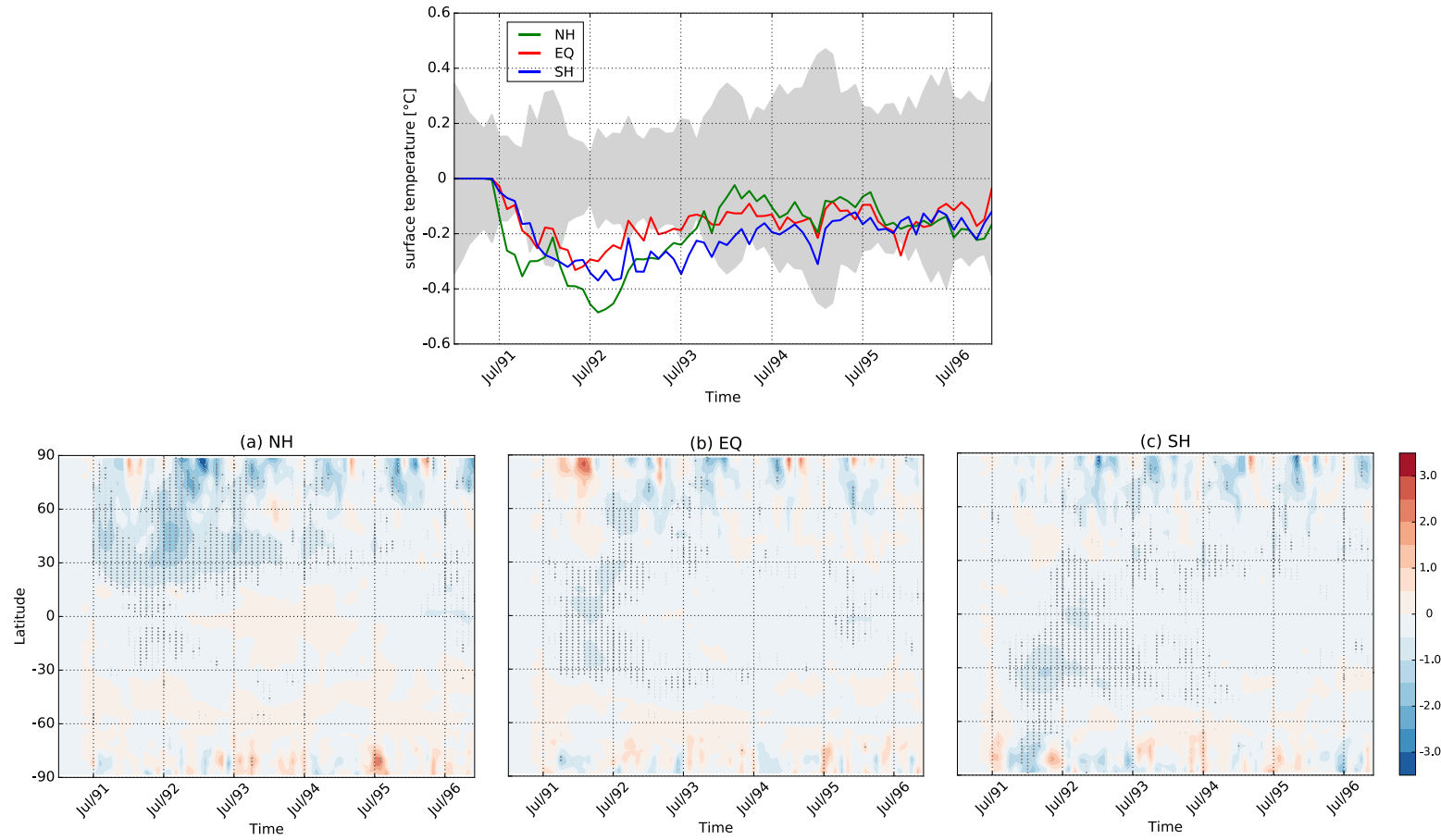


Fig. 5.3 Global mean surface temperature ($^{\circ}\text{C}$) anomaly (top) and its zonal mean distributions for the NH (a), EQ (b) and SH (c) volcanic eruption cases (bottom). The grey shade indicates two standard deviation of the control runs without any volcanic eruption. The vertical bars and plus signs indicate the grids that passed the significance test at the 95% and 99% confidence level based on two-tailed student's t-tests.

5.2.2 Climate effects in the Asian monsoon region

The discussion now focuses on volcanic eruptions' climate effects in the Asian monsoon region (AMR, 8.75°S–56.25°N, 61.25°E–143.75°E). Temporal analyses on boreal summer JJA mean temperature and precipitation were conducted firstly. As shown in figure 5.4 (a), the temperature decreased significantly in the boreal summer of 1992 and 1993 for all three eruption cases, with the strongest and weakest cooling after the NH and SH volcanic eruptions. For the NH and EQ cases, the largest reduction of the temperature is shown in 1992, while for the SH case, temperature decreased largely in 1992, and further decreased slightly with the largest reduction in 1993. Figure 5.4 (b) shows different precipitation responses to different latitudinal volcanic eruptions. Asian summer monsoon precipitation decreased largely after the NH volcanic eruption, but tended to increase after the SH eruption in 1992, then gradually recovered. For the EQ case, a slower response but with a continuous increase from 1992 to 1994 can be found. This suggests an inversed tendency of precipitation response to the NH and SH volcanic eruptions, which is similar to the conclusion at the end of chapter 4 on the different hydrological effects of interhemispherically asymmetric volcanic aerosol injections.

The spatial distribution of the climate response was further investigated. Since the largest and different climate effects are mostly visible in 1992, we focused our spatial analyses on JJA mean of 1992. Figure 5.5 shows the spatial distribution of the temperature anomaly. For the NH case, significant cooling (99% confidence level) are shown in most of the AMR, except for India, where it shows warming (figure 5.5 (a)). For the EQ case, the significant cooling (99% confidence level) are shown in the western and southern AMR, and the largest cooling can be seen in India. Warming is shown in central east AMR, but rarely passed the significance test, except for the warming in the boundary areas of east Mongolia and north China, where they passed the significance test at the 95% confidence level (figure 5.5 (b)). For the SH case, significant cooling (99% confidence level) are shown in south and central parts of the AMR, while slight warming is shown in the northeast part of AMR (figure 5.5 (c)).

The spatial pattern of precipitation in figure 5.6 indicates drying effects in India after the NH volcanic eruption (figure 5.6 (a)), while significant wetting effects can be found after the EQ and SH volcanic eruptions (figure 5.6 (b) and (c)). These two figures clearly indicate the opposite climate effects brought by the NH and SH volcanic eruptions, which are particularly strong in India. This is in agreement with the findings shown in chapter 4 based on analyses of CMIP5 model output that the different hydrological effects are mainly focused in the relatively wettest area (RWA), especially in the Indian summer monsoon

region. The following part of this chapter aims at explaining the mechanism of different climate responses to volcanic eruptions at different latitudes in India.

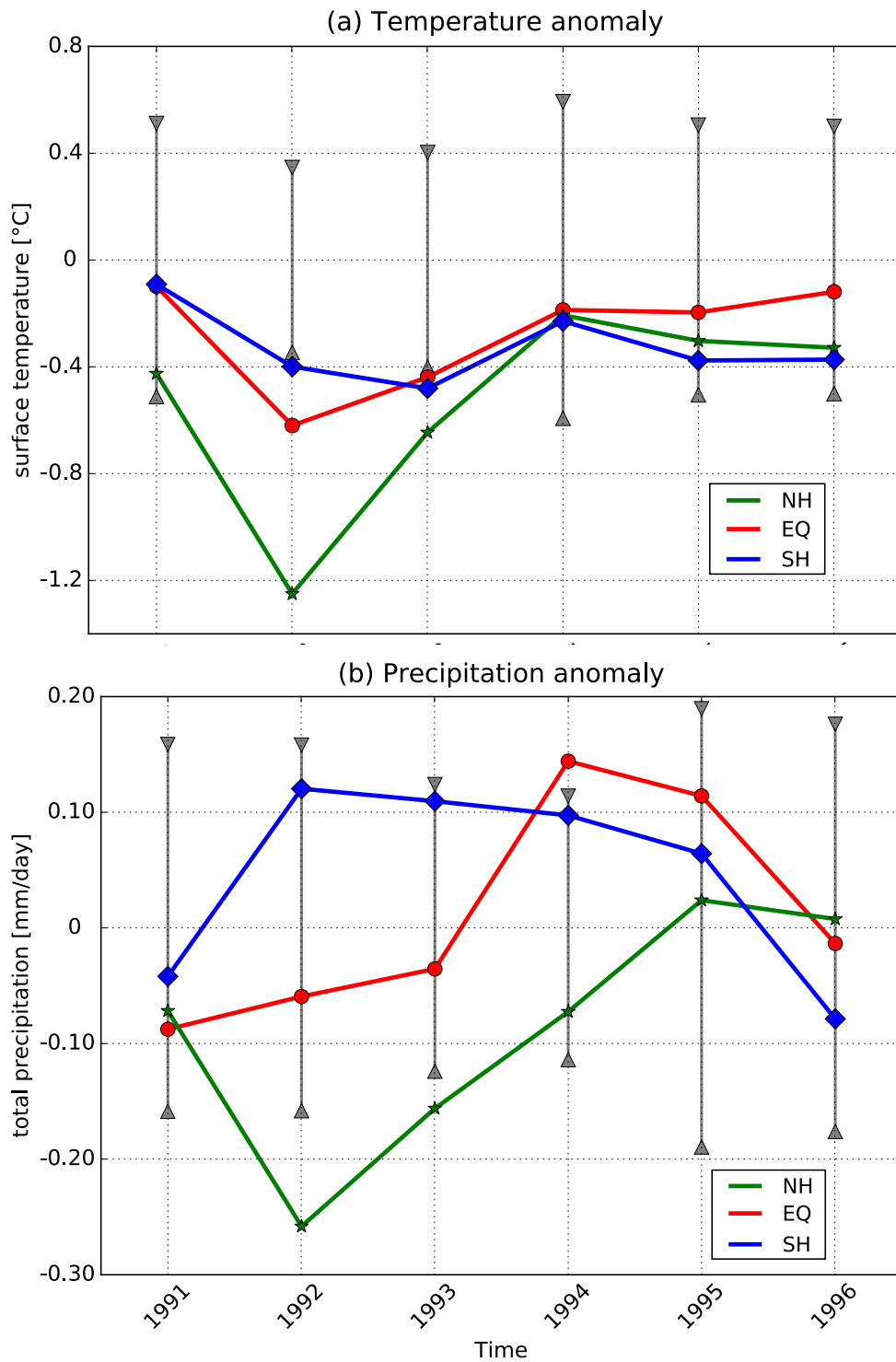


Fig. 5.4 JJA mean temperature ($^{\circ}\text{C}$, a) and precipitation (mm/day, b) anomaly over the land of the Asian monsoon region (8.75°S – 56.25°N , 61.25°E – 143.75°E). The grey bar indicates two (a) and one (b) standard deviation of the control runs without any volcanic eruption.

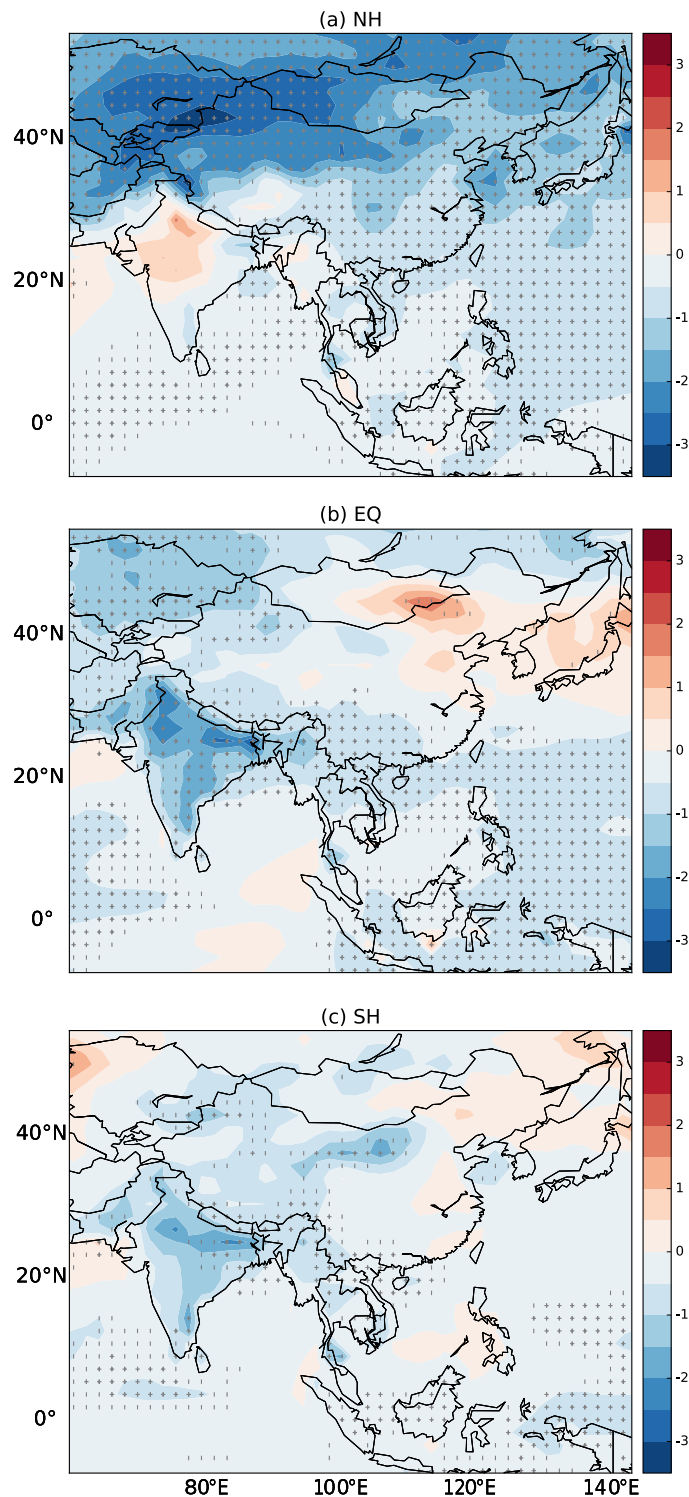


Fig. 5.5 Spatial distribution of JJA mean temperature ($^{\circ}\text{C}$) anomaly in 1992 in the Asian monsoon region for the NH (a), EQ (b) and SH (c) volcanic eruption cases. The vertical bars and plus signs indicate the grids that passed the significance test at the 95% and 99% confidence level based on two-tailed student's t-tests.

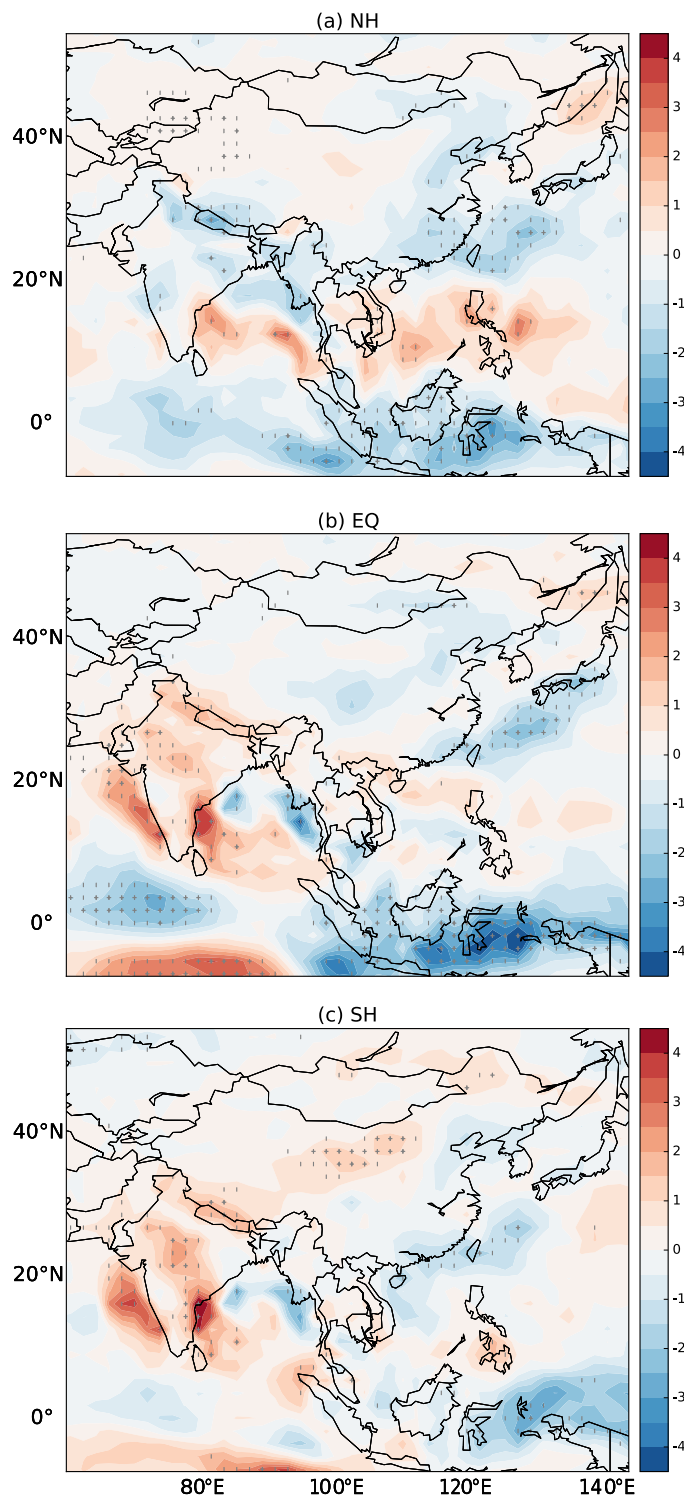


Fig. 5.6 Spatial distribution of JJA mean precipitation (mm/day) anomaly in 1992 in the Asian monsoon region for the NH (a), EQ (b) and SH (c) volcanic eruption cases. The vertical bars and plus signs indicate the grids that passed the significance test at the 95% and 99% confidence level based on two-tailed student's t-tests.

5.2.3 ENSO responses to volcanic eruptions at different latitudes

The relationship between volcanic eruptions and ENSO and their potential concurrent impacts on the climate are unresolved issues. The impact of volcanic eruption on ENSO variation deserves to be studied. In this study, 10-member simulations are performed with initial conditions that leave out ENSO event in 1990-1992, thus the simultaneous occurrence of ENSO event with volcanic eruptions is suppressed. As shown in figure 5.7, Oceanic Niño Index (ONI, see chapter 2.4.5) indicates that the members of the 10 control runs have some variations, but no ENSO event emerges during the study period (The El Niño or La Niña event occurs only when the ONI is continuously over 0.5 or below -0.5 for 5 months). For the NH case (figure 5.7 (a)), ONI decreases slightly at first but then increases to over 0.5 from the boreal summer of 1992 to the end of 1994, which suggests a tendency towards a stronger and longer period of El Niño event in one to three years after the NH volcanic eruption. A similar tendency towards El Niño was found in Pausata et al. (2015), in which the tendency suggested to be the result of the southward movement of ITCZ due to the weakening of the trade wind in the western and central part of equatorial Pacific Ocean. For the EQ case (figure 5.7 (b)), ONI decreases in the boreal winter of 1991 but then increases to over 0.5 from the boreal summer of 1992 to the boreal summer of 1993, and then decreases to negative from the boreal summer of 1994 to the boreal summer of 1996. This suggests that ENSO tilts to the positive phase one year after the EQ volcanic eruption and then to a negative phase three years after the EQ eruption. This is in agreement with Mann et al. (2005) and Maher et al. (2015). For the SH case (figure 5.7 (c)), ONI is continuously negative until the boreal summer of 1994, which indicates a tendency to tilt to the negative phase of ENSO after the SH volcanic eruption. Stevenson et al. (2016) also found a La Niña tendency after the SH volcanic eruption and the opposite response of ENSO to different hemispheric volcanic eruptions. A more detailed analysis to understand the mechanism of the ENSO response to volcanic eruptions exceeds the scope of this thesis.

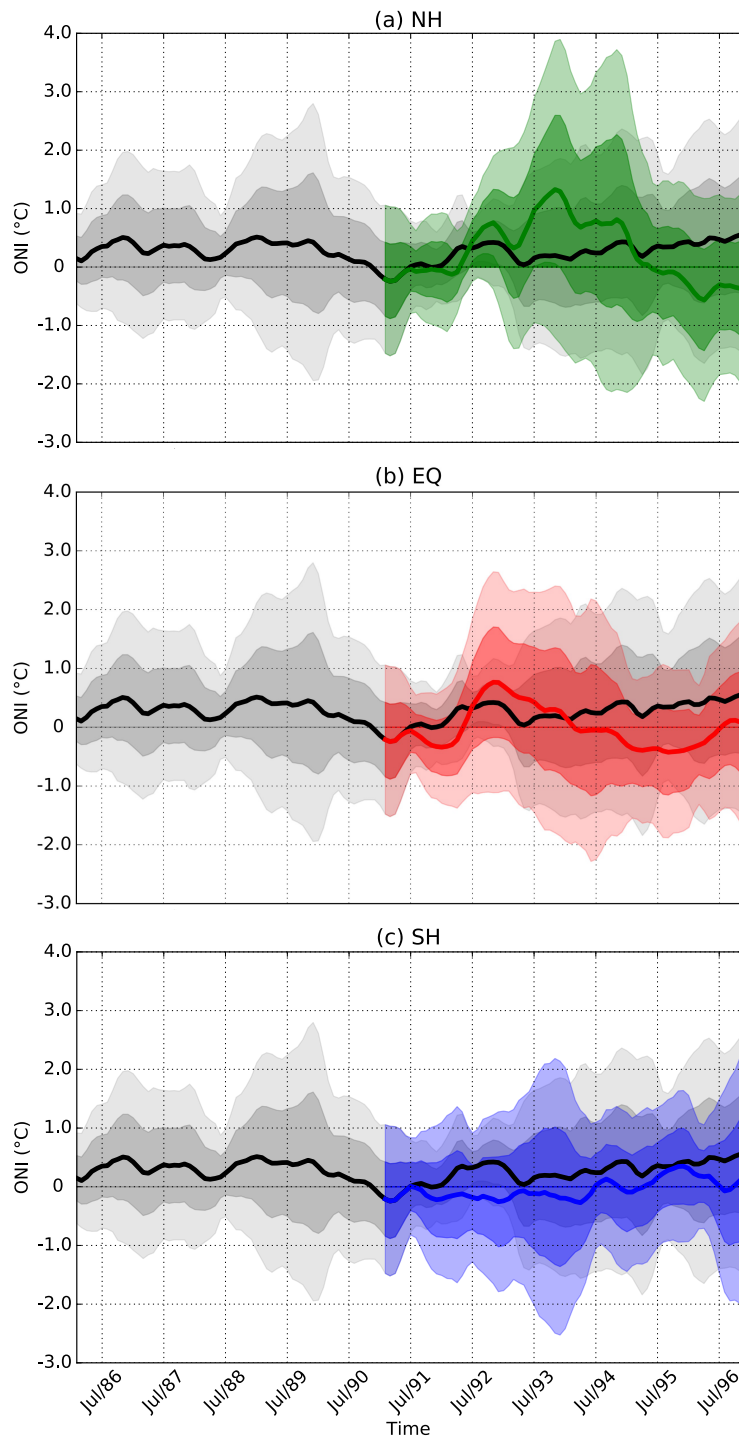


Fig. 5.7 Time series of Oceanic Niño Index ($^{\circ}\text{C}$) anomaly for the NH (a), EQ (b) and SH (c) volcanic eruption cases. The black and relative solid color lines are the ensemble member means of the control run and the eruption cases. The dark (light) grey and relative heavy (light) color shades represent one (two) standard deviation of the control runs and the eruption cases.

5.3 Mechanisms of climate responses to different latitudinal volcanic eruptions in India

5.3.1 The direct radiative effect and dynamical response

Stratospheric aerosols injected by an explosive volcanic eruption reflected more solar radiation (figure 5.2), thus bringing significant surface cooling (figure 5.3). These cooling effects are more pronounced in the areas with more aerosols. Since the volcanic aerosols are asymmetrically distributed after the three latitudinal volcanic eruptions (figure 5.1), they bring asymmetric cooling effects between the two hemispheres. Figure 5.8 (a) shows the difference of the summer mean temperature between northern and southern hemispheres. It decreased largely (slightly) in 1992 after NH (EQ) volcanic eruptions, while increased slightly after SH volcanic eruption. This indicates a larger cooling in the NH than in the SH after the NH and EQ volcanic eruption, while a larger cooling in the SH than in the NH is shown after the SH volcanic eruption. The thermal contrast between the two hemispheres moves the ITCZ away from the cooler hemisphere (Broccoli et al., 2006). In the boreal summer, large amounts of precipitation are concentrated around 10°N where the ITCZ is. As shown in figure 5.8 (b), the zonal mean precipitation is largely decreased around 10°N but increased around 0° after the NH volcanic eruption. This indicates that the ITCZ moves southward to the equator. The zonal mean precipitation is largely increased around 10°N but decreased around equator after SH volcanic eruption, which indicates the northward movement of the ITCZ. For the EQ case, because the aerosols are distributed in both hemispheres, the precipitation along the ITCZ is altered, with a decreased precipitation around 10°N but increased in the north and south of it, which particularly affects India.

Due to a larger heat content in the ocean, the temperature response over the ocean is delayed compared to the land. This leads to a stronger cooling of the land compared to the ocean. This decreases the land-ocean thermal gradient and results in a weakening of the summer monsoons (Dogar and Sato, 2019; Iles and Hegerl, 2014; Zuo et al., 2019). These studies come to the conclusion which is based on a qualitative analysis that the monsoon is driven by the land-ocean thermal contrast. The effects of volcanic eruptions in different hemispheres on the monsoon has only marginally been explored by Liu et al. (2016) and Zuo et al. (2019). In this study, the Indian summer monsoon is quantitatively studied based on the South Asian summer monsoon index (SASMI, Webster and Yang (1992)). As shown in figure 5.9, SASMI decreased continuously from 1992 to 1994 after the NH volcanic eruption, while it increased significantly and slightly in 1992 after the SH and EQ volcanic eruption.

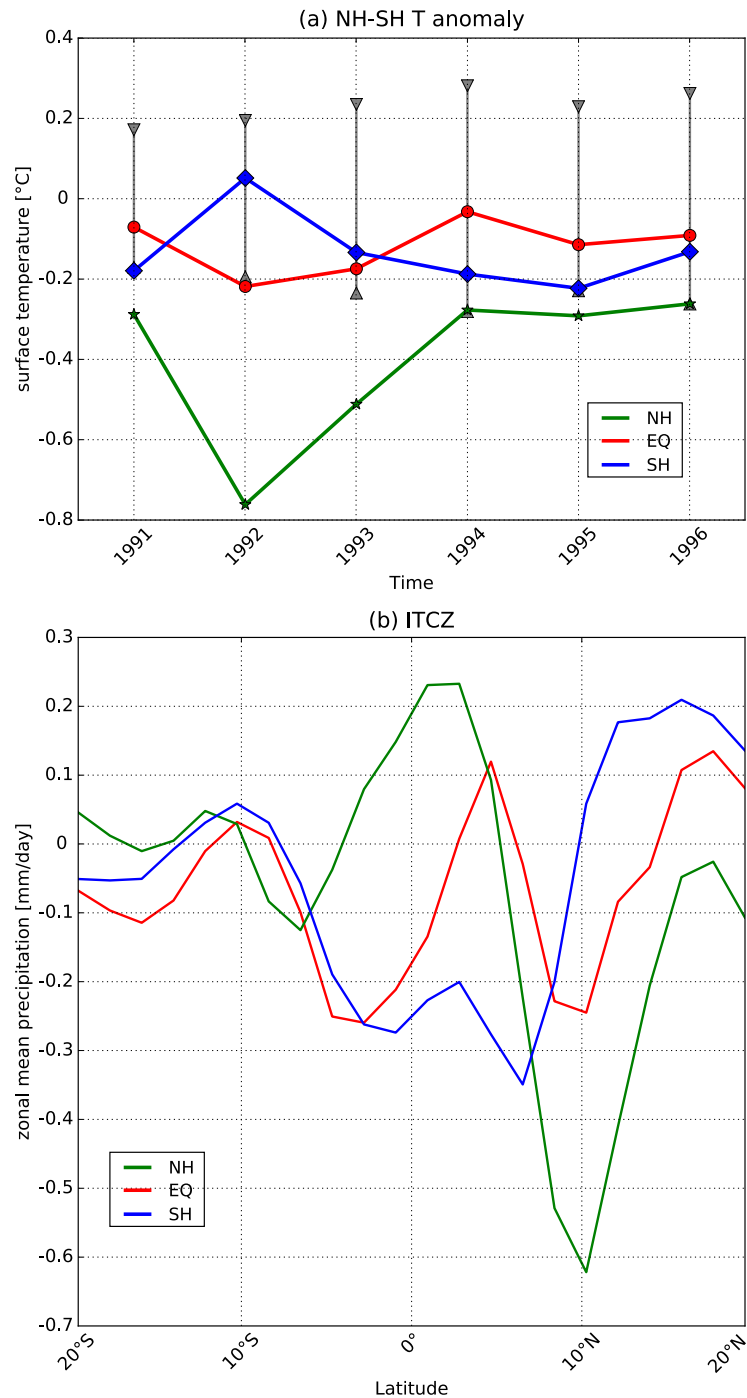


Fig. 5.8 Difference of JJA mean temperature ($^{\circ}\text{C}$) anomaly between northern and southern hemisphere (a) and ITCZ in 1992 (b) indicated by the JJA mean zonal mean precipitation (mm/day) anomaly between 20°N and 20°S . The grey bar in (a) indicates the two standard deviation of the control runs.

This indicates the opposite weakening and strengthening effects on the SASM after the NH and SH volcanic eruptions.

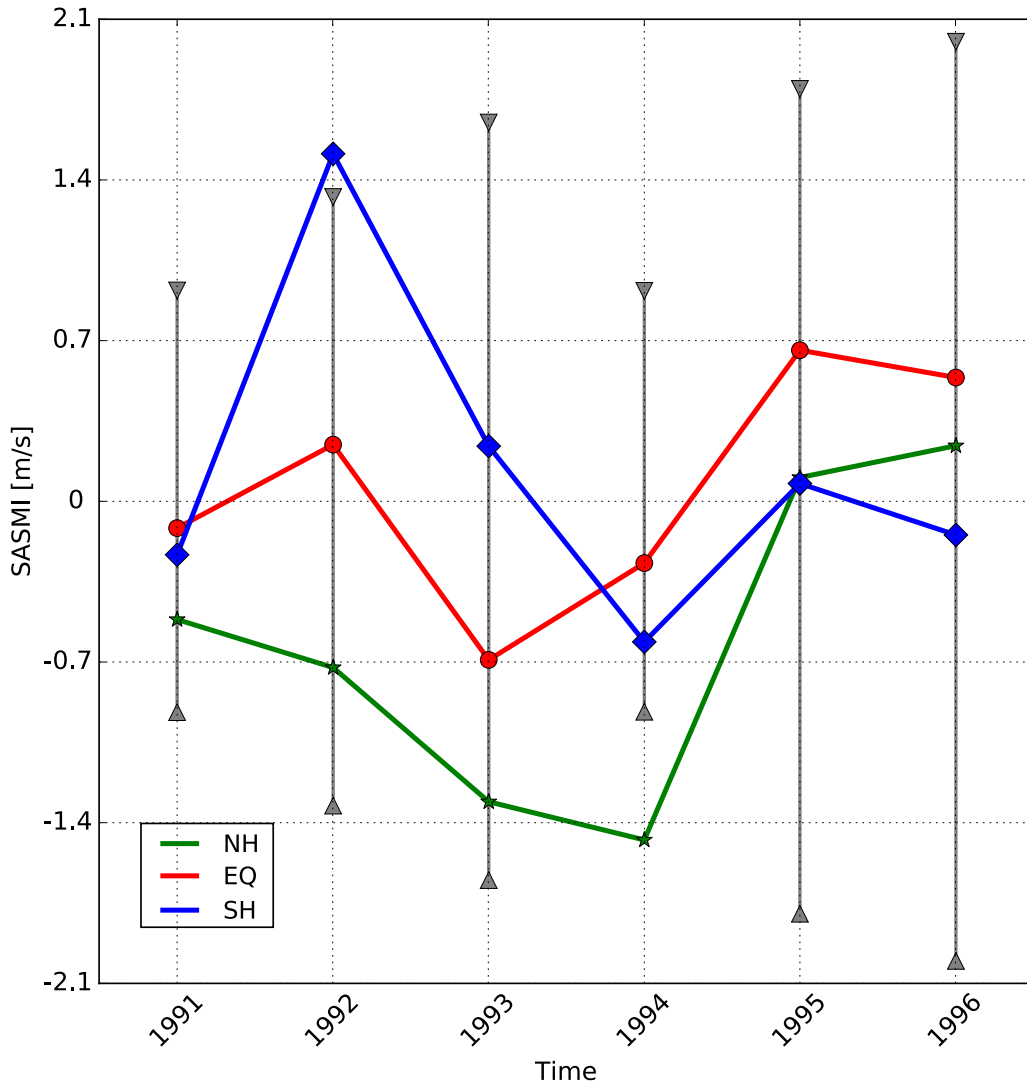


Fig. 5.9 South Asian summer monsoon index (m/s, method see chapter 2.4.5) anomaly. The grey bar indicates one standard deviation of the control runs.

The altered land-ocean thermal contrast largely changes the moisture transport from the ocean to India. Figure 5.10 shows the vertically integrated moisture flux (vector) and its divergence (shaded) in India. For the control runs without any volcanic eruption, as shown in figure 5.10 (a), in the western part of India, the wind from the Arabian Sea brings a large amount of moisture to the land. This results in a strong precipitation in the western coast of India. In the eastern and northern parts of India, the moisture is transported from the Bay of Bengal to the land, and lifted over the barrier of the Himalaya. This causes air

subsidence along the southern edge of the Himalaya (brown shade) while air lifting in the eastern part of India (blue-green shade), as shown by the VIMFD. After the NH volcanic eruption, the moisture transported from the ocean to the land is decreased, especially the moisture flux from Arabian Sea to the western coast of India. The reduced convergence in the northern part and northeastern coast of India indicates a diminished upward motion (figure 5.10 (b)). Whereas, after the EQ and SH volcanic eruptions (figure 5.10 (c) and (d)), more moisture is transported to the land, especially from the Bay of Bengal. The upward motion is diminished due to the reduced convergence in the northern part and northeastern coast of India, while strengthened in the western part and southeastern coast of India, as can be seen by the decreased divergence. The altered horizontal and vertical motion of the atmospheric circulation changes the amount and distribution of moisture in the atmosphere over India.

These results show the connection between the direct radiative effect of volcanic aerosol and the indirect dynamical response of the climate system. The hemispheric thermal gradient moves the ITCZ toward south (north) after the NH (SH and EQ) volcanic eruptions (figure 5.8 (b)), this largely affects regional precipitation in the areas along the ITCZ. The altered land-ocean thermal gradient diminishes (strengthens) the horizontal and vertical motion of the air in India after the NH (SH and EQ) volcanic eruptions, this changed the transport of moisture to India. These dynamical responses influence the regional climate in India.

5.3.2 The role of atmospheric clouds and water vapor

In order to examine the regional climate response, the spatial patterns of several selected climate variables were analyzed. Following describes the subsequent physical feedback of atmospheric cloud and water vapor, which confirms the response chain as summarized from the analyses on CMIP5 models. Figure 5.11 shows the clear sky net surface solar radiation. It suggests a general synchronized reduction of the surface solar radiation in the same latitudes after all the three volcanic eruption cases, which resulted from the evenly distributed volcanic aerosols in the same latitude. It shows a larger decrease of the surface solar radiation in the northern (southern) part of the area after NH and SH volcanic eruptions, while a uniform decrease after EQ eruption. This is due to the reflection of the solar radiation by the asymmetric distribution of volcanic aerosols in two hemispheres after NH and SH volcanic eruptions, while being approximately balanced between the two hemispheres after EQ eruption. When looking into the full sky net surface solar radiation (figure 5.12), an opposite decrease and increase of the surface solar radiation are shown in different regions. Specifically, in India, the net surface solar radiation increased after NH volcanic eruption (figure 5.12 (a)), but decreased after SH and EQ volcanic eruptions (figure 5.12 (c) and (b)). This leads to the temperature increase (decrease) after NH (SH and EQ) in India (figure 5.5),

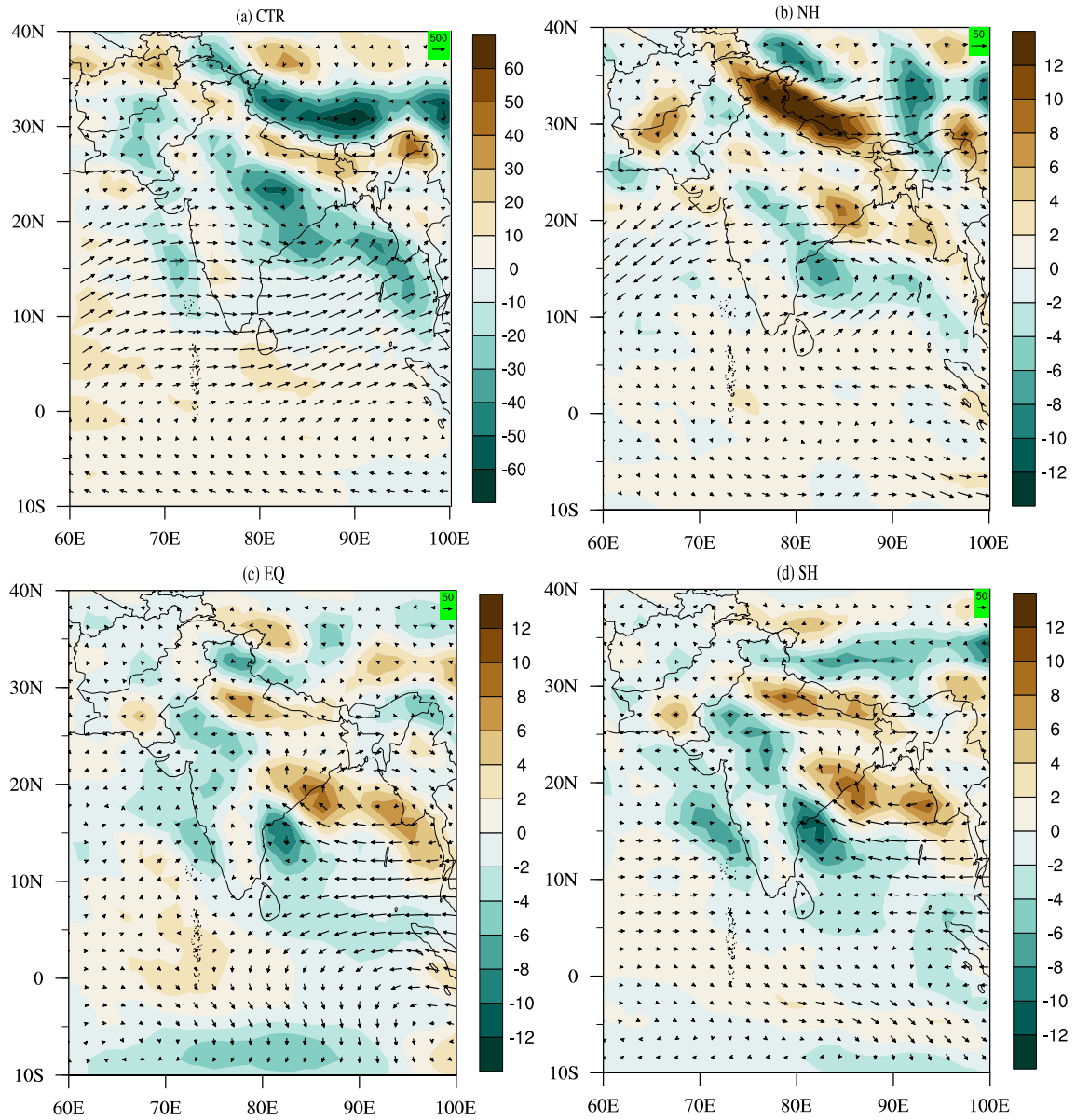


Fig. 5.10 JJA mean vertically integrated moisture flux (vector, $\text{kg/m}\cdot\text{s}$) and its divergence (shaded, $10^{-5} \text{ kg/m}^2\cdot\text{s}$) for the control runs without any volcanic eruption (a), and their anomalies after the NH (b), EQ (c) and SH (d) volcanic eruptions in 1992.

and is connected to the change of the total cloud cover. As shown in figure 5.13, it shows a significant decrease of cloud cover after NH volcanic eruption (figure 5.13 (a)), while increased after SH and EQ eruptions (figure 5.14 (c) and (b)). Less (more) SR is reflected with less (more) clouds, thus leading to the increase (decrease) of net surface SR and T after NH (SH and EQ) volcanic eruption.

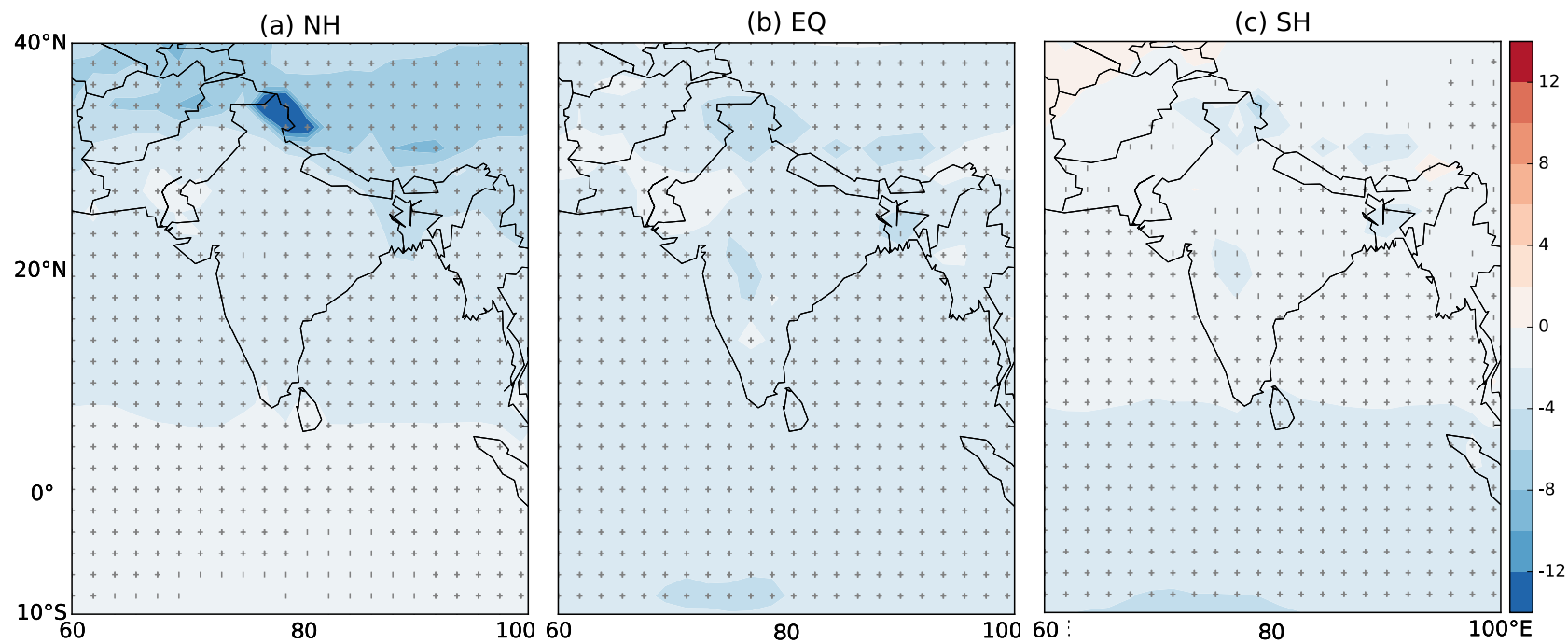


Fig. 5.11 Spatial distribution of JJA mean net surface solar radiation (W/m^2) anomaly in the clear sky after the NH (a), EQ (b) and SH (c) volcanic eruptions in 1992. The vertical bars and plus signs indicate the grids that passed the significance test at the 95% and 99% confidence level based on two-tailed student's t-tests.

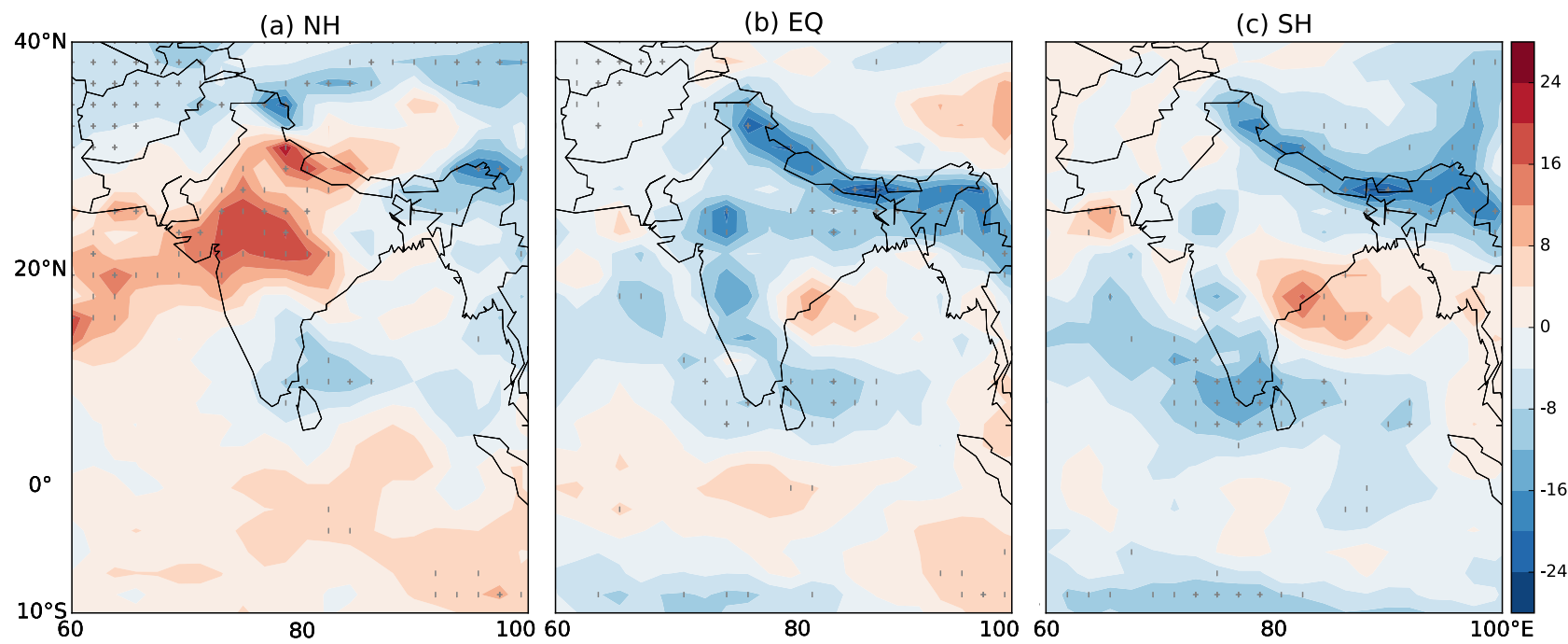


Fig. 5.12 Spatial distribution of JJA mean net surface solar radiation (W/m^2) anomaly in the full sky after the NH (a), EQ (b) and SH (c) volcanic eruptions in 1992. The vertical bars and plus signs indicate the grids that passed the significance test at the 95% and 99% confidence level based on two-tailed student's t-tests.

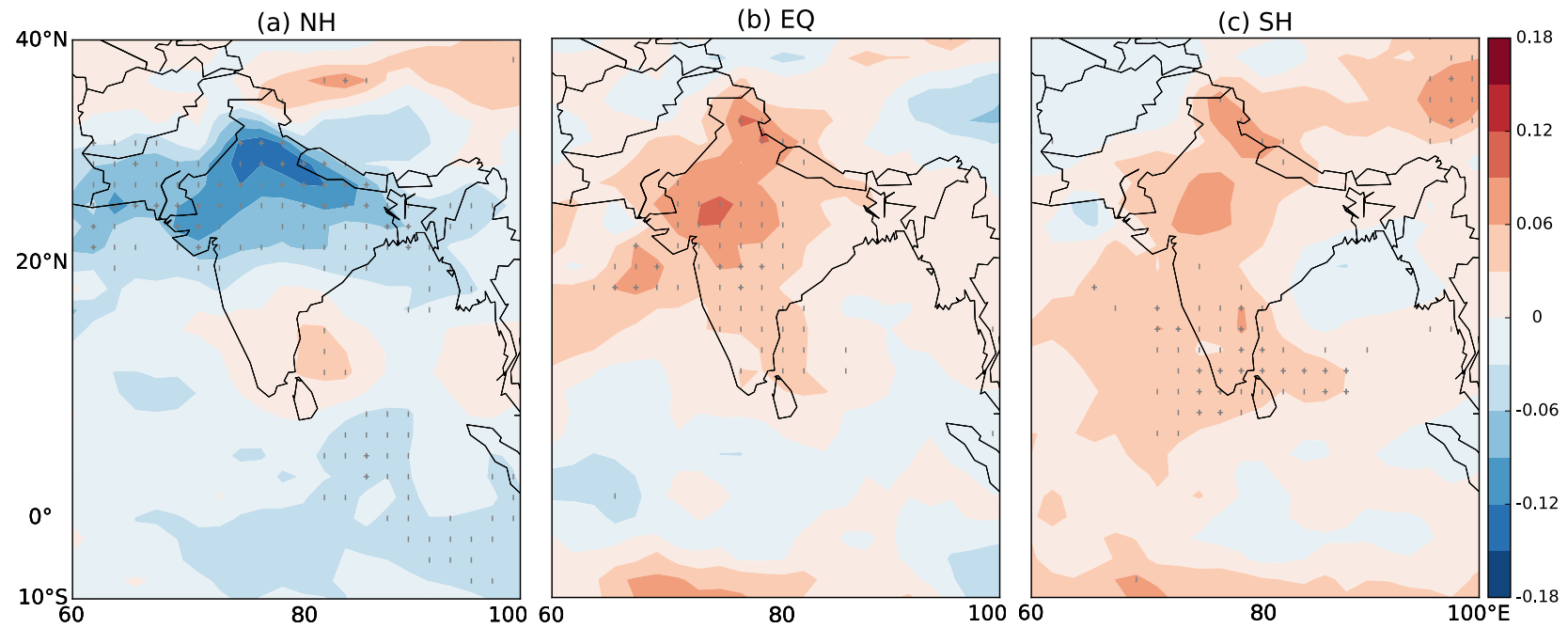


Fig. 5.13 Spatial distribution of JJA mean total cloud cover (%) anomaly after the NH (a), EQ (b) and SH (c) volcanic eruptions in 1992. The vertical bars and plus signs indicate the grids that passed the significance test at the 95% and 99% confidence level based on two-tailed student's t-tests.

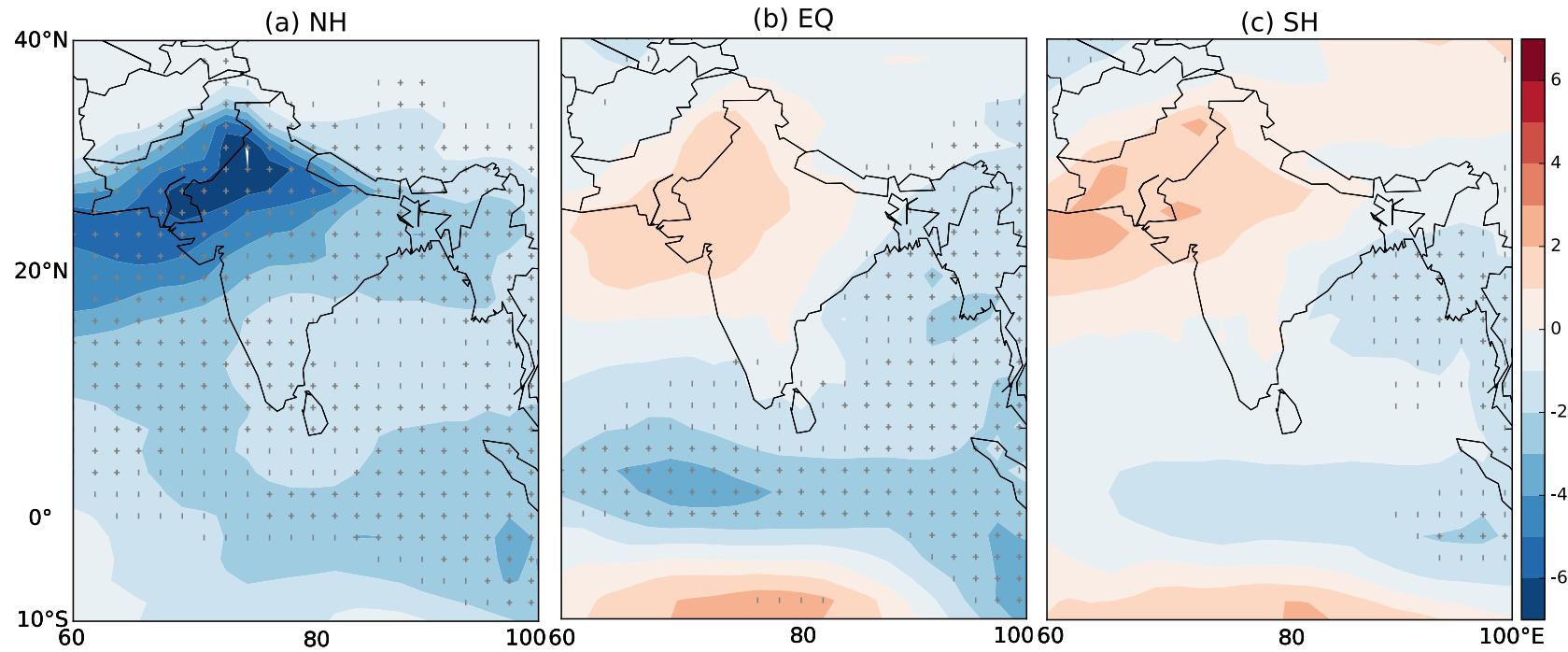


Fig. 5.14 Spatial distribution of JJA mean vertical integrated water vapor (kg/m^2) anomaly after the NH (a), EQ (b) and SH (c) volcanic eruptions in 1992. The vertical bars and plus signs indicate the grids that passed the significance test at the 95% and 99% confidence level based on two-tailed student's t-tests.

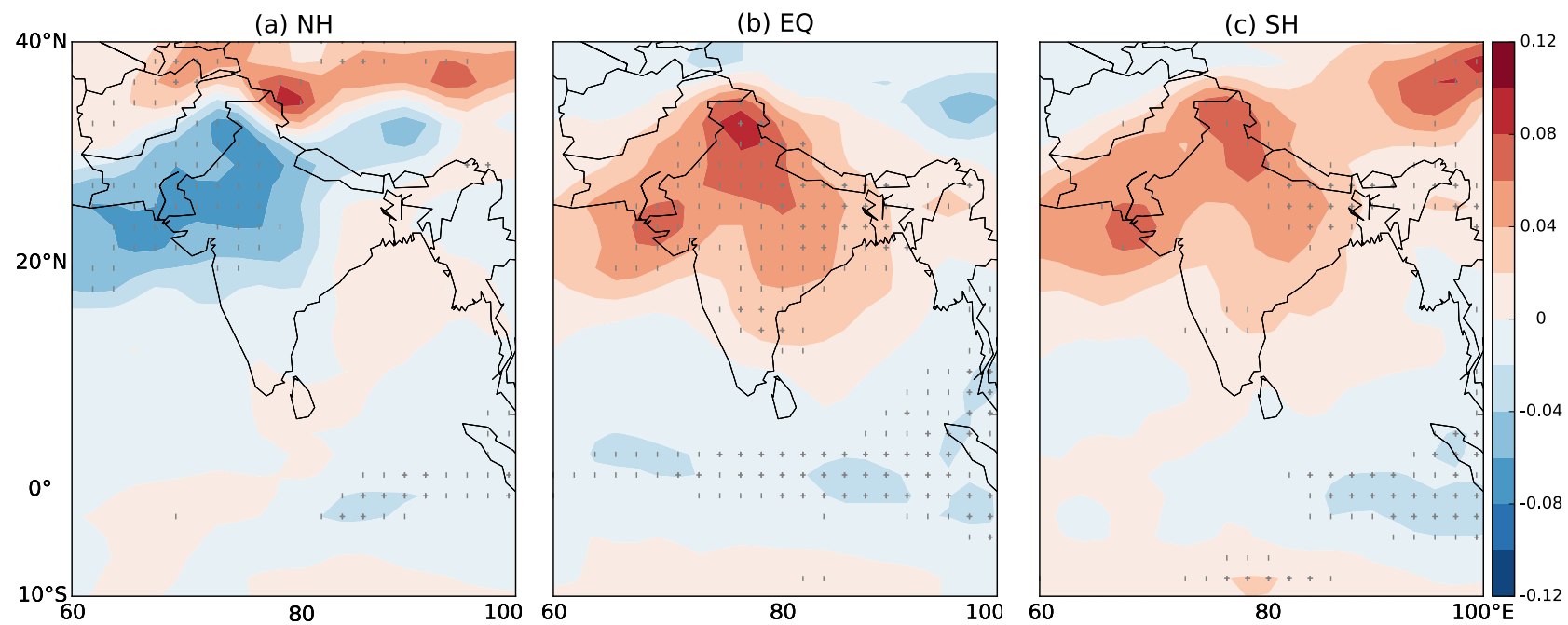


Fig. 5.15 Spatial distribution of JJA mean relative humidity (%) anomaly after the NH (a), EQ (b) and SH (c) volcanic eruptions in 1992. The vertical bars and plus signs indicate the grids that passed the significance test at the 95% and 99% confidence level based on two-tailed student's t-tests.

Then what leads to the change of the cloudiness? Atmospheric water vapor content is one of the most important factors in the formation of clouds. Our previous analyses suggested that the dynamical response to the volcanic eruptions, combined with the move of the ITCZ and the changes of the horizontal and vertical motion, lead to the water vapor change in the atmosphere over India. As a result, the water vapor content is significantly decreased over the Indian continent as well as the ocean around India after the NH volcanic eruption (figure 5.15 (a)). After the SH and EQ volcanic eruptions (figure 5.15 (c) and (b)), it increases the water vapor content over the Indian continent and the adjacent areas to the west, and the water vapor content over the Bay of Bengal and the Indian Ocean decrease significantly. This impedes (facilitates) the cloud formation in India after the NH (SH and EQ) volcanic eruption.

The radiative effects of clouds lead to the change of the temperature in India. This further affects precipitation in India. For the NH case, it increases the maximum water vapor content in the atmosphere with the increase of the temperature; meanwhile, the actual water vapor content in the atmosphere is decreased (figure 5.14). Based on the Clausius-Clapeyron equation, this will lead to the decrease of relative humidity, and thus diminishes precipitation in India. For the SH and EQ case, the increase of the actual water vapor and the decrease of the maximum water vapor content in the atmosphere will lead to the increase of relative humidity, and thus in favor of precipitation in India. This is exactly the case as shown by the spatial pattern of RH in figure 5.15 and P in and figure 5.6.

5.3.3 Scheme of the response mechanism

Based on the above analyses, the mechanism chain of the different climate effects in India after volcanic eruptions at different latitudes can be schematically summarized in figure 5.16. The stratospheric volcanic aerosols injected by volcanic eruptions directly reflect large amount of solar radiation, which decreases the amount of solar radiation reaching the surface. This brings significant cooling in the relative latitude bands that have volcanic aerosols. It alters the thermal gradient between northern and southern hemispheres and between the land and the ocean. These thermal gradients caused an indirect dynamical response, specifically, the altered thermal contrast between two hemispheres moves the ITCZ to the warmer hemisphere, and the altered land-ocean thermal contrast changes the strength of the South Asian summer monsoon and the horizontal and vertical motion of the air. This resulted in the change of water vapor content in the atmosphere over a specific region. Regional temperature and precipitation further changed, due to the physical response of atmospheric cloud and water vapor.

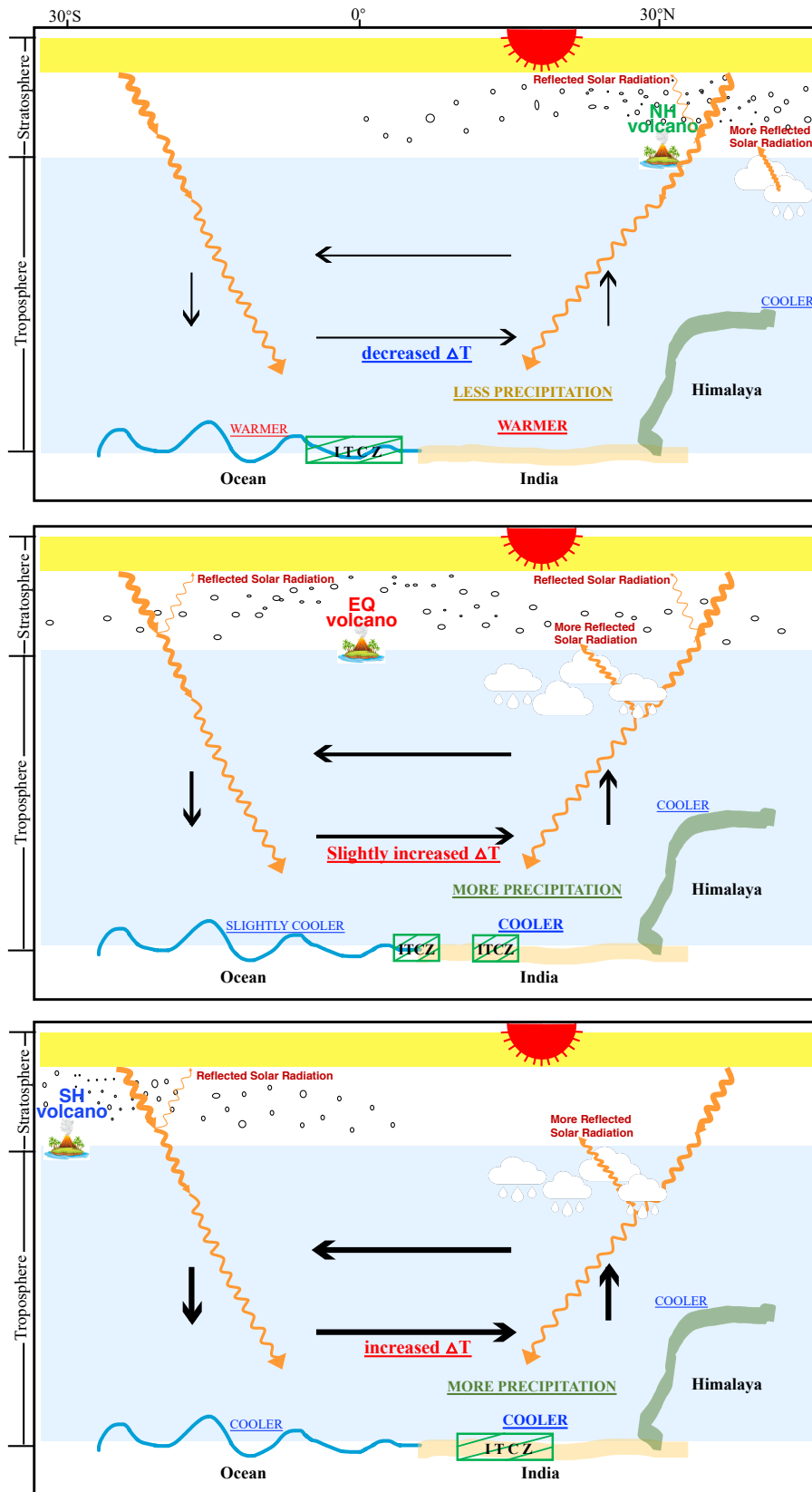


Fig. 5.16 Schematic view of the mechanism chain on the climate response to volcanic eruptions at different latitudes.

In India, after the NH volcanic eruptions, the altered hemispheric thermal contrast led to the southward movement of ITCZ; the decreased land-ocean thermal contrast weakened the SASM and diminished the horizontal and vertical motion of the air. This reduced the water vapor in the atmosphere and decreased the atmospheric cloud, which resulted in the decrease of the regional precipitation. The reduced atmospheric cloud counteracted to the cooling effect of volcanic aerosols. This negative feedback led to the increase of the regional temperature. For the SH volcanic eruptions, the altered hemispheric thermal contrast led to the northward movement of ITCZ; the increased land-ocean thermal contrast strengthened the SASM and strengthened the horizontal and vertical motion of the air. This increased the water vapor in the atmosphere and increased the atmospheric cloud, which resulted in the increase of the regional precipitation. The positive feedback of the increased atmospheric cloud further decreased the regional temperature. For the EQ eruption, evenly distributed volcanic aerosols in the two hemispheres brought a relatively symmetric radiative effect in India, but because the subsequent dynamical response led to similar physical responses to that after the SH volcanic eruptions, the temperature and precipitation patterns are also similar to that in the SH case. This illustrates the importance of the indirect dynamical response and subsequent physical feedback on the regional climate response to volcanic eruptions.

Previous studies have shown the different climate effects of symmetric and asymmetric volcanic aerosols in tropics (Colose et al., 2016a; Zuo et al., 2018), monsoon areas (Liu et al., 2016; Zuo et al., 2019) as well as in the Atlantic (Yang et al., 2019). Conclusions in this study on the different temperature and precipitation response in India to different latitudinal volcanic eruptions are in agreement with those findings in Liu et al. (2016) and Zuo et al. (2019). For the mechanism of the monsoon response to asymmetric volcanic aerosols, Zuo et al. (2019) suggested that the change of the dynamical atmospheric circulation plays a dominant role in the change of the precipitation, which is related to the changes of the monsoon circulation and the cross-equator flow. Earlier, using GISS model, Oman et al. (2005) simulated the climate effects of high-latitude eruption, and found that the radiative impacts are larger than the dynamical impacts, and the dynamical effects mainly shown in the summer over Asia, as the strong cooling in NH landmass leads to the reduction of the Asian summer monsoon circulation. This study confirms that the atmospheric circulation change due to the volcanic eruption plays an important role in the changing of the precipitation in India, because it changes the water vapor transport and the resultant formation or depletion of clouds in different areas. The regional temperature and precipitation variation result from the subsequent radiative effect of clouds and the physical feedback of the system. This is in agreement with the recent findings in Dogar and Sato (2019). They suggested that the direct radiative effect of tropical volcanic eruption and the associated land-ocean thermal

contrast result in the warming and drying effects in Middle Eastern, African and south Asian monsoon region, which is due to the reduction of clouds over the monsoon region. The indirect circulation change was summarized to be connected to the volcanic-induced ENSO forcing (Dogar and Sato, 2019). Their conclusion might have large uncertainty, as only three ensemble members were performed, and the simulations were conducted in an atmospheric circulation model with prescribed ocean boundaries conditions. Based on the fully coupled atmosphere-ocean model, results in this study show that both the NH and EQ volcanic eruptions favor El Niño in the summer of 1992, while it promotes a tendency to La Niña after the SH volcanic eruptions. After the EQ volcanic eruption, the climate response in India is similar to that after the SH volcanic eruption. This suggests that it is the indirect circulation change and the subsequent physical feedback, not so much the ENSO variation, dominate the regional climate change in India.

Chapter 6

Conclusions and outlook

This study comprehensively investigated volcanic eruptions' hydrological effects in the Asian monsoon region based on proxy reconstruction data and output from state-of-the-art global climate models. Firstly, comparisons were made between proxy reconstruction data and model simulations on the spatio-temporal hydrological responses to historical volcanic classifications in the subregions of monsoon Asia. Secondly, after verifying the reliability of CMIP5 model simulations, we used CMIP5 model outputs to examine the potential mechanism of the hydrological effects in the monsoon and westerlies-dominated subregions of Asia. The hydrological effects of volcanic eruptions at different latitudes based on large ensemble members of model simulations are also presented.

6.1 Proxy-model comparisons

This section is dedicated to the questions 1 and 2 presented in the introduction chapter of the thesis. To answer the questions, explosive volcanic eruptions in 1300 – 1849 CE and 850-1849 CE are prescribed by two volcanic reconstruction indices. The analyses of hydrological responses are based on tree-ring reconstruction data set MADA and two groups of 6 model ensemble members from CMIP5. To verify the model simulation, multi-member mean of LME project is also utilized. Superposed epoch analyses with Monte Carlo tests were applied to study the hydrological response to the volcanic classifications. Comparisons were made between MADA and models on the spatio-temporal characteristics of the hydrological effects. The long-standing proxy-model discrepancy problem is discussed. In this study, the uncertainties and limitations of both, proxy and MMEMs, were treated with the same weight, which leads to a more balanced interpretation of the results compared to previous studies. It also sheds new light on the reliability of both proxy and MMEMs of CMIP5 “last

millennium” experiment on showing historical volcanic eruptions’ hydrological effects in the subregions of the Asian monsoon region.

The answers to the questions are summarized as follows:

Question 1: What are the similarities and discrepancies between proxy and model on reflecting volcanic eruptions’ spatio-temporal hydrological effects in the subregions of the Asian monsoon region?

- MADA PDSI and CMIP5 PDSI/SPI12 agree on the significant drying effects of volcanic aerosols in the monsoon-dominated subregion, while disagreement emerges in the westerlies-dominated subregion.

- Spatial comparisons indicate a better agreement in the subregions with more tree ring sources. In w-EA, MADA PDSI agree with CMIP5 PDSI/SPI12 on the significant drying effects of northern hemispheric volcanic aerosol injections.

- In the monsoon-dominated subregions, MADA PDSI and CMIP5 PDSI/SPI12 indicate a similar drying to wetting transition after the volcanic perturbation, with faster and prolonged drying effects shown by the model data compared to the proxy reconstruction data. MADA PDSI and CMIP5 PDSI/SPI12 show better consistency in year 1 than in the eruption year, with significant drying effects in the northern EASM, SASM and SeA, and wetting effects in the southern EASM.

- In the westerlies-dominated subregions, where there is a lack of tree rings, MADA PDSI and CMIP5 PDSI/SPI12 show large discrepancies: In w-SA, MADA PDSI indicates drying effects. While, model results all indicate wetting effects. The robustness of this wetting effect can be confirmed by similar results in earlier studies found in the literature. In CA and NA subregions, MADA PDSI show significant wetting effects while CMIP5 PDSI/SPI12 in GNH classification show significant drying effects. On the other hand, CMIP5 PDSI/SPI12 in CNH show only a limited response. Therefore, it is not possible to draw a definite conclusion in these two subregions.

- The proxy-model discrepancies can be seen as a response to an overestimation of the aerosol magnitude from the volcanic forcing index and the time-lag effect of tree ring-based proxy data MADA. The effect of the uncertain timing of the eruption season on the circulation and the definition of the eruption year might also contribute to their difference in the eruption year.

Question 2: Is the multi-model ensemble mean (MEM) of CMIP5 able to reproduce volcanic eruptions’ hydrological effects in the Asian monsoon region?

- The spatio-temporal comparisons between MADA and CMIP5 MEMs suggest larger reliability of MADA PDSI in subregions with more available tree rings.

- Comparative analyses between proxy, observation and CMIP5 MMEMs in two classifications as well as LME PDSI indicate that CMIP5 MMEMs are reliable to reproduce the volcanic aerosols' hydrological effects in the southern Asian monsoon region.

6.2 Mechanism of the hydrological effects

This section answers the main questions 3 and 4 listed in the introduction chapter. After having verified the capability of CMIP5 model on reproducing the hydrological effects of northern hemispheric volcanic aerosol injection, the mechanism of the hydrological effects was examined based on CMIP5 model output. We also explored the hydrological effects of volcanic aerosol injections into southern hemisphere. The different responses to explosive volcanic eruptions in westerlies and monsoon-dominated subregion of Asia and their different mechanisms are investigated based on both temporal and spatial analyses. Based on correlation analyses, the key factors that closely related to the climate variation were identified. Further investigation on the mechanism was made based on the spatial patterns of the key factors. Results in this section fill in the gaps in the understanding of the mechanism of explosive volcanic eruptions' hydrological effects in the westerlies and monsoon-dominated subregions of Asia.

The following shows the answers to the questions:

Question 3: What is the mechanism behind the hydrological effects of the explosive volcanic eruptions in subregions of the Asian monsoon region?

- Northern hemispheric volcanic aerosol injections bring significant drying, cooling and a decreased land-ocean thermal contrast in the Asian monsoon region, with the largest effect directly visible during the eruption year.

- Regionally, it shows strongest wetting effect in the southwestern part of the Asian monsoon region while drying effects are concentrated in the southern Asian summer monsoon region, where the relatively driest area (RDA) and the relatively wettest area (RWA) locate.

- Correlation analyses suggest that surface temperature is highly correlated with longwave and shortwave radiation, while precipitation is closely related to evaporation, latent heat flux and relative humidity in climate response to volcanic eruptions.

- The distribution of the atmospheric clouds play an important role on the temperature response to volcanic eruptions. With the largest area of clouds covering the RDA, the shortwave radiation is largely decreased. This brings a significant cooling in the RDA. In the RWA, the change of the cloud cover brings slight cooling and warming in different parts of this area. This leads to a variation of the hydrological conditions. In the RDA, the cooling and the strengthened upward motion by convergence favor condensation. Water vapor

transported from adjacent areas brings more moisture, which contributes to more clouds and precipitation. This causes the wetting effect in the RDA. In the RWA, the warming diminishes the condensation, and the water vapor supply is reduced by the significantly weakened summer monsoon circulation and the decreased divergence, thus precipitation decreases. This results in the drying effect in the RWA.

Question 4: Are there different hydrological responses to different hemispheric volcanic aerosol injections?

- Comparing the GSH classification with the GNH classification, temporally, an inversed wetting effect and increased land-ocean thermal contrast can be found; spatially, most variables show inversed responses especially in the South Asian summer monsoon region. This indicates the different hydrological effects of volcanic aerosol injections in different hemispheres. Results in GSH classification are not significant. This is caused by small aerosol concentration identified in the volcanic forcing reconstruction. Different aerosol magnitudes in the GNH and GSH volcanic classifications limit the possibility to draw definite conclusion on the effects of interhemispherically asymmetric volcanic aerosols.

6.3 Climate effects of volcanic eruptions at different latitudes

This section is committed to the key questions 5, 6 and 7 raised in the introduction chapter. To understand the hydrological effect of asymmetric volcanic aerosol injections, and tropical and extratropical volcanic eruptions' climate effect in the Asian monsoon region, model simulations with three ensembles of 10-members of Pinatubo-like volcanic eruptions at 0° (EQ), 30°N (NH) and 30°S (SH) were performed based on EVA volcanic forcing generator and fully coupled general circulation model MPI-ESM-LR. Results in this section avoid the uncertainties from unequal aerosol magnitudes among different volcanic eruption cases and the climate effect of concurrent ENSO events.

The answers to the questions are summarized as follows:

Question 5: What hydrological effects do different latitudinal volcanic eruptions have in the Asian monsoon region?

- Volcanic eruptions reduce net incoming solar radiation and cool the surface especially in the boreal summer of 1992. Faster and stronger cooling is shown after the NH volcanic eruption than that after the SH and EQ eruptions. Larger reduction of the incoming solar radiation and temperature are shown in the areas covered by more volcanic aerosols.

- Volcanic eruptions bring significant cooling in the Asian monsoon region in the summer of 1992. Stronger cooling is shown after the NH volcanic eruptions than that of the EQ and SH eruptions. For precipitation, it decreases significantly after the NH volcanic eruption, while increases after the SH volcanic eruption. Precipitation responds slowly with a continuous increase from the boreal summer of 1991 to 1994 after the EQ volcanic eruption. Spatial distribution of temperature and precipitation show that the different hemispheric volcanic eruptions generate inversed climate effects in India.

Question 6: What connection have different latitudinal volcanic eruptions with ENSO variation?

- Previous studies drawn contradictory conclusions on the connection between volcanic eruptions and the evolution of ENSO and their climate effects. Through controlling the initial ENSO conditions in the simulations, we exclude the climate effects from ENSO events concurrent with volcanic eruptions. Results in this study suggest differentiated response of ENSO to volcanic eruptions at different latitudes. After the NH volcanic eruption, a tendency toward El Niño from the summer of 1992 to the end of 1994 can be found. ENSO tilted to the negative phase in the first months after the EQ volcanic eruption. An El Niño event tended to emerge one year after the eruption, and the negative phase is reached again three years after the eruption. After the SH volcanic eruption, a tendency toward the negative phase three years after the eruption can be found.

Question 7: What is the mechanism of the climate response to different latitudinal volcanic eruptions?

- Stratospheric volcanic aerosols directly influence the radiative budget of the climate system. This causes a dynamical response due to the thermal gradient change between northern and southern hemispheres as well as between land and ocean. The interhemispherically asymmetric distribution of volcanic aerosols as well as the different heat capacity of the land and ocean reinforces the effect. This leads to different responses of atmospheric water vapor content and atmospheric cloud cover over different regions.

- In India, the NH volcanic eruption leads to warming and drying effects. This is caused by the decreased water vapor advection and cloud cover over India, which comes from the suppression of the horizontal and vertical motion after the volcanic eruption. The ITCZ moves southward due to the altered interhemispheric thermal contrast. The South Asian summer monsoon is weakened due to the decreased land-ocean thermal contrast. After the SH and EQ volcanic eruptions, cooling and wetting effects result in the increase of water vapor and clouds over India, connected to an increased horizontal and vertical motion. This results from the northward movement of ITCZ and the strengthened South Asian summer monsoon after the volcanic eruptions.

6.4 Outlook

A set of global model output have been compared with a tree-ring based proxy reconstruction dataset in order to study the volcanic eruptions' hydrological effects in the subregions of the monsoon Asia. Mechanisms on hydrological effects of asymmetric volcanic aerosol distributions have been investigated based on both CMIP5 model output and self-conducted model simulation. Future researches and potential improvements can be made regarding following aspects:

- **Intercomparison of model outputs from state-of-the-art model simulations with recently published multi-proxy-based reconstruction data:** The discrepancies between tree ring-based proxy reconstruction data and model output indicate the uncertainties from both data sources. Further investigations are needed in order to improve both. This is important for understanding and predicting the hydrological effects of future volcanic eruptions. For example, the "last millennium" experiment of PMIP4/CMIP6 with further improved models Jungclaus et al. (2017) is ongoing. Shi et al. (2017) and Steiger et al. (2018) recently published reconstruction data which is not only based on tree rings, but also based on more proxy data like ice cores, lake sediments and historical records. Future analyses on these data can help to further examine the research findings shown in this thesis. Working groups of Past Global Changes dedicate to reconstruct climate data with multiple proxy sources and improve proxy model systems. Analyses on these data and collaborating with these researchers in the future will contribute to comprehensively study the climate effect of historical volcanic eruptions.

- **Improved reconstruction of volcanism:** The uncertainty (dating, strength, location) from the volcanic forcing reconstruction lead to large uncertainties on analyzing the proxy reconstruction data. This is one of the sources of the proxy-model discrepancy. A reduction of the dating uncertainty can help to better evaluate both proxy reconstruction and models. For example, recently available collection of tree rings and ice cores contribute to a large improved volcanic forcing reconstruction (Sigl et al., 2015), which will be used in the "last millennium" experiment of PMIP4/CMIP6 (Jungclaus et al., 2017). With these better-dated volcanic eruptions and newly evaluated stratospheric aerosol magnitudes, simulation on volcanic eruptions' climate effect can be largely improved. Further investigating the mechanism of the hydrological response to volcanic eruptions based on these simulations can complete the results shown in this thesis. This will also contribute to narrow down the proxy-model discrepancies, and contribute to a better understanding of the hydrological effects of volcanic eruptions.

- **Climate model simulations on characterized volcanic eruptions:** Only boreal summer eruptions were simulated in this thesis. Different injection height and magnitude of the

volcanic aerosols were not considered. These are also factors affecting the hydrological effect of volcanic eruptions. Using EVA and MPI-ESM, there is potential to design a set of new simulations with different initial conditions, in order to further explore the climate impact of different characterized volcanic eruptions, like eruptions in different seasons, different injection height of volcanic aerosols in the stratosphere and different magnitude of injected aerosols in specific areas etc. Further studies are also needed for the understanding on the connection between volcanic eruptions and ENSO variation as well as their global and regional climate impacts. Simulations based on higher resolution of the climate models can be used to further improve the simulation capacity.

- **Extending the understanding of volcanic eruptions' impact on extreme climate:** This study focuses on the patterns of the hydrological responses to volcanic eruptions. Strong drying and wetting effects of volcanic eruptions might lead to severe drought and flooding events. These are better indications of the adverse impact of volcanic eruptions. To better estimate the impact of future volcanic eruptions, further studies should be extended to examine the impacts of volcanic eruptions on the strength and frequency of the droughts and floods.

- **Stratosphere-troposphere interactions after volcanic eruptions and their role in climate:** The volcanic forcing used in this study is prescribed. This does not consider the formation and transport of volcanic aerosol in the stratosphere and the deposition of the volcanic aerosol in the troposphere. The interaction between stratosphere and troposphere through atmospheric circulation and their role in climate is important for accurately studying the volcanic eruptions' climate effect. These should be further investigated by employing fully coupled climate model with dynamical stratospheric aerosol module.

References

- Adams, J. B., Mann, M. E., and Ammann, C. M. (2003). Proxy evidence for an el niño-like response to volcanic forcing. *Nature*, 426(6964):274–278.
- Ammann, C. M., Joos, F., Schimel, D. S., Otto-Bliesner, B. L., and Tomas, R. A. (2007). Solar influence on climate during the past millennium: Results from transient simulations with the near climate system model. *Proceedings of the National Academy of Sciences of the United States of America*, 104(10):3713–3718.
- Ammann, C. M. and Naveau, P. (2003). Statistical analysis of tropical explosive volcanism occurrences over the last 6 centuries. *Geophysical Research Letters*, 30(5):n/a–n/a.
- Anchukaitis, K. J., Buckley, B. M., Cook, E. R., Cook, B. I., D'Arrigo, R. D., and Ammann, C. M. (2010). Influence of volcanic eruptions on the climate of the asian monsoon region. *Geophysical Research Letters*, 37(22):L22703.
- Braconnot, P., Harrison, S. P., Kageyama, M., Bartlein, P. J., Masson-Delmotte, V., Abe-Ouchi, A., Otto-Bliesner, B., and Zhao, Y. (2012). Evaluation of climate models using palaeoclimatic data. *Nature Climate Change*, 2(6):417–424.
- Briffa, K. R., Osborn, T. J., Schweingruber, F. H., Harris, I. C., Jones, P. D., Shiyatov, S. G., and Vaganov, E. A. (2001). Low-frequency temperature variations from a northern tree ring density network. *Journal of Geophysical Research: Atmospheres*, 106(D3):2929–2941.
- Broccoli, A. J., Dahl, K. A., and Stouffer, R. J. (2006). Response of the itcz to northern hemisphere cooling. *Geophysical Research Letters*, 33(1):n/a–n/a.
- Chen, F., Yu, Z., Yang, M., Ito, E., Wang, S., Madsen, D. B., Huang, X., Zhao, Y., Sato, T., John B. Birks, H., Boomer, I., Chen, J., An, C., and Wünnemann, B. (2008). Holocene moisture evolution in arid central asia and its out-of-phase relationship with asian monsoon history. *Quaternary Science Reviews*, 27(3-4):351–364.
- Chiang, J. C. H., Swenson, L. M., and Kong, W. (2017). Role of seasonal transitions and the westerlies in the interannual variability of the east asian summer monsoon precipitation. *Geophysical Research Letters*, 44(8):3788–3795.
- Colose, C. M., LeGrande, A. N., and Vuille, M. (2016a). Hemispherically asymmetric volcanic forcing of tropical hydroclimate during the last millennium. *Earth System Dynamics*, 7(3):681–696.
- Colose, C. M., LeGrande, A. N., and Vuille, M. (2016b). The influence of volcanic eruptions on the climate of tropical south america during the last millennium in an isotope-enabled general circulation model. *Climate of the Past*, 12(4):961–979.

- Consortium, P. H. (2017). Comparing proxy and model estimates of hydroclimate variability and change over the common era. *Climate of the Past*, 13(12):1851–1900.
- Cook, E. R., Anchukaitis, K. J., Buckley, B. M., D'Arrigo, R. D., Jacoby, G. C., and Wright, W. E. (2010). Asian monsoon failure and megadrought during the last millennium. *Science*, 328(5977):486–9.
- Crowley, T. J. and Unterman, M. B. (2013). Technical details concerning development of a 1200 yr proxy index for global volcanism. *Earth System Science Data*, 5(1):187–197.
- Crowley, T. J., ZieLinsKi, G., Vinther, B., Udisti, R., Kreutz, K., Cole-Dai, J., and Castellano, E. (2008). Volcanism and the little ice age. *PAGES news*, 16(2):22–23.
- Dai, A. G., Trenberth, K. E., and Qian, T. T. (2004). A global dataset of palmer drought severity index for 1870-2002: Relationship with soil moisture and effects of surface warming. *J. Hydrometeorol.*
- Dando, W. A. (2005). *Asia, Climates of Siberia, Central and East Asia*, pages 102–114. Springer Netherlands, Dordrecht.
- Ding, Y., Carton, J. A., Chepurin, G. A., Stenchikov, G., Robock, A., Sentman, L. T., and Krasting, J. P. (2014). Ocean response to volcanic eruptions in coupled model intercomparison project 5 simulations. *Journal of Geophysical Research: Oceans*, 119:5622–5637.
- Ding, Y. and Chan, J. C. L. (2005). The east asian summer monsoon: an overview. *Meteorology and Atmospheric Physics*, 89(1-4):117–142.
- Ding, Y., Sun, Y., Wang, Z., Zhu, Y., and Song, Y. (2009). Inter-decadal variation of the summer precipitation in china and its association with decreasing asian summer monsoon part ii: Possible causes. *International Journal of Climatology*, 29(13):1926–1944.
- Ding, Y., Wang, Z., and Sun, Y. (2008). Inter-decadal variation of the summer precipitation in east china and its association with decreasing asian summer monsoon. part i: Observed evidences. *International Journal of Climatology*, 28(9):1139–1161.
- Dogar, M. M. and Sato, T. (2019). Regional climate response of middle eastern, african, and south asian monsoon regions to explosive volcanism and enso forcing. *Journal of Geographical Research: Atmospheres*, 124.
- Dufresne, J. L., Foujols, M. A., Denvil, S., Caubel, A., Marti, O., Aumont, O., Balkanski, Y., Bekki, S., Bellenger, H., Benshila, R., Bony, S., Bopp, L., Braconnot, P., Brockmann, P., Cadule, P., Cheruy, F., Codron, F., Cozic, A., Cugnet, D., de Noblet, N., Duvel, J. P., Ethé, C., Fairhead, L., Fichefet, T., Flavoni, S., Friedlingstein, P., Grandpeix, J. Y., Guez, L., Guilyardi, E., Hauglustaine, D., Hourdin, F., Idelkadi, A., Ghattas, J., Jousaume, S., Kageyama, M., Krinner, G., Labetoulle, S., Lahellec, A., Lefebvre, M. P., Lefevre, F., Levy, C., Li, Z. X., Lloyd, J., Lott, F., Madec, G., Mancip, M., Marchand, M., Masson, S., Meurdesoif, Y., Mignot, J., Musat, I., Parouty, S., Polcher, J., Rio, C., Schulz, M., Swingedouw, D., Szopa, S., Talandier, C., Terray, P., Viovy, N., and Vuichard, N. (2013). Climate change projections using the ipsl-cm5 earth system model: from cmip3 to cmip5. *Climate Dynamics*, 40(9-10):2123–2165.

- Eyring, V., Bony, S., Meehl, G. A., Senior, C. A., Stevens, B., Stouffer, R. J., and Taylor, K. E. (2016). Overview of the coupled model intercomparison project phase 6 (cmip6) experimental design and organization. *Geoscientific Model Development*, 9(5):1937–1958.
- Fan, J. (2017). *Geography in the Second Volume of Seventh Grade*. People's Education, Beijing.
- Feng, S., Hu, Q., Wu, Q., and Mann, M. E. (2013). A gridded reconstruction of warm season precipitation for asia spanning the past half millennium. *Journal of Climate*, 26(7):2192–2204.
- Fischer, E. M., Luterbacher, J., Zorita, E., Tett, S. F. B., Casty, C., and Wanner, H. (2007). European climate response to tropical volcanic eruptions over the last half millennium. *Geophysical Research Letters*, 34(5).
- Flato, G. J., Marotzke, B., Abiodun, P. B. S. C., Collins, W., Cox, P., Driouech, F., Eyring, S. E. V., Forest, C., Gleckler, E., Guilyardi, C., Jakob, V. K., Reason, C., and Rummukainen, M. (2013). *Evaluation of Climate Models*, book section 9. Cambridge University Press, Cambridge, United Kingdom and New York, NY, USA.
- Franklin, B. (1784). Meteorological imaginations and conjectures. *Memoirs of the Manchester Literary and Philosophical Society*, 2:373–377.
- Gao, C. and Gao, Y. (2018). Revisited asian monsoon hydroclimate response to volcanic eruptions. *Journal of Geophysical Research*, 123:7883–7896.
- Gao, C., Robock, A., and Ammann, C. (2008). Volcanic forcing of climate over the past 1500 years: An improved ice core-based index for climate models. *Journal of Geophysical Research*, 113(D23):D23111.
- Gent, P. R., Danabasoglu, G., Donner, L. J., Holland, M. M., Hunke, E. C., Jayne, S. R., Lawrence, D. M., Neale, R. B., Rasch, P. J., Vertenstein, M., Worley, P. H., Yang, Z.-L., and Zhang, M. (2011). The community climate system model version 4. *Journal of Climate*, 24(19):4973–4991.
- Gillett, N. P., Weaver, A. J., Zwiers, F. W., and Wehner, M. F. (2004). Detection of volcanic influence on global precipitation. *Geophysical Research Letters*, 31(12):n/a–n/a.
- Giorgetta, M. A., Jungclaus, J., Reick, C. H., Legutke, S., Bader, J., Böttinger, M., Brovkin, V., Crueger, T., Esch, M., Fieg, K., Glushak, K., Gayler, V., Haak, H., Hollweg, H.-D., Ilyina, T., Kinne, S., Kornbluh, L., Matei, D., Mauritsen, T., Mikolajewicz, U., Mueller, W., Notz, D., Pithan, F., Raddatz, T., Rast, S., Redler, R., Roeckner, E., Schmidt, H., Schnur, R., Segschneider, J., Six, K. D., Stockhause, M., Timmreck, C., Wegner, J., Widmann, H., Wieners, K.-H., Claussen, M., Marotzke, J., and Stevens, B. (2013). Climate and carbon cycle changes from 1850 to 2100 in mpi-esm simulations for the coupled model intercomparison project phase 5. *Journal of Advances in Modeling Earth Systems*, 5(3):572–597.
- Guo, Y., Cao, J., Li, H., Wang, J., and Ding, Y. (2016). Simulation of the interface between the indian summer monsoon and the east asian summer monsoon: Intercomparison between mpi-esm and echam5/mpi-om. *Advances in Atmospheric Sciences*, 33(3):294–308.

- Ha, K.-J., Heo, K.-Y., Lee, S.-S., Yun, K.-S., and Jhun, J.-G. (2012). Variability in the east asian monsoon: a review. *Meteorological Applications*, 19(2):200–215.
- Hansen, J., Lacis, A., Ruedy, R., and Sato, M. (1992). Potential climate impact of mount pinatubo eruption. *Geophysical Research Letters*, 19(2):215–218.
- Haurwitz, M. W. and Brier, G. W. (1981). A critique of the superposed epoch analysis method: Its application to solar–weather relations. *Monthly Weather Review*, 109(10):2074–2079.
- Haywood, J. M., Jones, A., Bellouin, N., and Stephenson, D. (2013). Asymmetric forcing from stratospheric aerosols impacts sahelian rainfall. *Nature Climate Change*, 3(7):660–665.
- Hegerl, G. C., Crowley, T. J., Baum, S. K., Kim, K.-Y., and Hyde, W. T. (2003). Detection of volcanic, solar and greenhouse gas signals in paleo-reconstructions of northern hemispheric temperature. *Geophysical Research Letters*, 30(5):n/a–n/a.
- Herzschuh, U. (2006). Palaeo-moisture evolution in monsoonal central asia during the last 50,000 years. *Quaternary Science Reviews*, 25(1-2):163–178.
- Hurrell, J. W., Holland, M. M., Gent, P. R., Ghan, S., Kay, J. E., Kushner, P. J., Lamarque, J. F., Large, W. G., Lawrence, D., Lindsay, K., Lipscomb, W. H., Long, M. C., Mahowald, N., Marsh, D. R., Neale, R. B., Rasch, P., Vavrus, S., Vertenstein, M., Bader, D., Collins, W. D., Hack, J. J., Kiehl, J., and Marshall, S. (2013). The community earth system model: A framework for collaborative research. *Bulletin of the American Meteorological Society*, 94(9):1339–1360.
- Iles, C. E. and Hegerl, G. C. (2014). The global precipitation response to volcanic eruptions in the cmip5 models. *Environmental Research Letters*, 9(10):104012.
- Iles, C. E., Hegerl, G. C., Schurer, A. P., and Zhang, X. (2013). The effect of volcanic eruptions on global precipitation. *Journal of Geophysical Research: Atmospheres*, 118(16):8770–8786.
- Illing, S., Kadow, C., Pohlmann, H., and Timmreck, C. (2018). Assessing the impact of a future volcanic eruption on decadal predictions. *Earth System Dynamics*, 9(2):701–715.
- Ilyina, T., Six, K. D., Segschneider, J., Maier-Reimer, E., Li, H., and Núñez-Riboni, I. (2013). Global ocean biogeochemistry model hamocc: Model architecture and performance as component of the mpi-earth system model in different cmip5 experimental realizations. *Journal of Advances in Modeling Earth Systems*, 5(2):287–315.
- Jacobi, J., Perrone, D., Duncan, L. L., and Hornberger, G. (2013). A tool for calculating the palmer drought indices. *Water Resources Research*, 49(9):6086–6089.
- Joseph, R. and Zeng, N. (2011). Seasonally modulated tropical drought induced by volcanic aerosol. *Journal of Climate*, 24(8):2045–2060.
- Jungclaus, J. H., Bard, E., Baroni, M., Braconnot, P., Cao, J., Chini, L. P., Egorova, T., Evans, M., González-Rouco, J. F., Goosse, H., Hurtt, G. C., Joos, F., Kaplan, J. O., Khodri, M., Klein Goldewijk, K., Krivova, N., LeGrande, A. N., Lorenz, S. J., Luterbacher, J., Man, W., Maycock, A. C., Meinshausen, M., Moberg, A., Muscheler, R., Nehrbass-Ahles, C.,

- Otto-Bliesner, B. I., Phipps, S. J., Pongratz, J., Rozanov, E., Schmidt, G. A., Schmidt, H., Schmutz, W., Schurer, A., Shapiro, A. I., Sigl, M., Smerdon, J. E., Solanki, S. K., Timmreck, C., Toohey, M., Usoskin, I. G., Wagner, S., Wu, C.-J., Yeo, K. L., Zanchettin, D., Zhang, Q., and Zorita, E. (2017). The pmip4 contribution to cmip6 – part 3: The last millennium, scientific objective, and experimental design for the pmip4 past1000 simulations. *Geoscientific Model Development*, 10(11):4005–4033.
- Jungclaus, J. H., Fischer, N., Haak, H., Lohmann, K., Marotzke, J., Matei, D., Mikolajewicz, U., Notz, D., and von Storch, J. S. (2013). Characteristics of the ocean simulations in the max planck institute ocean model (mpiom) the ocean component of the mpi-earth system model. *Journal of Advances in Modeling Earth Systems*, 5(2):422–446.
- Kadow, C., Illing, S., Kunst, O., Rust, H. W., Pohlmann, H., Müller, W. A., and Cubasch, U. (2015). Evaluation of forecasts by accuracy and spread in the miklip decadal climate prediction system. *Meteorologische Zeitschrift*.
- Khodri, M., Izumo, T., Vialard, J., Janicot, S., Cassou, C., Lengaigne, M., Mignot, J., Gastineau, G., Guilyardi, E., Lebas, N., Robock, A., and McPhaden, M. J. (2017). Tropical explosive volcanic eruptions can trigger el nino by cooling tropical africa. *Nature Communications*, 8(1):778.
- Kirchner, I. and Graf, H.-F. (1995). Volcanoes and el nino: signal separation in northern hemisphere winter. *Climate Dynamics*, 11:341–358.
- Kirchner, I., Stenchikov, G. L., Graf, H.-F., Robock, A., and Antuña, J. C. (1999). Climate model simulation of winter warming and summer cooling following the 1991 mount pinatubo volcanic eruption. *Journal of Geophysical Research: Atmospheres*, 104(D16):19039–19055.
- Knutti, R. and Sedláček, J. (2012). Robustness and uncertainties in the new cmip5 climate model projections. *Nature Climate Change*, 3(4):369–373.
- Kravitz, B. and Robock, A. (2011). Climate effects of high-latitude volcanic eruptions: Role of the time of year. *Journal of Geophysical Research*, 116(D1).
- Kusunoki, S. and Arakawa, O. (2015). Are cmip5 models better than cmip3 models in simulating precipitation over east asia? *Journal of Climate*, 28(14):5601–5621.
- Lamb, H. H. and Sawyer, J. S. (1970). Volcanic dust in the atmosphere; with a chronology and assessment of its meteorological significance. *Philosophical Transactions of the Royal Society of London. Series A, Mathematical and Physical Sciences*, 266(1178):425–533.
- Li, J., Xie, S.-P., Cook, E. R., Morales, M. S., Christie, D. A., Johnson, N. C., Chen, F., D’Arrigo, R., Fowler, A. M., Gou, X., and Fang, K. (2013). El niño modulations over the past seven centuries. *Nature Climate Change*, 3(9):822–826.
- Liu, F., Chai, J., Wang, B., Liu, J., Zhang, X., and Wang, Z. (2016). Global monsoon precipitation responses to large volcanic eruptions. *Sci Rep*, 6:24331.
- Liu, F., Li, J., Wang, B., Liu, J., Li, T., Huang, G., and Wang, Z. (2018). Divergent el niño responses to volcanic eruptions at different latitudes over the past millennium. *Climate Dynamics*, 50(9-10):3799–3812.

- Loo, Y. Y., Billa, L., and Singh, A. (2015). Effect of climate change on seasonal monsoon in asia and its impact on the variability of monsoon rainfall in southeast asia. *Geoscience Frontiers*, 6(6):817–823.
- Maher, N., McGregor, S., England, M. H., and Gupta, A. S. (2015). Effects of volcanism on tropical variability. *Geophysical Research Letters*, 42(14):6024–6033.
- Man, W. and Zhou, T. (2014). Response of the east asian summer monsoon to large volcanic eruptions during the last millennium. *Chinese Science Bulletin*, 59(31):4123–4129.
- Man, W., Zhou, T., and Jungclaus, J. H. (2012). Simulation of the east asian summer monsoon during the last millennium with the mpi earth system model. *Journal of Climate*, 25(22):7852–7866.
- Man, W., Zhou, T., and Jungclaus, J. H. (2014). Effects of large volcanic eruptions on global summer climate and east asian monsoon changes during the last millennium: Analysis of mpi-esm simulations. *Journal of Climate*, 27(19):7394–7409.
- Mann, M. E., Bradley, R. S., and Hughes, M. K. (1999). Northern hemisphere temperatures during the past millennium: Inferences, uncertainties, and limitations. *Geophysical Research Letters*, 26(6):759–762.
- Mann, M. E., Cane, M. A., Zebiak, S. E., and Clement, A. (2005). Volcanic and solar forcing of the tropical pacific over the past 1000 years. *Journal of Climate*, 18:447–456.
- Mann, M. E., Fuentes, J. D., and Rutherford, S. (2012). Underestimation of volcanic cooling in tree-ring-based reconstructions of hemispheric temperatures. *Nature Geoscience*, 5(3):202–205.
- McGregor, S. and Timmermann, A. (2011). The effect of explosive tropical volcanism on enso. *Journal of Climate*, 24(8):2178–2191.
- McKee, T., Doesken, N., and Kleist, J. (1993). The relationship of drought frequency and duration to time scale. In *Proceedings of the Eighth Conference on Applied Climatology, Anaheim, California, Boston, American Meteorological Society*, 179–184.
- Myhre, G., Shindell, D., Bréon, F.-M., Collins, W., Fuglestedt, J., Huang, J., Koch, D., Lamarque, J.-F., Lee, D., Mendoza, B., Nakajima, T., Robock, A., Stephens, G., Takemura, T., and Zhang, H. (2013). *Anthropogenic and Natural Radiative Forcing*. Cambridge University Press, Cambridge, United Kingdom and New York, NY, USA.
- Newhall, C. G. and Self, S. (1982). The volcanic explosivity index (vei) an estimate of explosive magnitude for historical volcanism. *Journal of Geophysical Research*, 87(C2).
- Oman, L., Robock, A., and Stenchikov, G. L. (2005). Climatic response to high-latitude volcanic eruptions. *Journal of Geophysical Research*, 110(D13103).
- Oman, L., Robock, A., Stenchikov, G. L., and Thordarson, T. (2006). High-latitude eruptions cast shadow over the african monsoon and the flow of the Nile. *Geophysical Research Letters*, 33(L18711).

- Otto-Bliesner, B. L., Brady, E. C., Fasullo, J., Jahn, A., Landrum, L., Stevenson, S., Rosenbloom, N., Mai, A., and Strand, G. (2016). Climate variability and change since 850 ce: An ensemble approach with the community earth system model. *Bulletin of the American Meteorological Society*, 97(5):735–754.
- Paik, S. and Min, S.-K. (2016). Climate responses to volcanic eruptions assessed from observations and cimp5 multi-models. *Climate Dynamics*.
- Pausata, F. S., Chafik, L., Caballero, R., and Battisti, D. S. (2015). Impacts of high-latitude volcanic eruptions on enso and amoc. *Proc Natl Acad Sci U S A*, 112(45):13784–8.
- Peng, Y., Shen, C., Wang, W.-C., and Xu, Y. (2010). Response of summer precipitation over eastern china to large volcanic eruptions. *Journal of Climate*, 23:818–824.
- Pitari, G. and Mancini, E. (2002). Short-term climatic impact of the 1991 volcanic eruption of mt. pinatubo and effects on atmospheric tracers. *Natural Hazards and Earth System Sciences*, 2:91–108.
- Predybaylo, E., Stenchikov, G. L., Wittenberg, A. T., and Zeng, F. (2017). Impacts of a pinatubo-size volcanic eruption on enso. *Journal of Geophysical Research: Atmospheres*, 122(2):925–947.
- Preethi, B., Mujumdar, M., Kripalani, R. H., Prabhu, A., and Krishnan, R. (2016). Recent trends and tele-connections among south and east asian summer monsoons in a warming environment. *Climate Dynamics*, 48(7-8):2489–2505.
- Reick, C. H., Raddatz, T., Brovkin, V., and Gayler, V. (2013). Representation of natural and anthropogenic land cover change in mpi-esm. *Journal of Advances in Modeling Earth Systems*, 5(3):459–482.
- Robock, A. (2000). Volcanic eruptions and climate. *Reviews of Geophysics*, 38(2):191–219.
- Robock, A. (2002). Pinatubo eruption. the climatic aftermath. *Science*, 295(5558):1242–4.
- Robock, A. (2015). *Climatic Impacts of Volcanic Eruptions*, book section 53, pages 935–942. Elsevier, Amsterdam, second edition.
- Robock, A. and Free, M. P. (1995). Ice cores as an index of global volcanism from 1850 to the present. *Journal of Geographical Research*, 100:11549–11567.
- Robock, A. and Mao, J. (1995). The volcanic signa in surface temperature observations. *Journal of Climate*, 8:1086–1103.
- Robock, A. and Y., L. (1994). The volcanic signal in goddard institute for space studies three-dimensional model simulations. *Journal of Climate*, 7:44–55.
- Roeckner, E., Brokopf, R., Esch, M., Giorgetta, M., Hagemann, S., Kornblueh, L., Manzini, E., Schlese, U., and Schulzweida, U. (2006). Sensitivity of simulated climate to horizontal and vertical resolution in the echam5 atmosphere model. *Journal of Climate*, 19:3771–3791.

- Schmidt, G. A., Jungclauss, J. H., Ammann, C. M., Bard, E., Braconnot, P., Crowley, T. J., Delaygue, G., Joos, F., Krivova, N. A., Muscheler, R., Otto-Bliesner, B. L., Pongratz, J., Shindell, D. T., Solanki, S. K., Steinhilber, F., and Vieira, L. E. A. (2011). Climate forcing reconstructions for use in pmip simulations of the last millennium (v1.0). *Geoscientific Model Development*, 4(1):33–45.
- Schmidt, G. A., Kelley, M., Nazarenko, L., Ruedy, R., Russell, G. L., Aleinov, I., Bauer, M., Bauer, S. E., Bhat, M. K., Bleck, R., Canuto, V., Chen, Y.-H., Cheng, Y., Clune, T. L., Del Genio, A., de Fainchtein, R., Faluvegi, G., Hansen, J. E., Healy, R. J., Kiang, N. Y., Koch, D., Lacis, A. A., LeGrande, A. N., Lerner, J., Lo, K. K., Matthews, E. E., Menon, S., Miller, R. L., Oinas, V., Oloso, A. O., Perlwitz, J. P., Puma, M. J., Putman, W. M., Rind, D., Romanou, A., Sato, M., Shindell, D. T., Sun, S., Syed, R. A., Tausnev, N., Tsigaridis, K., Unger, N., Voulgarakis, A., Yao, M.-S., and Zhang, J. (2014). Configuration and assessment of the giss modele2 contributions to the cmip5 archive. *Journal of Advances in Modeling Earth Systems*, 6(1):141–184.
- Schneck, R., Reick, C. H., and Raddatz, T. (2013). Land contribution to natural co2variability on time scales of centuries. *Journal of Advances in Modeling Earth Systems*, 5(2):354–365.
- Schneider, D. P., Ammann, C. M., Otto-Bliesner, B. L., and Kaufman, D. S. (2009). Climate response to large, high-latitude and low-latitude volcanic eruptions in the community climate system model. *Journal of Geophysical Research*, 114(D15).
- Schneider, L., Smerdon, J. E., Buntgen, U., Wilson, R. J. S., Myglan, V. S., Kirilyanov, A. V., and Esper, J. (2015). Revising midlatitude summer temperatures back to ad600 based on a wood density network. *Geophysical Research Letters*, 42(11):4556–4562.
- Shen, C., Wang, W.-C., Hao, Z., and Gong, W. (2007). Exceptional drought events over eastern china during the last five centuries. *Climatic Change*, 85(3-4):453–471.
- Shi, F., Zhao, S., Guo, Z., Goosse, H., and Yin, Q. (2017). Multi-proxy reconstructions of may–september precipitation field in china over the past 500 years. *Climate of the Past*, 13(12):1919–1938.
- Shi, J., Yan, Q., Jiang, D. B., Min, J. Z., and Jiang, Y. (2016). Precipitation variation over eastern china and arid central asia during the past millennium and its possible mechanism: Perspectives from pmip3 experiments. *Journal of Geophysical Research-Atmospheres*, 121(20):11989–12004.
- Sigl, M., Winstrup, M., McConnell, J. R., Welten, K. C., Plunkett, G., Ludlow, F., Buntgen, U., Caffee, M., Chellman, N., Dahl-Jensen, D., Fischer, H., Kipfstuhl, S., Kostick, C., Maselli, O. J., Mekhaldi, F., Mulvaney, R., Muscheler, R., Pasteris, D. R., Pilcher, J. R., Salzer, M., Schupbach, S., Steffensen, J. P., Vinther, B. M., and Woodruff, T. E. (2015). Timing and climate forcing of volcanic eruptions for the past 2,500 years. *Nature*, 523(7562):543–9.
- Song, F. and Zhou, T. (2014). The climatology and interannual variability of east asian summer monsoon in cmip5 coupled models: Does air–sea coupling improve the simulations? *Journal of Climate*, 27(23):8761–8777.
- Steiger, N. J., Smerdon, J. E., Cook, E. R., and Cook, B. I. (2018). A reconstruction of global hydroclimate and dynamical variables over the common era. *Sci Data*, 5:180086.

- Stevens, B., Giorgetta, M., Esch, M., Mauritsen, T., Crueger, T., Rast, S., Salzmann, M., Schmidt, H., Bader, J., Block, K., Brokopf, R., Fast, I., Kinne, S., Kornbluh, L., Lohmann, U., Pincus, R., Reichler, T., and Roeckner, E. (2013). Atmospheric component of the mpi-m earth system model: Echam6. *Journal of Advances in Modeling Earth Systems*, 5(2):146–172.
- Stevenson, S., Fasullo, J. T., Otto-Bliesner, B. L., Tomas, R. A., and Gao, C. (2017). Role of eruption season in reconciling model and proxy responses to tropical volcanism. *Proceedings of the National Academy of Sciences of the United States of America*, 114(8):1822–1826.
- Stevenson, S., Otto-Bliesner, B., Fasullo, J., and Brady, E. (2016). “el niño like” hydroclimate responses to last millennium volcanic eruptions. *Journal of Climate*, 29(8):2907–2921.
- Stoffel, M., Khodri, M., Corona, C., Guillet, S., Poulain, V., Bekki, S., Guiot, J., Luckman, B. H., Oppenheimer, C., Lebas, N., Beniston, M., and Masson-Delmotte, V. (2015). Estimates of volcanic-induced cooling in the northern hemisphere over the past 1,500 years. *Nature Geoscience*, 8(10):784–788.
- Sun, W., Liu, J., Wang, B., Chen, D., Liu, F., Wang, Z., Ning, L., and Chen, M. (2018). A “la niña-like” state occurring in the second year after large tropical volcanic eruptions during the past 1500 years. *Climate Dynamics*.
- Taylor, K. E., Stouffer, R. J., and Meehl, G. A. (2012). An overview of cmip5 and the experiment design. *Bulletin of the American Meteorological Society*, 93(4):485–498.
- Timmreck, C. (2012). Modeling the climatic effects of large explosive volcanic eruptions. *Wiley Interdisciplinary Reviews: Climate Change*, 3(6):545–564.
- Timmreck, C., Pohlmann, H., Illing, S., and Kadow, C. (2016). The impact of stratospheric volcanic aerosol on decadal-scale climate predictions. *Geophysical Research Letters*, 43(2):834–842.
- Toohey, M., Krüger, K., Schmidt, H., Timmreck, C., Sigl, M., Stoffel, M., and Wilson, R. (2019). Disproportionately strong climate forcing from extratropical explosive volcanic eruptions. *Nature Geoscience*, 12(2):100–107.
- Toohey, M. and Sigl, M. (2017). Volcanic stratospheric sulfur injections and aerosol optical depth from 500bce to 1900ce. *Earth System Science Data*, 9(2):809–831.
- Toohey, M., Stevens, B., Schmidt, H., and Timmreck, C. (2016). Easy volcanic aerosol (eva v1.0): an idealized forcing generator for climate simulations. *Geoscientific Model Development*, 9(11):4049–4070.
- Trenberth, K. E. and Dai, A. (2007). Effects of mount pinatubo volcanic eruption on the hydrological cycle as an analog of geoengineering. *Geophysical Research Letters*, 34(15):L15702.
- Valcke, S. (2013). The oasis3 coupler: a european climate modelling community software. *Geoscientific Model Development*, 6(2):373–388.

- Wang, B. and Fan, Z. (1999). Choice of south asian summer monsoon indices. *Bulletin of the American Meteorological Society*, 80(4):629–638.
- Wang, B. and Lin, H. (2002). Rainy season of the asian–pacific summer monsoon. *Journal of Climate*, 15:386–398.
- Wang, B., Wu, Z., Li, J., Liu, J., Chang, C.-P., Ding, Y., and Wu, G. (2008). How to measure the strength of the east asian summer monsoon. *Journal of Climate*, 21(17):4449–4463.
- Wang, P., Clemens, S., Beaufort, L., Braconnot, P., Ganssen, G., Jian, Z., Kershaw, P., and Sarnthein, M. (2005). Evolution and variability of the asian monsoon system: state of the art and outstanding issues. *Quaternary Science Reviews*, 24(5-6):595–629.
- Wang, T., Guo, D., Gao, Y., Wang, H., Zheng, F., Zhu, Y., Miao, J., and Hu, Y. (2017). Modulation of enso evolution by strong tropical volcanic eruptions. *Climate Dynamics*.
- Wang, T., Otterå, O. H., Gao, Y., and Wang, H. (2012). The response of the north pacific decadal variability to strong tropical volcanic eruptions. *Climate Dynamics*, 39(12):2917–2936.
- Watanabe, S., Hajima, T., Sudo, K., Nagashima, T., Takemura, T., Okajima, H., Nozawa, T., Kawase, H., Abe, M., Yokohata, T., Ise, T., Sato, H., Kato, E., Takata, K., Emori, S., and Kawamiya, M. (2011). Miroc-esm 2010: model description and basic results of cmip5-20c3m experiments. *Geoscientific Model Development*, 4(4):845–872.
- Webster, P. J. and Yang, S. (1992). Monsoon and enso: Selectively interactive systems. *Quarterly Journal of the Royal Meteorological Society*, 118:877–926.
- Wegmann, M., Brönnimann, S., Bhend, J., Franke, J., Folini, D., Wild, M., and Luterbacher, J. (2014). Volcanic influence on european summer precipitation through monsoons: Possible cause for “years without summer”*. *Journal of Climate*, 27(10):3683–3691.
- Wilson, R., Anchukaitis, K., Briffa, K. R., Büntgen, U., Cook, E., D’Arrigo, R., Davi, N., Esper, J., Frank, D., Gunnarson, B., Hegerl, G., Helama, S., Klesse, S., Krusic, P. J., Linderholm, H. W., Myglan, V., Osborn, T. J., Rydval, M., Schneider, L., Schurer, A., Wiles, G., Zhang, P., and Zorita, E. (2016). Last millennium northern hemisphere summer temperatures from tree rings: Part i: The long term context. *Quaternary Science Reviews*, 134:1–18.
- Wood, G. D. (2015). *Tambora: The Eruption That Changed the World*. Princeton University Press, New York.
- Wu, D., Zhao, X., Liang, S., Zhou, T., Huang, K., Tang, B., and Zhao, W. (2015). Time-lag effects of global vegetation responses to climate change. *Glob Chang Biol*, 21(9):3520–31.
- Wu, T., Li, W., Ji, J., Xin, X., Li, L., Wang, Z., Zhang, Y., Li, J., Zhang, F., Wei, M., Shi, X., Wu, F., Zhang, L., Chu, M., Jie, W., Liu, Y., Wang, F., Liu, X., Li, Q., Dong, M., Liang, X., Gao, Y., and Zhang, J. (2013). Global carbon budgets simulated by the beijing climate center climate system model for the last century. *Journal of Geophysical Research: Atmospheres*, 118(10):4326–4347.

- Yancheva, G., Nowaczyk, N. R., Mingram, J., Dulski, P., Schettler, G., Negendank, J. F., Liu, J., Sigman, D. M., Peterson, L. C., and Haug, G. H. (2007). Influence of the intertropical convergence zone on the east asian monsoon. *Nature*, 445(7123):74–7.
- Yang, W., Gabriel A., Vecchi Stephan, F., Larry W., H., David J., L., Ángel G., M., David, P., and Seth, U. (2019). Climate impacts from large volcanic eruptions in a high-resolution climate model: The importance of forcing structure. *Geophys Res Lett*, 46:7690–7699.
- Zambri, B. and Robock, A. (2016). Winter warming and summer monsoon reduction after volcanic eruptions in coupled model intercomparison project 5 (cmip5) simulation. *Geophysical Research Letters*, 43:10920–10928.
- Zambri, B., Robock, A. N. L. A., and Slawinska, J. (2017). Northern hemisphere winter warming and summer monsoon reduction after volcanic eruptions over the last millennium. *Journal of Geophysical Research-Atmospheres*, 122:7971–7989.
- Zhang, D., Blender, R., and Fraedrich, K. (2012). Volcanoes and enso in millennium simulations: global impacts and regional reconstructions in east asia. *Theoretical and Applied Climatology*, 111(3-4):437–454.
- Zhou, T., Gong, D., Li, J., and Li, B. (2009). Detecting and understanding the multi-decadal variability of the east asian summer monsoon recent progress and state of affairs. *Meteorologische Zeitschrift*, 18(4):455–467.
- Zhou, T., Wu, B., Wen, X., Li, L., and Wang, B. (2008). A fast version of lasg/iap climate system model and its 1000-year control integration. *Advances in Atmospheric Sciences*, 25(4):655–672.
- Zhuo, Z., Gao, C., and Pan, Y. (2014). Proxy evidence for china’s monsoon precipitation response to volcanic aerosols over the past seven centuries. *Journal of Geophysical Research*, 119(11):6638–6652.
- Zuo, M., Man, W. M., Zhou, T. J., and Guo, Z. (2018). Different impacts of northern, tropical, and southern volcanic eruptions on the tropical pacific sst in the last millennium. *Journal of Climate*, 31(17):6729–6744.
- Zuo, M., Zhou, T., and Man, W. (2019). Hydroclimate responses over global monsoon regions following volcanic eruptions at different latitudes. *Journal of Climate*, 32(14):4367–4385.

Appendix A

List of abbreviations

A07	volcanic classification following Ammann et al. (2007)
AMR	Asian monsoon region
AN03	volcanic classification following Ammann and Naveau (2003)
AOD	aerosol optical depth
C	cloud area fraction [%]
CA	Central Asia
CAM5	Community Atmosphere Model version 5
CCSM	Community Climate System Model
CESM	Community Earth System Model
CMIP5	the fifth phase of Coupled Model Intercomparison Project
CMIP5 PDSI	multi-model ensemble mean of PDSI from CMIP5 "LM" experiment
CMIP5 SPI12	multi-model ensemble mean of SPI12 from CMIP5 "LM" experiment
CNH	volcanic classification with NHVAI larger than 1991 Pinatubo eruption based on Crowley et al. (2008)
CTR	control run
DLR	Surface Downwelling Longwave Radiation [W/m^2]
E	Evaporation [mm/day]
EA	East Asia
EASM	East Asian summer monsoon
EASMI	EASM Index [m/s]
ENSO	El Niño-Southern Oscillation
EQ	equator
EVA	Easy Volcanic Aerosol
F07	volcanic classification following Fischer et al. (2007)

GCNH	volcanic classification with NHVAI larger than 1991 Pinatubo eruption based on both Gao et al. (2008) and Crowley et al. (2008)
GFDL-CM2.1	Geophysical Fluid Dynamics Laboratory Climate Model Version 2.1
GNH	volcanic classification with NHVAI larger than 1991 Pinatubo eruption based on Gao et al. (2008)
GSH	volcanic classification with only SHVAI based on Gao et al. (2008)
ISR	Incident Shortwave Radiation [W/m^2]
ITCZ	Intertropical Convergence Zone
IVI	ice-core volcano index
JJA	June-July-August
LHF	Surface Upward Latent Heat Flux [W/m^2]
LM	last millennium
LME	Last Millennium Ensemble
LME PDSI	multi-member mean of PDSI from LME "volcanic only" experiment
LR	low-resolution
LR	longwave radiation [W/m^2]
MADA	Monsoon Asia Drought Atlas
MADA PDSI	Proxy reconstruction MADA based on tree rings and Dai et al. (2004) PDSI
MME	multi-model ensemble
MMEM	multi-model ensemble mean
MPI-ESM	Max-Planck-Institute Earth System Model
NA	North Asia
NCAR	National Center for Atmospheric Research
NH	northern hemisphere
NOAA	National Oceanic and Atmospheric Administration
OLR	Outgoing Longwave Radiation [W/m^2]
ONI	Oceanic Niño Index [$^{\circ}\text{C}$]
OSR	Outgoing Shortwave Radiation [W/m^2]
P	precipitation [mm/day]
PDSI	Palmer Drought Severity Index
PMIP3	the third phase of paleoclimate model intercomparison project
r	Pearson cross correlation
RDA	relatively driest area
RH	Near-surface Relative Humidity [%]
RWA	relatively wettest area

SA	South Asia
SASM	South Asian summer monsoon
SASMI	SASM Index [m/s]
SD	standard deviation
SEA	superposed epoch analysis
SeA	Southeast Asia
SH	southern hemisphere
SHF	Surface Upward Sensible Heat Flux [W/m^2]
SNH	volcanic classification with NHVAI larger than 1991 Pinatubo eruption based on Sigl et al. (2015)
SPI12	12-months of Standardized Precipitation Index
SR	Shortwave radiation [W/m^2]
SST	Sea surface temperature [$^{\circ}\text{C}$]
T	Temperature [$^{\circ}\text{C}$]
TOA	Top of the atmosphere
TP	Tibetan Plateau
ULR	Surface Upwelling Longwave Radiation [W/m^2]
USR	Surface Upwelling Shortwave Radiation [W/m^2]
VAI	volcanic aerosol injection
VIMF	vertical integrated moisture flux [$\text{kg}/\text{m}\cdot\text{s}$]
VIMFD	VIMF divergence [$10^{-5} \text{ kg}/\text{m}^2\cdot\text{s}$]
w-EA	Western-East Asia
WCRP	World Climate Research Programme
WGCM	Working Group on Coupled Modelling
WPSH	Western Pacific subtropical high

Acknowledgements

The past four years was a wonderful journey in my life. I learned to look at things with an open mind. I grow up to an independent researcher. I know myself better than ever before. I will always remember the unconditional support and help I received during this journey.

I would like to express my sincere appreciation to my supervisor Prof. Dr. Ulrich Cubasch. He gave me this great opportunity to pursue my PhD in the institute of Meteorology, FUB. I got full support from him to freely carry out my researches and actively participate in summer schools and academic conferences. He gave me constructive suggestions and feedbacks whenever I need, and helped me to connect with colleagues and other scientists. It's his constant support and help during the past four years that enables me to finish my PhD.

I would also like to express my sincere gratitude to my second supervisor Dr. Ingo Kirchner. He is always there to help me to solve the problems whenever I faced in my study. Even in weekends and holidays, he is ready to help me and answer my emails. I learned to better use the professional software with him. We had so many discussions that helped me to think deeply into my research and find out the next steps. I learned critical thinking from him in this process. Without his help, I could not have finished my thesis today.

I sincerely appreciate Prof. Dr. Stephan Pfahl for his suggestions, support and help on my study. I am thankful for being part of the climate modelling group (Klimod) and Weather and Climate Processes group (Weclip). Many thanks to all my colleagues. I benefit a lot from the group meetings and enjoyed so much working together with them.

I greatly acknowledge Prof. Dr. Kirstin Krüger for her supervision during my research stay in University of Oslo and her trust to give me the opportunity to do a postdoc with her after my PhD. This also gave me full motivation to finish this thesis. I sincerely appreciate Dr. Matthew Toohey and Dr. Claudia Timmreck for their help and suggestions on my study.

I appreciate the China Scholarship Council (CSC) and FUB for providing me the financial support. I acknowledge the German Climate Computing Center (DKRZ) and FUB for providing the computer sources and data services.

Words cannot express how grateful I am to my family. The love, support and encouragement from my mother Yunlan Guo, my father Liming Zhuo and my brother Jun Zhuo as always helped me to conquer all the difficulties I faced through this journey.

”
The way was long, and wrapped in gloom did seem
As I urged on to seek my vanished dream

—Yuan Qu [340 BCE-278 BCE, Poet and Politician]